FORMATION OF SILICON NANOCRYSTALS IN SiO_2 BY SILICON IMPLANTATION AND SUBSEQUENT ANNEALING

FORMATION OF SILICON NANOCRYSTALS IN SiO_2 BY SILICON IMPLANTATION AND SUBSEQUENT ANNEALING

By

MD. ASKER IBNA SHAIKH, B.Sc.

A Thesis

Submitted to the School of Graduate Studies

in Partial Fulfillment of the Requirements

for the Degree

Master of Applied Science

McMaster University

Hamilton, Ontario, Canada

MASTER OF APPLIED SCIENCE (2012) McMaster University
(Engineering Physics) Hamilton, Ontario, Canada

TITLE	Formation of Silicon Nanocrystals in SiO_2 by Silicon Implantation and Subsequent Annealing
AUTHOR	Md. Asker Ibna Shaikh, B.Sc.
SUPERVISOR	Dr. A P Knights, Associate Professor Department of Engineering Physics
NUMBER OF PAGES	xx, 112

ABSTRACT

Since the first description of Si nanocrystals, research in this field has gone through raid progress and potential applications of Si nanocrystals have been established. There are several methods applicable to the fabrication of Si nanocrystals with one of the most used being ion implantation followed by thermal annealing. Two types of thermal annealing are available for use: furnace annealing (FA) for several hours, normally in an N_2 atmosphere; and rapid thermal annealing (RTA) for a short time (less than a few minutes), again in an inert atmosphere such as N_2. The formation of the nanocrystals then proceeds with decomposition, segregation, diffusion, nucleation, aggregation, growth and crystallization. This formation requires temperatures in excess of 1000^{o} C such that noticeable photoluminescence may be observed. This thesis explores the fabrication of Si nanocrystals using the McMaster ion implanter and subsequent RTA. The implantation conditions required to form luminescent nanocrystals are determined. For example, for an implantation energy of 10 KeV a minimum dose of 1.5×10^{16} ions cm^{-2} is required. The relationship between luminescent intensity and post-implantation annealing is also explored. An optimum annealing temperature of 1100^{o}C is found. For the first time to the author's knowledge, a study of the effects of thin film thickness on luminescent intensity is conducted. The major conclusions of this thesis are i) a specific thickness of oxide layer has the maximum PL for a fixed implantation energy and implantation dose, ii) PL intensity is inversely proportional with measuring temperature., iii) the type of oxidation process has a large effect on PL intensity.

ACKNOWLEDGEMENT

The author thanks the almighty for the successful completion of the thesis. He would like to express his heartiest gratitude, profound gratefulness as well as deep admiration to his supervisor Dr. Andy P Knights for his supervision, constant encouragement and valuable ideas accompanied by constant help through the course of work. He would also like to thank his friend Dr. Mohammad Hasanuzzaman and Dhrubo Saha for their continuous help during the thesis.

The author is also grateful to the department of Engineering Physics of McMaster University for providing the laboratory support throughout the thesis work. He would also like to thank Doris Stevanovic, Zhilin Peng, Peter Jonasson, Marilyn Marlow from the department of Engineering Physics for their incessant help during the thesis.

The author would also like to thank his friends and colleagues of photonics laboratory for their generous support throughout the thesis. The author also would like to express his thankfulness to his family. The author would like to specially thank M. A. Mabud, who continually fortified and supported him. The author would like express his heartiest thankfulness to his wife Eshita Farhana Esha, who continuously motivated, supported, helped, encouraged the author and without her kind support it would not be possible to finish the thesis as well as acquire many success of author's life.

TABLE OF CONTENTS

LIST OF FIGURES

LIST OF TABLES

LIST OF ABBREVIATIONS

DF	Dark Field
FA	Furnace Annealer
HERM	High Resolution Electron Microscopy
IC	Integrated Circuit
LED	Light Emitting Diode
Si-nc	Silicon Nanocrystals
SRIM	Stopping and Range of Ions in Matter
PC	Photocurrent
PV	Photovoltaic
PL	Photo Luminescence
RTA	Rapid Thermal Annealer
RTP	Rapid Thermal Furnace
TEM	Transmission Electron Microscope
UV	Ultra Violate

CHAPTER ONE: INTRODUCTION

Silicon is an indirect semiconductor with a band gap close to 1.1 eV at room temperature. In its bulk form it has very low luminescence efficiency and for this reason it has very few applications as a photonics material [1]. Despite its indirect nature, silicon may be an efficient optical emitter when confined to a small volume such as is the case for porous Si which exhibits strong photoluminescence in the visible range at room temperature [2]. This behavior draws the attention of researchers.

Si nanocrystals embedded in SiO_2 have the properties of strong light emission, high thermal and chemical constancy and potential for compatibility with silicon electronics. Lots of investigation has taken place on the photoluminescence behavior in Si nanocrystals in embedded SiO_2 [3]. In the current work presented here, I investigate and report on the fabrication of Si nanocrystals via ion implantation of silicon into SiO_2 followed by thermal annealing.

1.1 The Indirect Band Gap

If the maximum of the valance band and the minimum of the conduction band are at the same *k* (wave vector) point, a semiconductor is referred to as direct and in this case only optical energy (photon energy) is needed for transition of electrons from one band to the other. For an indirect semiconductor the maximum of the valance band and the minimum of the conduction band are at a different *k* point and in this case phonon and photon energy are needed for the electron transition [4].

The band gap (E_g) is the energy difference between the valence band (E_v) and conduction band (E_c). For insulator materials the difference is larger than for semiconductors, while for metals the two bands overlap so there is no apparent band gap. At T= 0 K the valance band is filled with electrons and the conduction band is empty [4].

Direct band gap semiconductors are thus better for optical use than indirect band gap semiconductors. In the former, electrons in the conduction band can release energy in a downward transition to the valance band. There is no *k* (wave vector) difference so efficient light emission ensues where $E_g = h\nu$, where *h* is the planck constant and ν is the frequency of light. For indirect band gap semiconductor the wave vector *k* is not the same for the maxima of the conduction band and minima of the valance band. So in this case when electrons transition from the conduction band to the valance band the amount of energy released is divided into two parts: one is for the change in *k* (i.e. change of the electron momentum) and the other is for photon emission. For this reason indirect band gap semiconductors emit relatively weak light compared to direct band gap semiconductor [4].

1.2 Emission from Low Dimensional Silicon and Motivation for This Work

Bulk Si is an indirect material. For this reason the light emission efficiency from bulk Si is very low. On the other hand light emission efficiency from Si nanocrystals is relatively high. There is some controversy about the origin of light emission from Si nanocrystals [5-8]. Here quantum confinement and the interface layer behavior along with oxide defects are two possible causes for the light emission from Si nanocrystals [5-8]. At

the small dimension, and thus due to quantum confinement, the wave functions of the hole and electron confined in Si nanocrystals overlap, thus it is easier to recombine holes and electrons [2]. Wave function overlapping provides a route to a quasi-direct silicon structure, thus the light emission efficiency is dramatically increased.

Si nanocrystals have potential use in a number of fields such as: multicolor electroluminescence devices; PV and PC cells; flat panel displays; and even in biology for applications such as drug delivery [9].

Stable light emitting diodes (LED) have been made from Si nanocrystals embedded in SiO_2, including some reports of devices fabricated via ion implantation [10]. All these applications provide motivation for the current work.

1.3 Objective of the Thesis

The main objectives of the research leading to this thesis are:

- To analyze the formation of Si nanocrystals via ion implantation and annealing.
- To analyze the effect of different implantation energies and doses and different annealing temperatures.
- To study the effect of different oxide layer thickness on the formation of Si nanocrystals.
- To study the differences between formation of silicon nanocrystals in oxides formed by dry oxidation or wet oxidation.

1.4 Organization of the Thesis

Chapter 1 provides a brief introduction to the motivation for this work; describes the goals and achievements and summarizes the organization of this thesis.

Chapter 2 presents a background literature review relevant to the thesis; while the theoretical considerations required by my research are discussed.

Chapter 3 describes operating systems for the fabrication and characterization equipment I used for my experiments.

Chapter 4 presents the results obtained and discusses them in the context of other works.

Chapter 5 presents some concluding remarks and highlights some possible promising avenues of further development.

1.5 Summary of Contribution

During the course of my research the following contributions to the development of the understanding to the formation of silicon nanocrystals have been addressed:

- Calibration of rapid thermal annealer.
- Investigating the optimal annealing temperature for maximum PL efficiency. The annealing temperature is 1100^{o} C.
- Observing the effect of oxide thickness during the fabrication of Si nanocrystals. There is a maximum oxide thickness for a fixed implantation energy for which the

PL intensity is maximum. PL intensity decreases with the further increase of thickness.

- Comparing the effect of oxidation types on PL intensities. Wet oxidation and dry oxidation have different effects at different implantation energies.
- Observing the effect of measurement temperature on PL efficiency. The PL intensity deceases with the increase of measuring temperature.

CHAPTER TWO: REVIEW AND THEORITICAL CONSIDERATION

2.1 Introduction

Presently, due to the wide range of potential applications, Si nanocrystals are a very attractive field in which to work [9-10]. A huge amount of work has been done relating to Si nanocrystals embedded in an SiO_2 matrix, formed via ion implantation; specifically on the effects of implantation doses, implantation energy, annealing temperatures, etc. [1] [11-14]. Among all fabrication techniques ion implantation draws the researchers' interest due to its advantages [1] [8] [10] [12-14].

2.2 Background and Theoretical Consideration

Ion implantation, sputtering, chemical vapor deposition, molecular beam epitaxy, gas evaporation and laser ablation are commonly used techniques for the formation of Si nanocrystals [1] [8] [10] [12-14]. For potential commercial application ion implantation may be suitable due to the precise control afforded for dopant distribution [12] [1] [10]. Ion implantation can control the depth of implanted ions and their concentration by varying the acceleration energy and dose respectively [10]. The distribution may be modeled using software such as SRIM [49].

Post-implantation thermal annealing is essential to form Si nanocrystals embedded in a SiO_2 matrix. Measured PL intensity increases with the increase of annealing temperature above 1000^o C [1] [15]. Below this temperature the Si crystals do not form [1] [15]. However, it is observed that samples annealed less than 900^o C emit light due to

the defects introduced during ion implantation [17]. The annealing characteristic of emission intensity is consistent with the decomposition of SiO_x (silicon-rich SiO_2) which begins at 1000^o C [18-22]. A subsequent hydrogen passivation (through annealing at low temperatures in a hydrogen environment) increases nanocrystal luminescence via passivation of dangling bonds and non-radiative defects [5] [13] [23-25].

2.3 Light Emitting Mechanism

As an indirect band gap material, bulk Si has very low light emission efficiency; however Si nanocrystals have much higher light emission efficiency. There are two theories related to the photoluminescence from Si nanocrystals [5-8] [21] [54-55]. Quantum confinement during the recombination of excitations is the cause said by one theory while the other explains the emission as due to the oxide defects as well as the interface between the silicon and host dielectric.

One dimensional, two dimensional and three dimensional quantum confining volumes are known as quantum well, quantum wire and quantum dot respectively. In the nanostructure, the wave functions of both hole and electron overlap so phonon energy is not needed for light emission (in the case of indirect materials) [2]. Figure 1 shows the transformation of electron energies for direct and indirect semiconductor. For direct semiconductor, when an electron and hole recombine the energy is converted to light (photon energy) as $E_g = h\nu$ (figure 1). But for indirect semiconductor, the valance band maxima and conduction band minima are not at the same k (wave vector) point (figure 1). So for indirect semiconductor, electron hole recombine energies transform as both light

energy i.e. photon energy and phonon energy (figure 1). So light emission from the indirect semiconductor is much less compared to the direct semiconductor. Quantum confinement gives Si nanocrystals the feature of a direct band gap (at least optically).

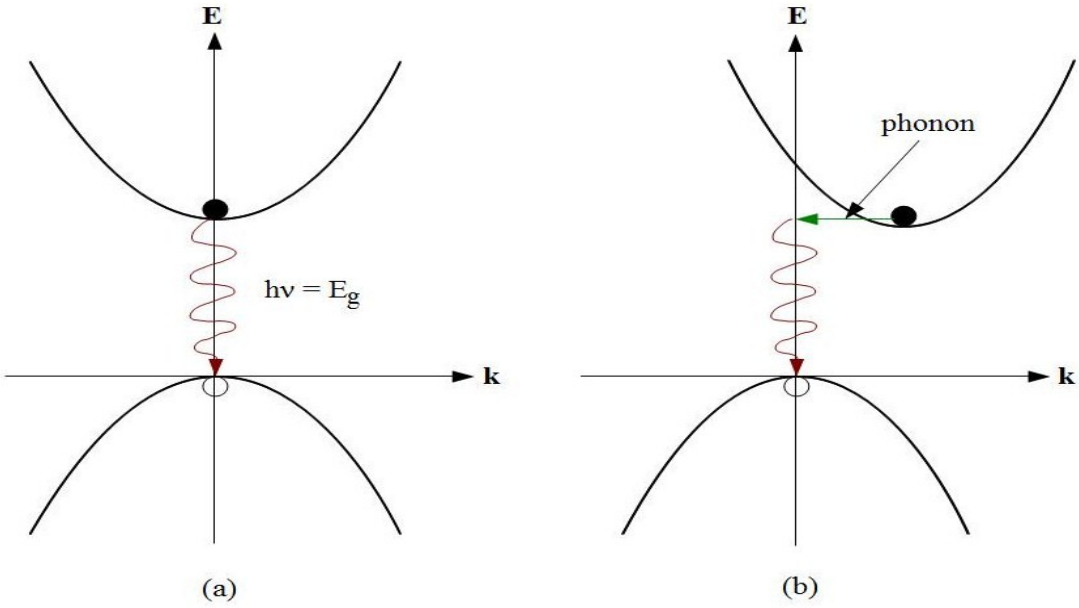

Figure 1: Transfer of energy (a) direct semiconductor (b) indirect semiconductor [2].

2.4 Formation of Si Nanocrystals

Ion implantation is a widely used technique for fabricating Si nanocrystals in an embedded SiO_2 matrix. In ion implantation, the depth profile and concentration can be controlled precisely. The doses and energies of Si ion implantation are in the range of 10^{16} to 10^{17} ions cm^{-2} and 10 KeV to 1MeV respectively [1] [8] [11-12] [15]. But during ion implantation many defects are introduced into the SiO_2 layers. Si nanocrystals are grown by high temperature thermal annealing (subsequent to the implantation) above 1000^{o} C and this annealing essentially removes the implantation induced defects [1] [15].

In general, two types of thermal annealing are used i.e. furnace annealing (FA) for several hours normally in N_2 atmosphere and rapid thermal annealing (RTA) for a short time.

Figure 2 describes the formation of Si nanocrystals during high temperature thermal annealing following ion implantation. The luminescence depends on decomposition, segregation, diffusion, nucleation, aggregation, growth and crystallization. Typically 1000^o C furnace annealing can do all the above steps such that adequate visible photoluminescence is found.

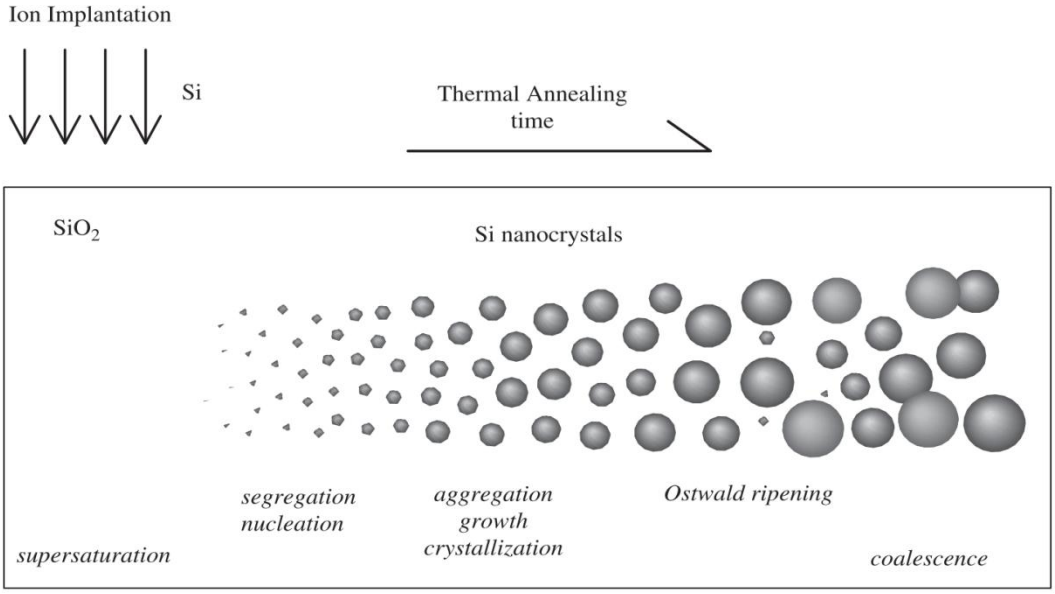

Figure 2: Formation of silicon nanocrystals with annealing process [1].

High resolution electron microscopy (HREM), in the Dark Field mode (DF) has been used to image silicon nanocrystals. The atomic number and density of Si and SiO_2 are nearly the same, so in the images it is very difficult to differentiate Si nanocrystals

from the SiO_2 matrix. The Si nanocrystals whose diameters are less than 1.2 nm cannot be distinguished in high resolution electron microscopy (HERM) images and for dark field (DF), Si nanocrystals of diameter less than 1nm cannot be differentiated from the SiO_2 matrix [3]. Figure 3 and figure 4 show the HERM image and DF image for Si nanocrystals embedded in SiO_2 matrix for the implantation dose and energy of 3×10^{17} ions cm^{-2} and 150 KeV respectively.

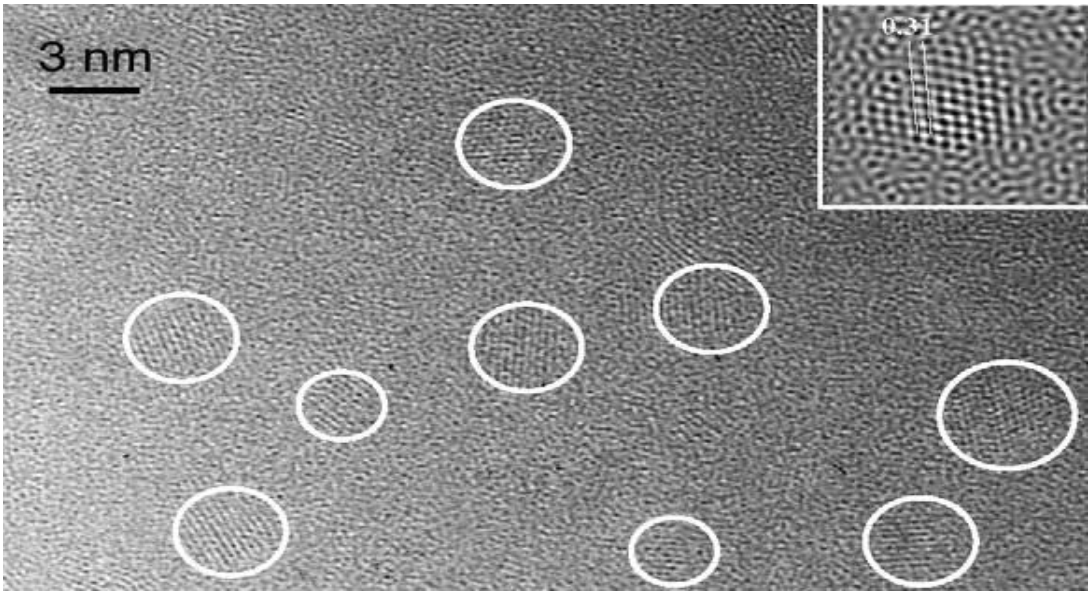

Figure 3: HREM picture of Si nanocrystals embedded on SiO_2 [3]

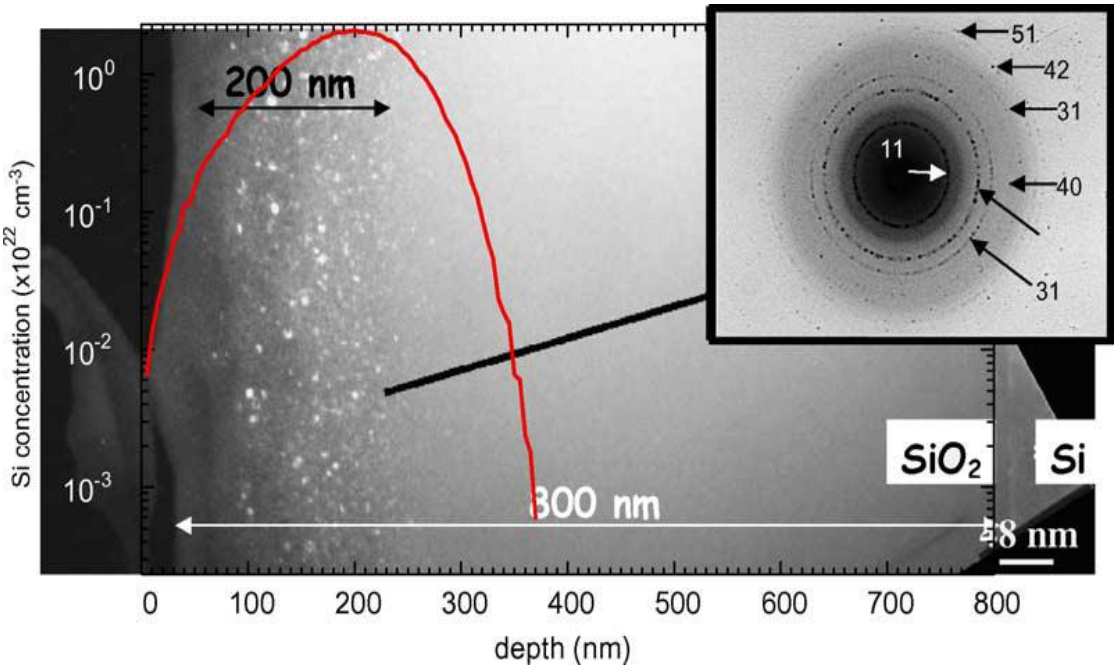

Figure 4: Dark Field picture of Si nanocrystals embedded in SiO_2 . Red line indicating the region where Si nanocrystals were formed [3].

2.5 Improving the PL Efficiency

2.5.1 Eliminating the Defects Caused by Ion Implantation

It is known that for forming Si nanocrystals and obtaining strong photoluminescence the thermal annealing temperature should be more than 1000^{o} C. But from the figure 5, PL intensity was found in the as-implanted sample after 400^{o} C annealing temperature and this occurred due to the defects created during ion implantation. Also, photoluminescence was found after 900^{o} C annealing temperature but this was significantly lower than that after 1000^{o} C.

For as-implanted samples the PL intensity peak is wide and asymmetric. After 400^{o} C and 600^{o} C it is seen that this peak is in fact the overlap of 2 peaks. The first one is at about 1.74 eV and the second one is at about 1.96 eV; while the values of peak energies are not a function of annealing temperature the intensity at the values of them are decreasing with the increase of annealing temperature. In as-implanted samples it is assumed to be no Si nanocrystals so the PL peaks are thus created due to the defect in SiO_2 layer. During ion implantation oxygen type defects occur due to the braking of Si-O bonds in the SiO_2 layer and the ratio of O/Si atoms becomes less than two [19].

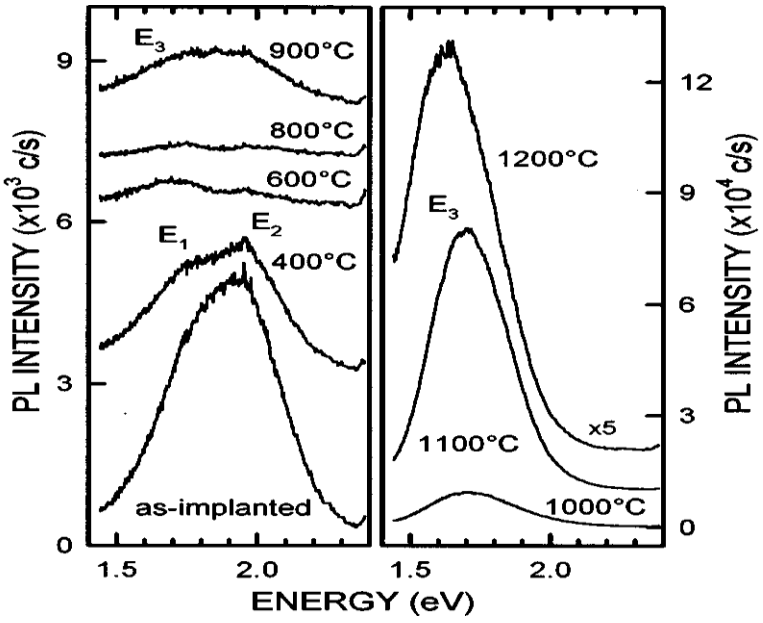

Figure 5: The room temperature PL spectrum of SiO_2/Si structure implanted by Si ions and annealed at different annealed temperature in an N_2 atmosphere for 30 min and the excitation light was 514.5 nm. Here the concentration is flat topped and depth region is 80-290 nm below the oxide surface [17].

Figure 5 and figure 6 reveal new peak energy when the annealing temperature is greater than 900^{o}C and this PL intensity peak increases with the increase of annealing temperature until 1100^{o} C, after which it starts decreasing. The value of this peak energy decreases from 1.84 eV to 1.70 eV when the value of annealing temperature increased but it is approximately flat between 1000^{o} C and 1100^{o} C.

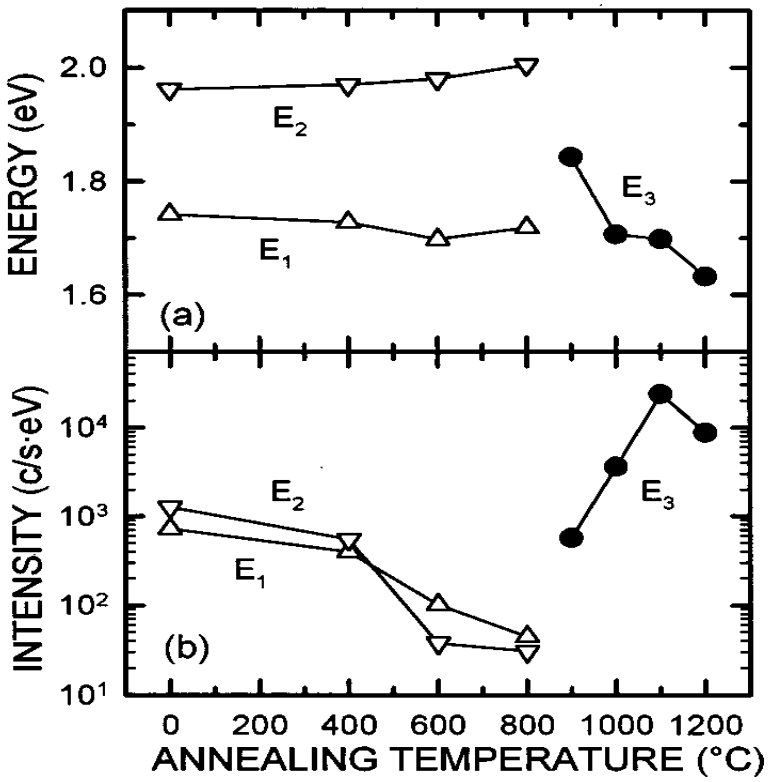

Figure 6: PL peak energy (a) and PL intensity (b) with respect to thermal annealing temperature [17].

2.5.2 Effect of Implantation Ion Doses

The peak position of photoluminescence intensity is dependent on implanted ion dose [1]. For 5.0×10^{16} ions cm^{-2} the peak photon energy is greater than that of the higher dose implantation for the implantation energy of 180 KeV [1]. PL intensity increases with dose but after reaching a maximum the PL intensity decreases. This general behavior is shown in figure 7. For getting measurable light from the Si nanocrystals, the minimum dose is about 1.0×10^{16} ions_cm^{-2} which is found from the experimental results of this thesis and discussed in chapter four.

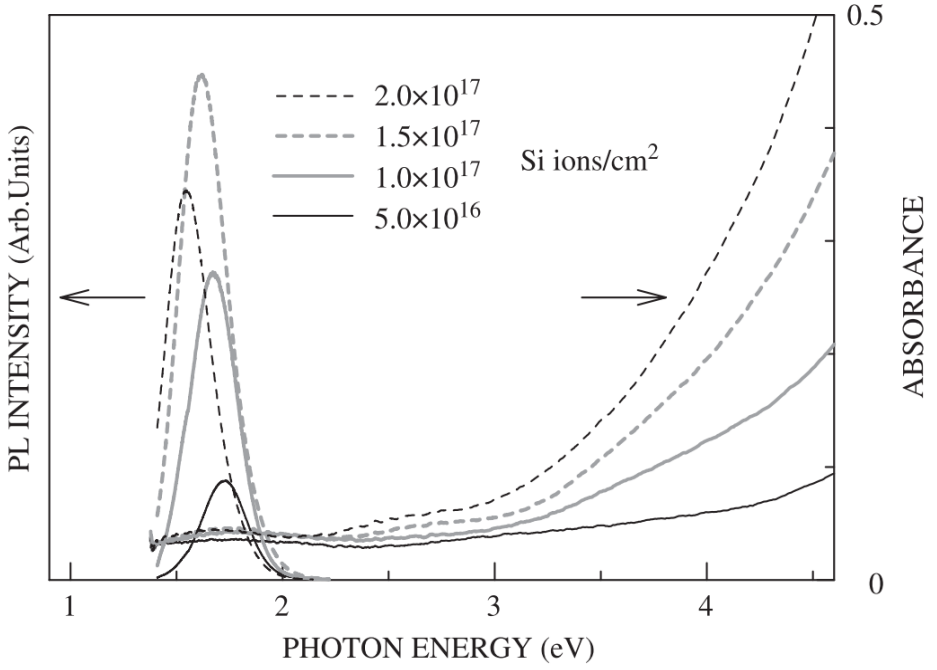

Figure 7: Photoluminescence and optical absopbance spectra of 180 KeV Si implanted 600 nm thermal oxide thin films for different doses, after annealing at 1050^o C for 5h [1].

2.5.3 Effect of Thermal Annealing

Si nanocrystals cannot form before the high temperature thermal annealing following ion implantation. For as-implanted samples the PL intensity is very low and is due to the defect generation during ion implantation [17]. Furnace annealing (FA) below 900^{o} C shows PL intensity similar to that in as-implanted samples [17]. But for temperatures greater than 1000^{o}C, Si nanocrystals are formed and light is emitted. PL intensity increases with the increase of time duration of thermal annealing (figure 8).

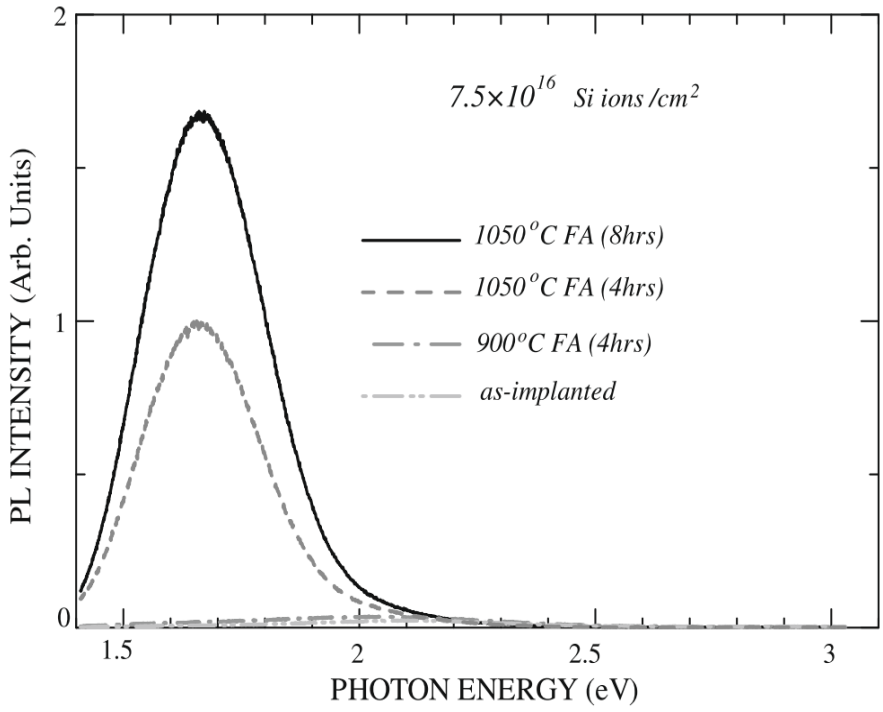

Figure 8: PL intensity of 7.5×10^{16} ions_cm^{-2} dose and 180 KeV sample with respect to photon energy for several house 900^{o} C and 1100^{o} C temperature furnace annealing (FA) [11].

Rapid thermal annealing (RTA) and standard furnace annealing have been used (on the same sample set) following ion implantation. The sequence of these two annealing processes was very significant. Figure 9 and figure 10 reveal that rapid thermal annealing (RTA) followed by furnace annealing (FA) had a higher luminescence intensity peak compared with furnace annealing followed by rapid thermal annealing. While for a 1100^{o}C annealing temperature, the PL intensity was 2 times greater compared with that of 1050^{o} C. PL intensity also depended on the temperature rise rates. The faster the temperatures raise, the more the value of PL intensity peak [1].

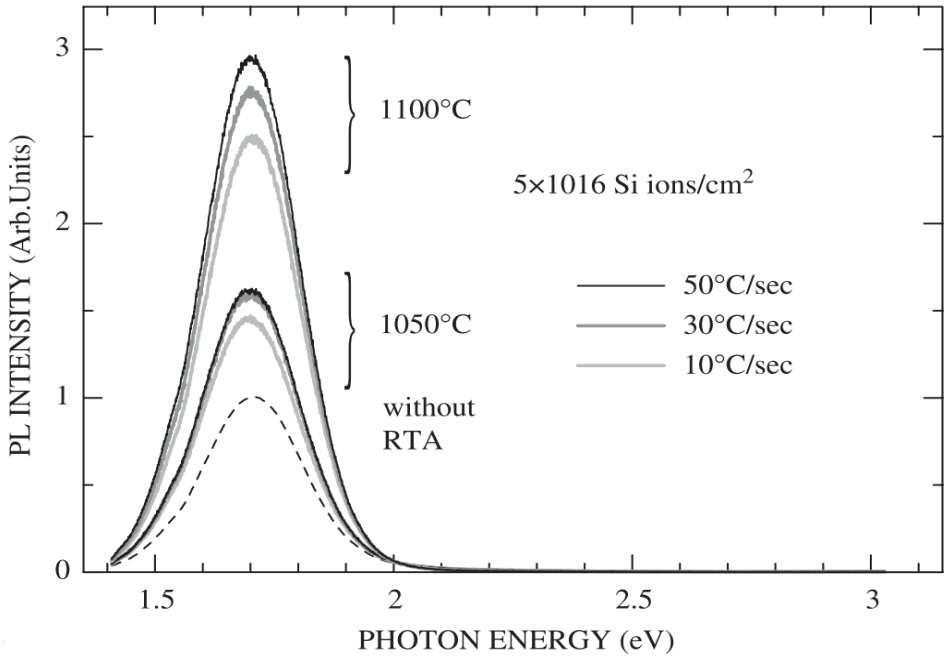

Figure 9: Photoluminescence spectra of samples implanted to dose of 5×10^{16} ions cm^{-2} and first 5 min rapidly thermally annealing with different temperature rise rate for 1050^{o}C 1100^{o} C annealed temperature and then furnace anneal at 1050^{o} C for 1h [1].

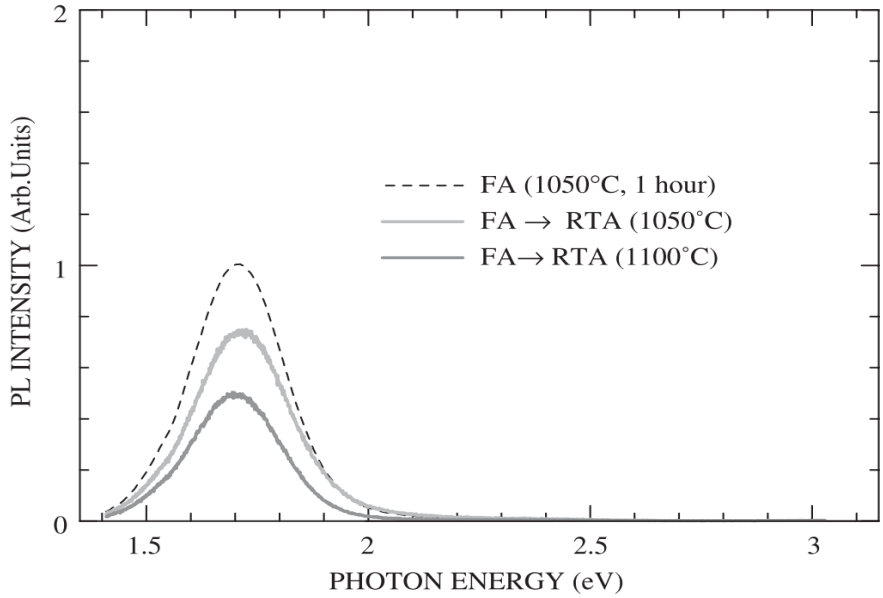

Figure 10: Photoluminescence spectra of samples implanted to dose of 5×10^{16} ions cm^{-2} and first 5 min rapidly thermally annealing with different temperature rise rate for $1050^{o}C$ 1100^{o} C annealed temperature but here first furnace annealing and then rapidly thermal annealing [1].

Sais *et al* described that with the increase of annealing temperature was an increase in the diameter of Si nanocrystals [26]. The PL intensity increases with the increase of diameter of Si nanocrystals, but only to a limit. After the limit the PL intensity decreases with the increase of diameter. At this point the larger diameter Si nanocrystals come so close to one another that they form a silicon continuum. Thus, the number of Si nanocrystals decreases and due to this the PL intensity decreases. Also, larger Si nanocrystals have a lower cross section for optical absorption. So as per figure 11, the PL intensity is low compared to the other two spectrums [26].

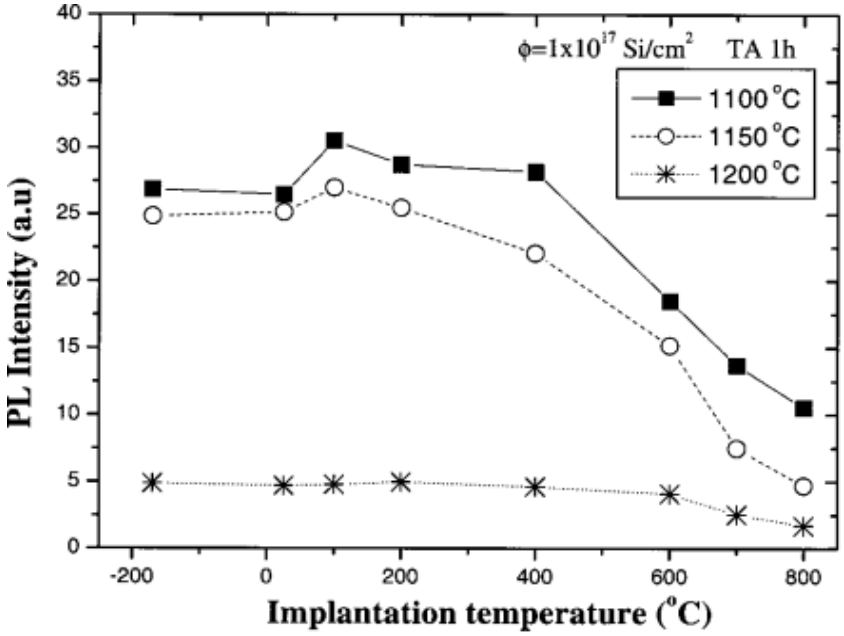

Figure 11: PL intensity versus implantation temperature for samples implanted to a fluence 1×10^{17} Si/cm^2 and thermal annealed for 1 h at temperatures of 1100 °C , 1150 °C, and 1200 °C [26].

2.5.4 Effect of UV Irradiation

UV-light irradiation increases the PL intensity when applied to Si-nanocrystals likely because UV-light irradiation breaks the Si-Si and Si-O bonds which have been shown to have an impact on photoluminescence [11], [16]. Previously, 172nm UV-light irradiation took place for 2 h in vacuum. Figure 12 reveals that such UV-light irradiation increased the PL intensity peak.

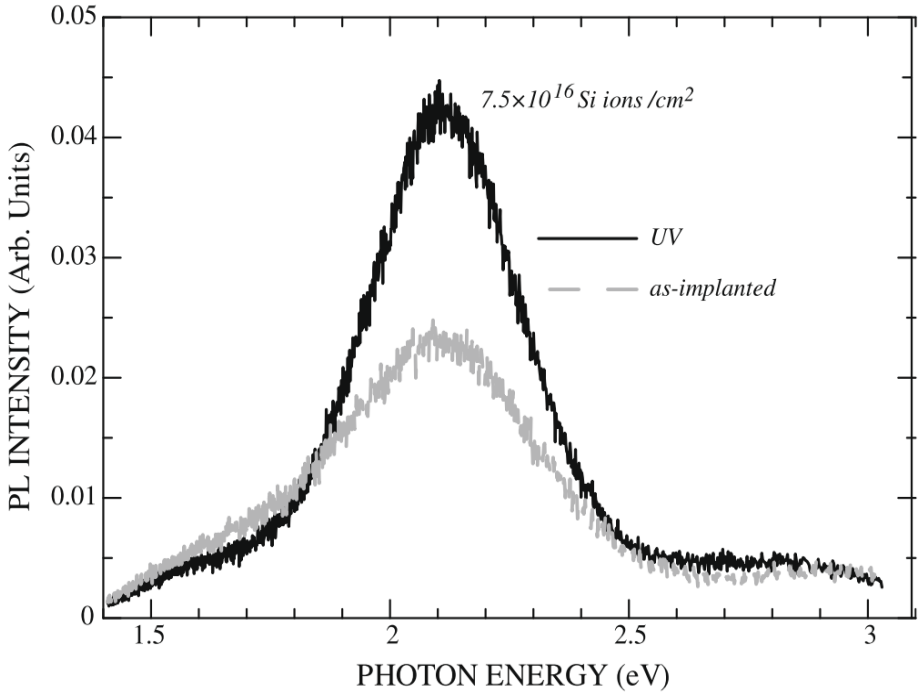

Figure 12: PL intensity spectra of sample implanted with dose 7.5×10^{16} ions_cm^{-2}, before and after UV light irradiated for 2 h in vacuum [11].

2.5.5 Relationship between Implantation Dose and Annealing Temperatures

The relationship between PL intensity enhancements by RTA processing depends on the implantation ion dose [1]. Figure 13 (A) shows that the PL intensity due to doses of 5.0×10^{16} ions_cm^{-2} and 1.0×10^{17} ions_cm^{-2} were 3 times and 1.8 times increased respectively with RTA compared with that without RTA (i.e. those that received furnace annealing only). So the effective increase of PL peak is about 2 units and 0.8 units respectively with RTA.

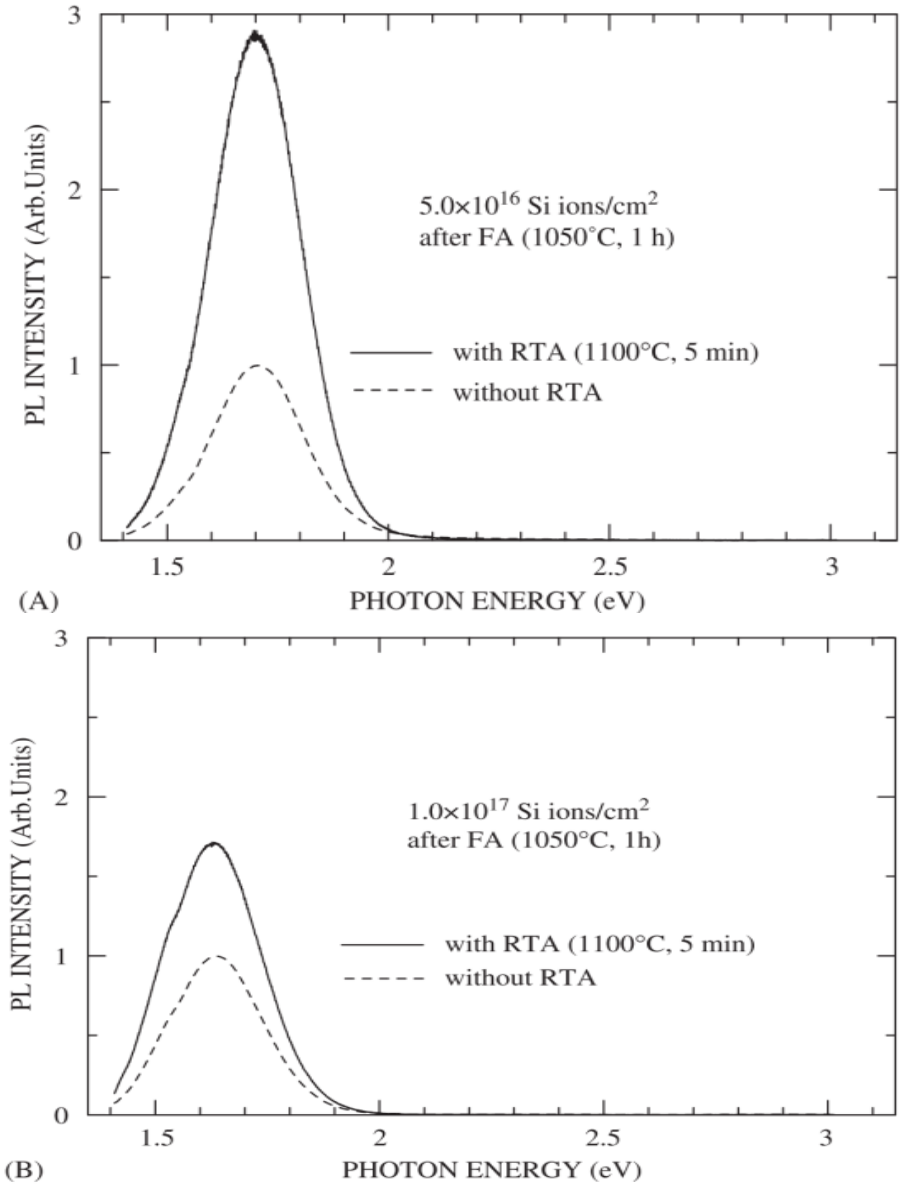

Figure 13: Photoluminescence spectra of samples implanted to doses of (A) 5.0×10^{16} ions_cm^{-2} (B) 1.0×10^{17} ions_cm^{-2}, first rapidly thermally annealed at 1100^{o}C for 5 min with temperature rise rate of 30^{o} C/sec and then furnace anneal at 1050^{o} C for 1h. The dashes line shows the spectrum only for furnace annealing [11].

Figure 14 reveals the relationship between PL intensity and Si ion doses at 1100^{o} C, rapidly thermal annealed for 5 min prior to furnace anneal at 1050^{o} C for 1h. It was

found that the RTA was more effective during the initial stages such as decomposition and segregation. In RTA the temperature rises within a very short time such as 50^{o} C/sec and due to the short time the diffusion of implanted Si is limited. A little aggregation forms because of the diffusion limited segregation and the small aggregations behave like a nucleation point. When the implanted Si ions increase they try to form small aggregates without RTA or FA. RTA is also doing the same thing.

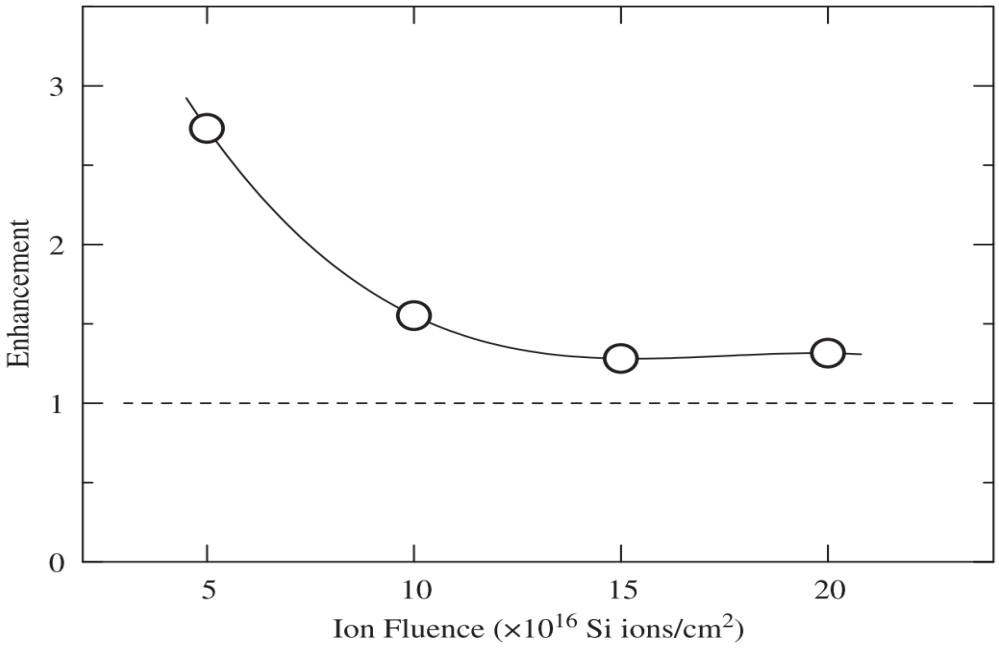

Figure 14: Enhancement of photoluminescence intensity as a function of implanted Si ion doses [15].

2.5.6 Relationship between Annealing Time Duration, Mean Radius and Lifetime

The diameter of Si nanocrystals is increased with the increase of annealing time [1] [3] [11] [56]. Figure 15 reveals the relationship between Si nanocrystal diameter and annealing time for 1100^{o} C annealing temperature for 10% to 30% excess Si. The diameter increases very slowly over the time duration, nearly 15% from 1min to 16 h. Due to the low diffusion coefficient of Si in SiO_2 and asymptotic Ostwald ripening growth stage of Si nanocrystals the diameter is almost constant at 1100^{o} C annealing temperature [10]. Annealing after 16h, the diameter for 10% excess Si was 3 nm and for 30% excess Si was 5.5 nm. The result can be explained with the overlapping theory of excess Si to neighbor nanocrystals [3]. Such larger diameter Si nanocrystals are formed via merging with neighboring Si nanocrystals.

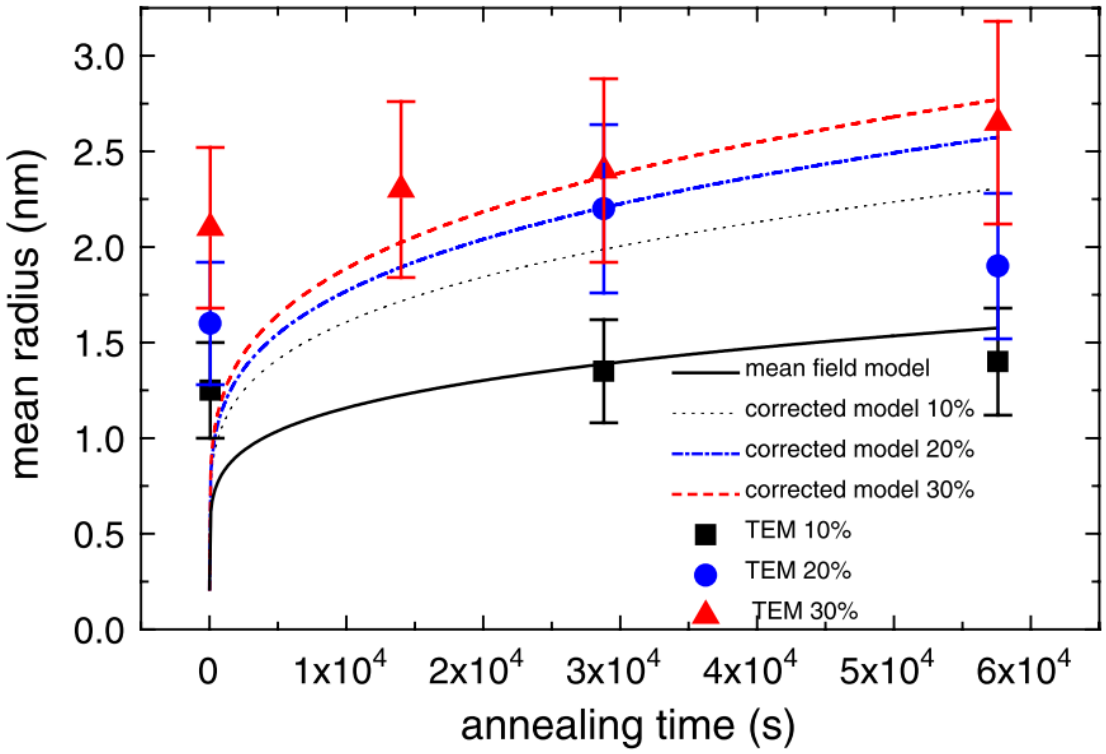

Figure 15: Diameter or mean radius with respect to annealing time graph was plotted for 10% to 30% excess Si at annealing temperature 1100^{o} C. The solid lines are simulations compared to the experimental points [3].

2.5.7 Role of Vacancy Type Defects on Si Nanocrystals

Primary vacancy creation has been shown to have an impact on Si nanocrystal size distribution.

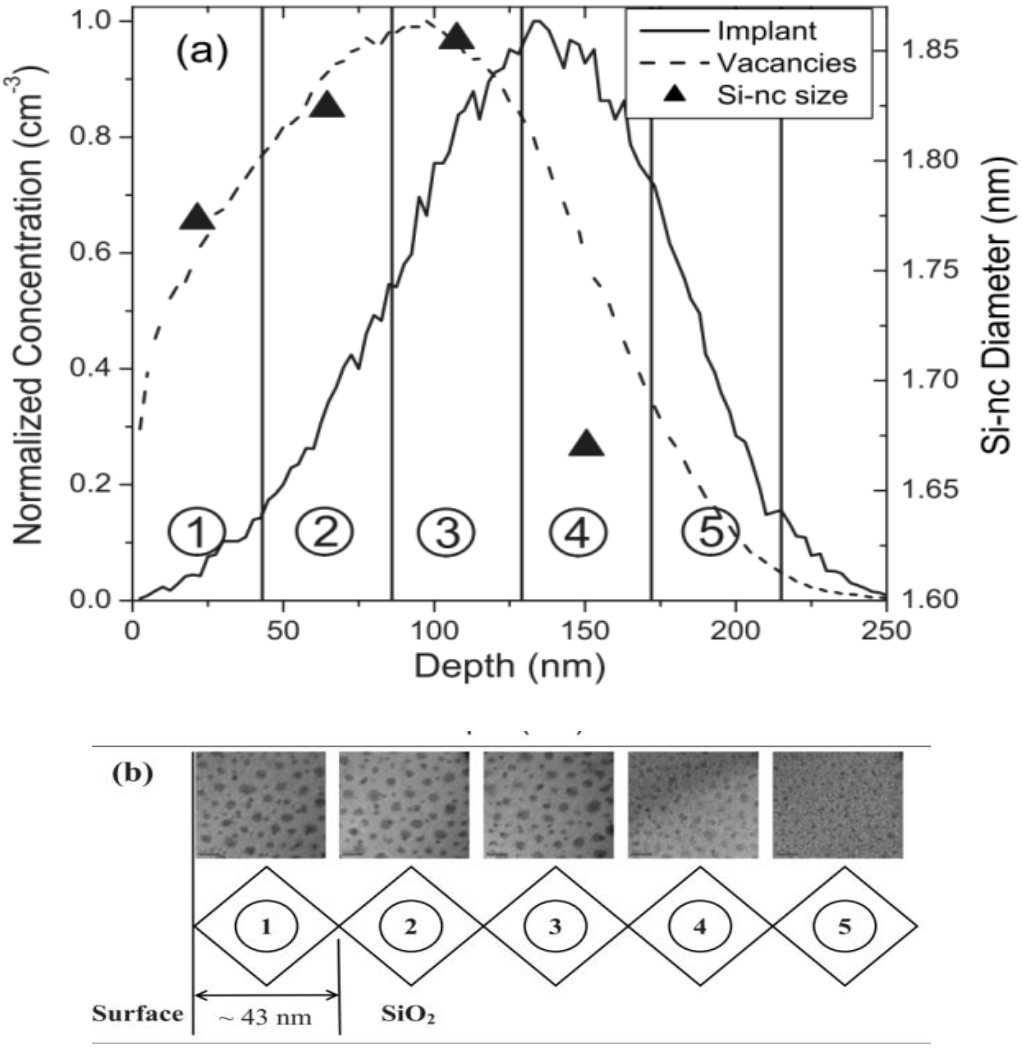

Figure 16: (a) Simulation routine stopping and range of ions in matter (SRIM) simulation for dose of 1.4×10^{17} ions_cm^{-2} energy 90 KeV. Implantation profile and vacancy distribution plotted with respect to the mean of Si nanocrystals (b) TEM images for different region of figure 16 (a) [10].

Figure 16 reveals the implanted ion profile, vacancy distribution and size of Si nanocrystals for the implantation dose and energy of 1.4×10^{17} ions_cm^{-2} and 90 KeV respectively. TEM images are used to find Si nanocrystal location and distribution after annealing at 1070° C for a total of 3 h. The implant profiles, vacancy distribution and size

of nanocrystals were increased with the increase of depth till a certain region and after that region the values were decreased. Table.1 shows the mean and median values of diameter of Si nanocrystals for different TEM image locations. It was found that the nanocrystal size was increasing till the depth of 135 nm for the specific implantation energy. At the thickness between 180-225 nm, the size of nanocrystals was so small that it could not be seen i.e. there was no Si nanocrystals or they were smaller than 1 nm.

TEM image location	SiO_x depth (nm)	Median Si-nc diameter (nm)	Mean Si-nc diameter (nm)
1	0-45	1.71	1.77±0.05
2	45-90	1.79	1.82±0.05
3	90-135	1.82	1.86±0.05
4	135-180	1.61	1.67±0.05
5	180-225	Too small to distinguis	Too small to distinguis

Table.1: Median and mean Si-nc size as a function of depth for silicon ions implanted to a dose of 1.4×10^{17} ions_cm^{-2} into a 430 nm thick oxide and annealed at 1070 °C for a total of 3 h [10].

Figure 17 (a) and (b) shows the normalized implanted ion concentration with respect to depth, and the normalized vacancy concentration. Here, two types of implantation energy were used i.e. 450 KeV and 90 KeV. The figure reveals that the vacancy type defects greatly depend on implantation energy [10]. PL intensity with respect to wavelength for three samples is plotted in figure 17 (c). For sample A the implantation energy was 450 KeV and dose was 1×10^{17} ions_cm^{-2}, for sample B the

implantation energy was 90 KeV and dose was 3×10^{16} ions_cm^{-2}, for sample C the implantation energies and doses were 450 KeV and 1×10^{17} ions_cm^{-2} followed by 90 KeV and 3×10^{16} ions_cm^{-2}. The PL intensity for sample C was about double than that of sample A and PL intensity peak wavelength of sample C was red shifted with respect to sample B. This indicates that the PL intensity i.e. the growth of Si nanocrystals was dependent on the vacancy type defects. The PL intensity spectrum shape of sample A and sample C was similar but sample C had more vacancy type defects due to their implantation energies and doses compared to sample A. PL intensity appears to thus increase with the increase of vacancy type defects.

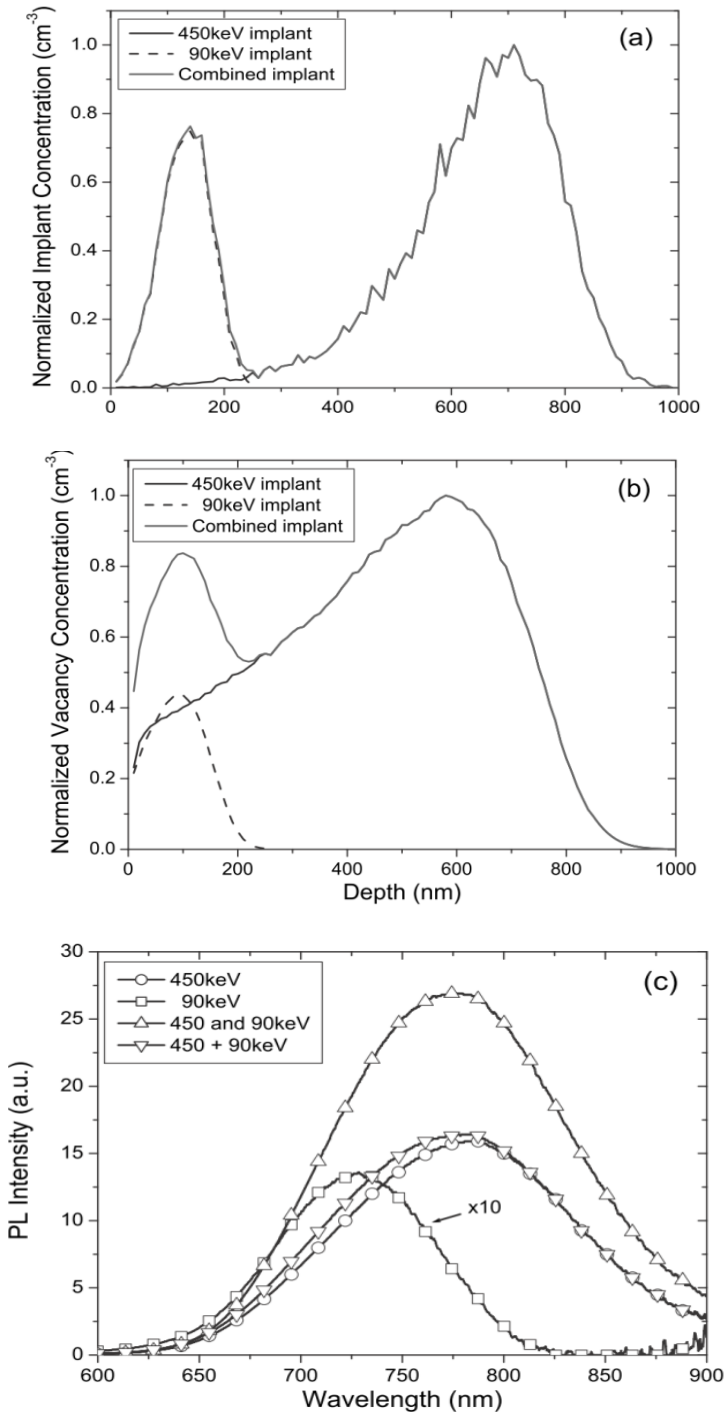

Figure 17: SRIM simulations of a 450 KeV implant at 1×10^{17} ions_cm^{-2} and a 90 KeV implant at 3×10^{16} ions_cm^{-2}. (a) Normalize ion concentration, (b) normalized vacancies concentration and (c) PL intensity spectrum are plotted [10].

2.5.8 Effect of H_2 Passivation

Hydrogen passivation increases significantly the PL from silicon nanocrystals [5] [23-25] [27]. H_2 passivation by using forming gas is a popular method to achieve this. In reference [24] the authors found that forming gas treatment had a great influence on PL intensity of Si nanocrystals.

Figure 18 and figure 19 show the impact of forming gas in the process of making Si nanocrystals. If the temperature and the time duration of the forming gas anneal were increased the PL intensity will also increase.

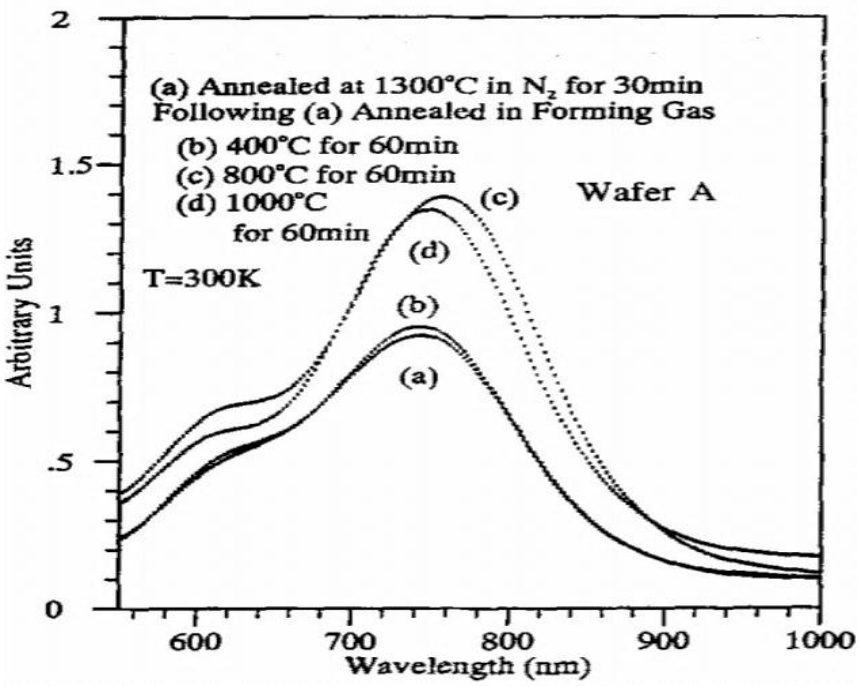

Figure 18: The impact of forming gas for different temperatures for fixed time duration The sample first annealed at 1300^o C in N_2 atmosphere for 30 min [24].

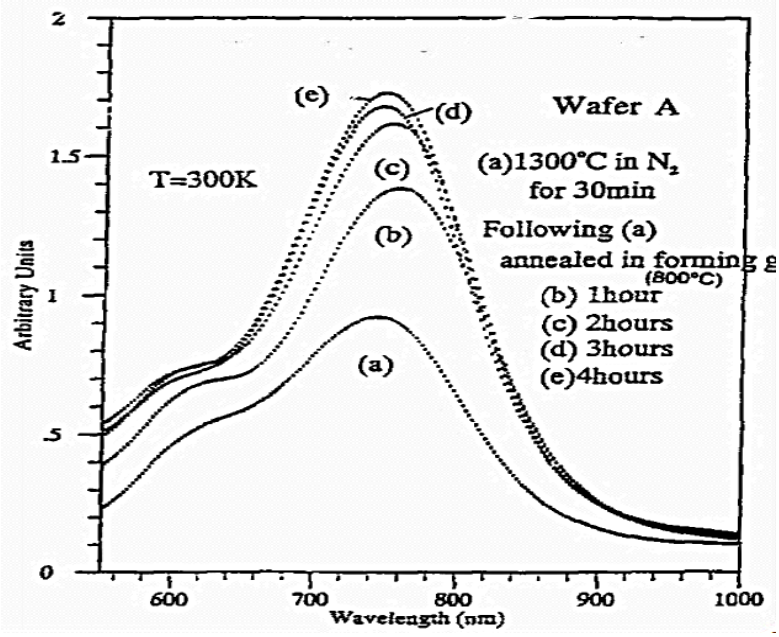

Figure 19: The impact of forming gas for different temperatures for fixed temperature but different time duration. The sample first annealed at 1300^o C in N_2 atmosphere for 30 min [24].

2.5.9 Effect of Oxidation Type

Tetelbaum *et. al.* found that a wet oxidation sample had PL intensity with two peaks at 770 nm and 880 nm (Figure 20). The group used 150 KeV as implantation energy. There were two theories for the origin of the peak about 770 nm; one group said that it was due to the interband recombination i.e. transition inside nanocrystal [59-61]; other group said that it was due to the recombination of excitations which was formed in a nanocrystal with the boundary region states [59] [62-64]. Water vapour present at interface states was responsible for the peak at 880 nm [59]. Flowing air at 1000^o C temperature could not remove the peak but 1100^o C removed the peak at 880nm (Figure 21) [59].

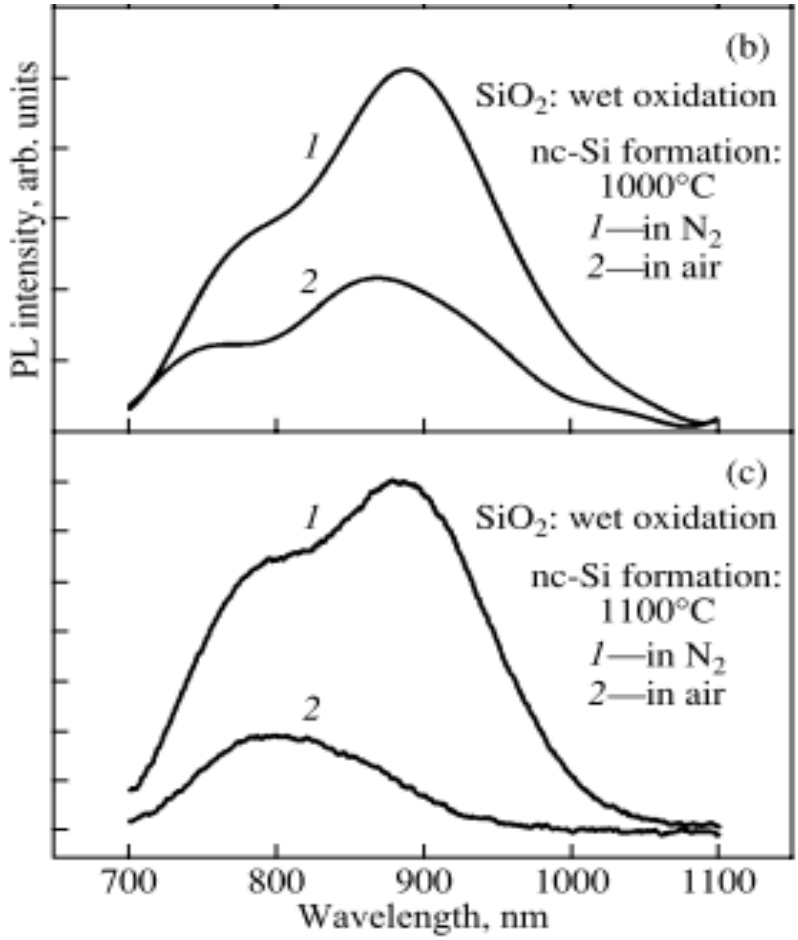

Figure 20: Wavelength dependence of PL intensity for wet oxidation at two annealing condition (N_2 and air) are shown for two annealing temperatue where the implantation dose 10^{17} ions_cm^{-2} [59].

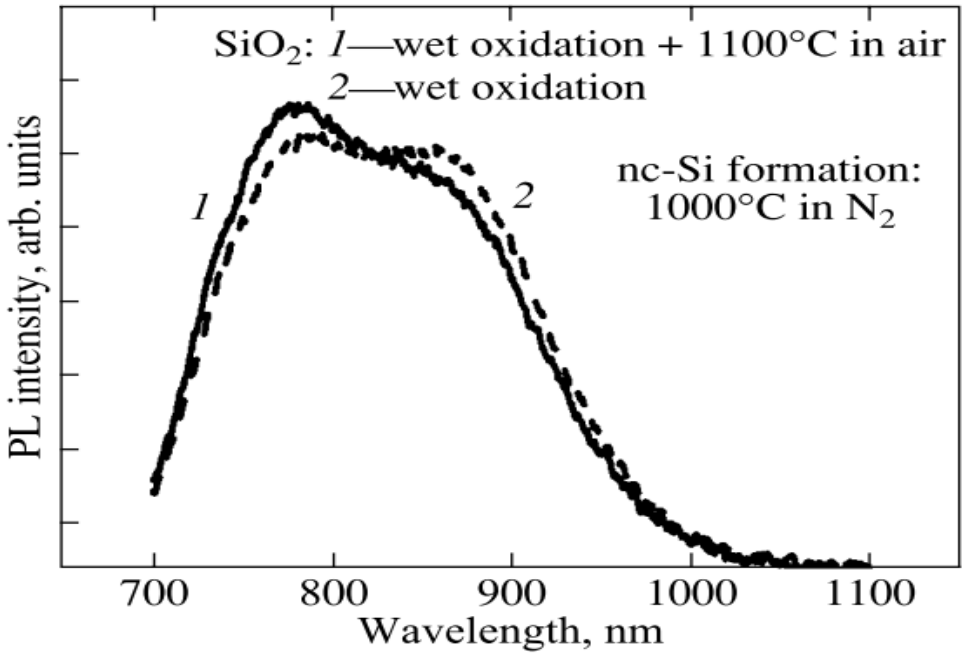

Figure 21: PL intensity vs wavelength graph for only wet oxidation and high temperature air flowing at 1100^{o}C. Here the dose was 10^{17}ions_cm^{-2} [59].

The group proposed a model for dry and wet oxidation shown in figure 22. According to this model, excitons formed in the nanocrystals and recombined through interband transition which was responsible for the PL intensity peak at 770 nm and interface region states captures electron and hole from nanocrystals. The recombination is radiative and responsible for the PL peak at 880 nm [59].

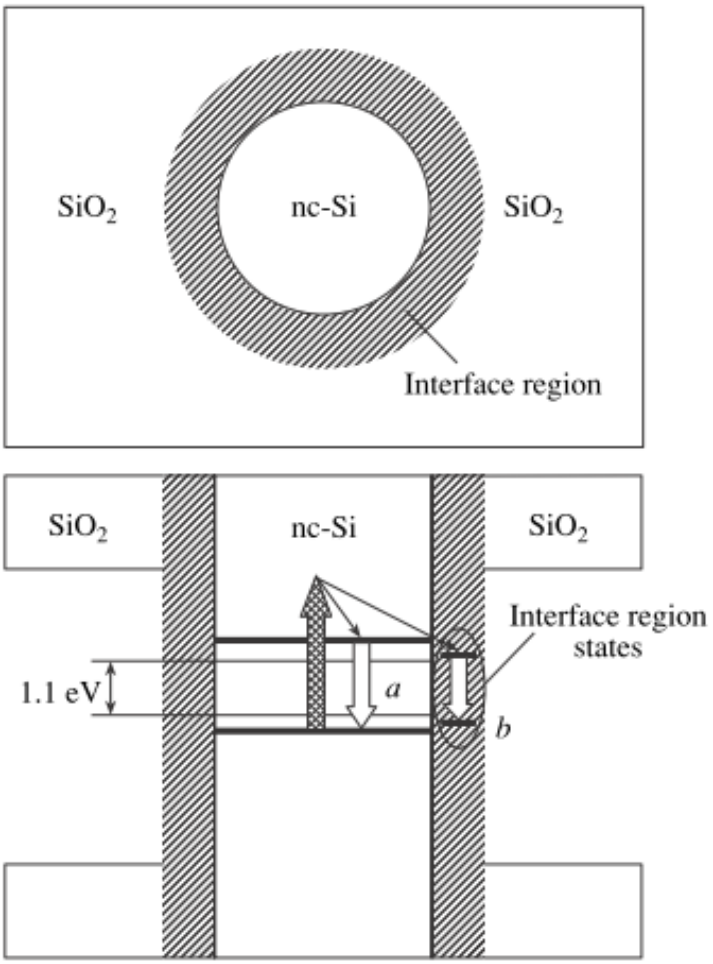

Figure 22: A model of light emission from Si nanocrystals. (a) is responsible for ~770 nm peak and (b) is responsible for ~880 nm peak [59].

2.6 Conclusion

The photoluminescence of silicon nanocrystals is a function of many process parameters when they are formed by ion implantation and annealing. After Si ion implantation in SiO_2 high temperature annealing must be performed. If furnace annealing (FA) is done before rapid thermal annealing (RTA), the photoluminescence is less than

compared to that of only FA annealing for any FA temperatures. The PL intensity increases with the increase of FA temperature until 1100^{o} C after which the PL intensity decreases due to the larger diameter i.e. low absorption cross-section of Si nanocrystals. Minimum implantation dose for fabricating Si nanocrystals is 1×10^{16} ions cm^{-2} (also experimental result of this thesis) which is required for making Si cluster with the radius greater than critical radius for joining the surrounding implanted Si ions [48].

Light emission is found from as-implanted samples- the reason being due to defects in SiO_2 layers formed during ion implantation. Hydrogen passivation is also important for enhancing the photoluminescence.

CHAPTER THREE: EXPERIMENTAL

3.1 Introduction

Several practical instruments and simulating software were used during this research work. Ion implanter, rapid thermal annealer and photoluminescence (PL) set up were the primary experimental tools. Ion implanter was used at the very beginning of the fabrication process followed by rapid thermal annealer, while the PL set-up was used to characterize the samples. In the following chapter the working principal and operational procedures are described.

3.2 Doping

Doping is a very common and important feature for semiconductor technology as well as the integrated circuit (IC) industry. Although not the primary focus of this research, doping has driven the development of ion implantation which is central to this work. It is appropriate therefore to outline the physical principals of doping in this section.

Intrinsic and extrinsic describe two types of semiconductor. In an intrinsic semiconductor the number of electrons and holes are equal. Undoped Si is normally an intrinsic semiconductor. When energy is provided to Si, the electrons from the valence band are promoted to the conduction band. Valance band electrons which go to conduction band, leave holes in the valance band, resulting in this equivalency of holes and electrons (Figure 23).

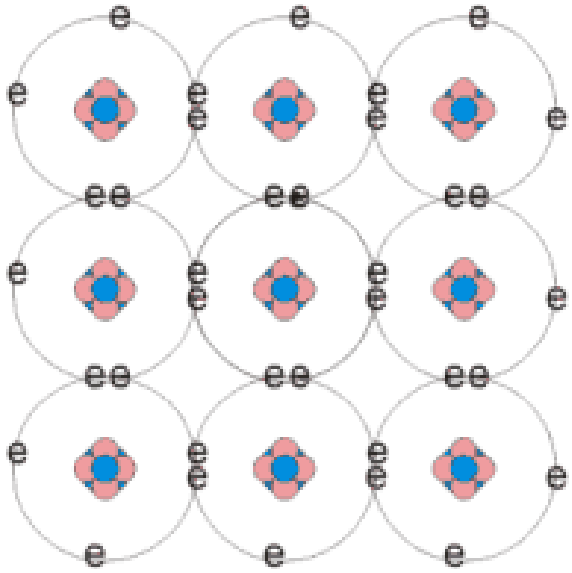

Figure 23: Intrinsic semiconductor at which number of electons and holes are same. Every e represents electon in orbits [28].

If silicon is doped with a group V material, then it is called n-type doping in Si. For example when Si is doped with As which has five valence electrons four Si electrons make covalent bonds with four As electrons while one electron remains unbounded, orbiting the As^{+} much like a single hydrogen atom. If sufficient energy is provided, then this electron becomes free from the As. Normally the energy for excitation of a hydrogen atom is 13.6 eV but in the case of doped silicon we have to consider the relative dielectric field and effective energy so the energy will be different [29]. In n-type doping free electrons are charge carriers and the doped atoms are known as donor atoms. Figure 24 shows an n-type semiconductor.

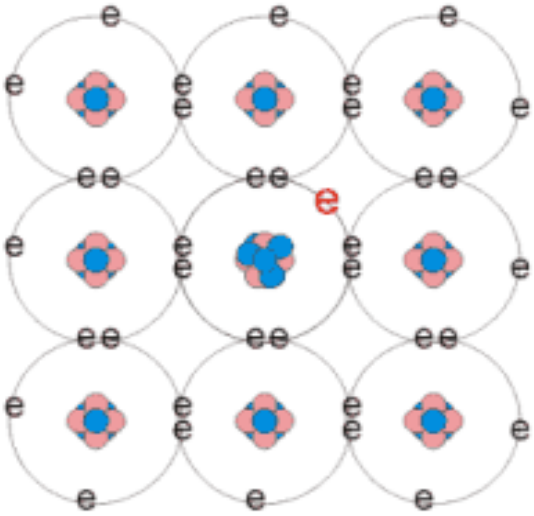

Figure 24: n-type semiconductor at which the number of electon is higher than that of holes i.e. they have extra electron as major carrier. The red e indicates an extra electon [28].

In p-type doping, group III materials are placed in Si. Group III materials are known as trivalent atoms. When silicon is doped with trivalent atoms such as boron, a hole is created due to the presence of only three valance electrons. Then a neighboring electron comes to the hole and the hole goes away from the B atom. The binding energy is near to 0.05 eV. The thermal vibration can free the electrons from B at room temperature. This boron atom is known as acceptor impurity. In p-type doping free holes are carrier [30]. Figure 25 shows a p type semiconductor.

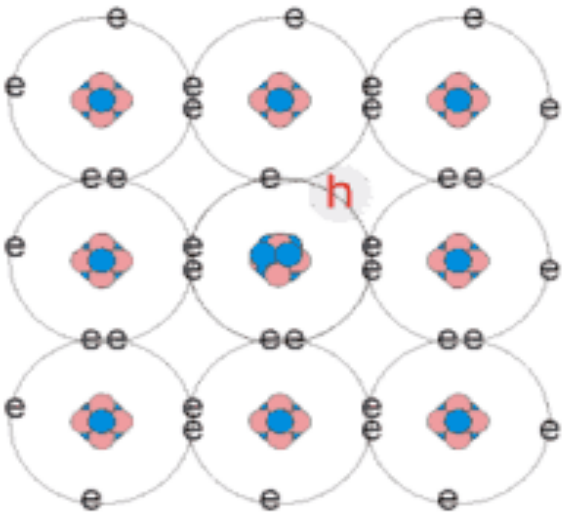

Figure 25: P-type semiconductor at which the number of hole is higher than that of electron i.e. they have extra hole as major carrier. The red h indicates an extra hole [28].

3.3 Ion Implantation

Ion implantation is the most common method for achieving doping. It has huge importance in the semiconductor industry. Today's integrated circuit (IC) has many components and ion implantation is needed for fabrication of these parts and for the precise control of feature sizes of the IC (Figure 26). The increasing requirement for process control is summarized nicely in figure 27. The numbers of bits per chip has increased such that today a Si IC can store as much information as an encyclopedia.

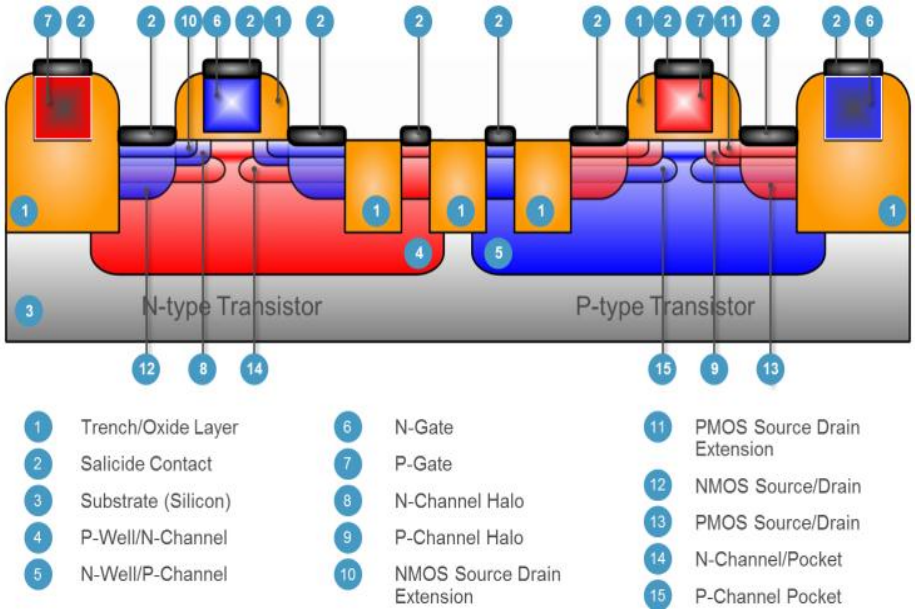

Figure 26: Elements at present IC which need several implant process [31-33].

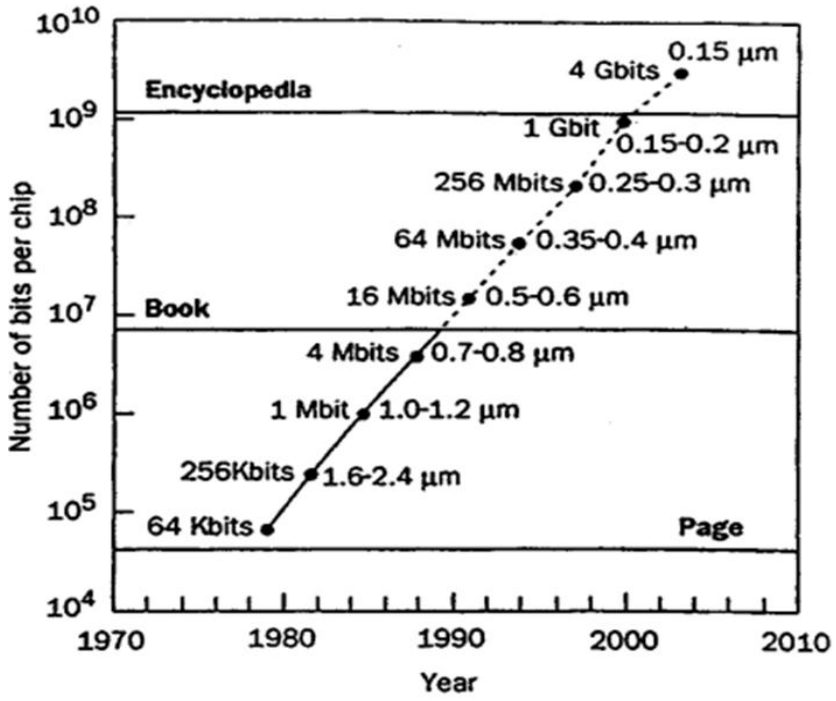

Figure 27: The number of bits per chip with respest to year is plotted which is exponential shaped [34].

An ion is a charged atom whose nature and amount of charge depends on the numbers of protons and electrons of that specific atom. If the numbers of protons are greater than the number of electrons, then the atom is known as a positively charged ion. The reverse is the case for negatively charged ions. During ion implantation ions are launched into a wafer using a forceful electric field [31-33]. The properties of the target material is thus changed- in the case of electrical doping the electrical properties are modified dependent on the concentration of p type or n type ions implanted into the material [31-33]. The implantation energy is determined by the accelerating potential of the ion implanter and is determined by the required specific depth of modification [31-33].

In a modern fabrication process a number of ions may be used: silicon (Si), arsenic (As), nitrogen (N), phosphorus (P), antimony (Sb), boron (B), hydrogen (H), boron difluoride (BF_2), indium (In), germanium (Ge) and helium (He) [35]. The commonly used elements as dopant are shown at figure 28.

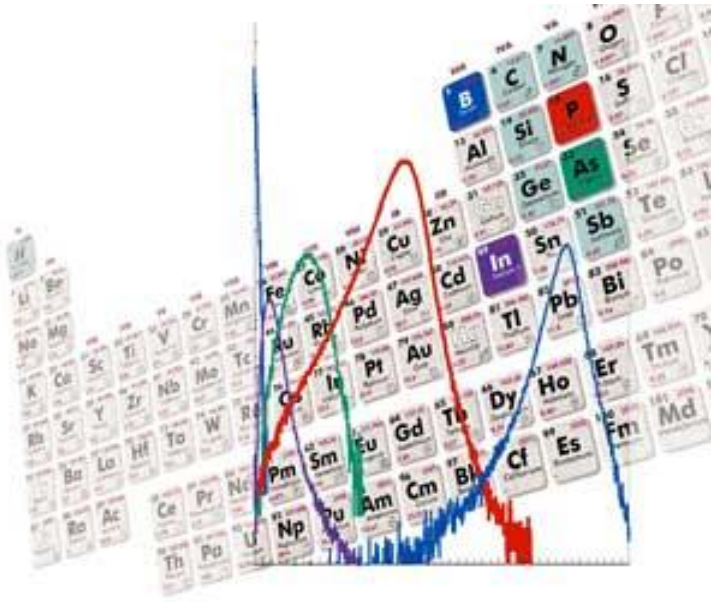

Figure 28: Highlited atoms are commonly used as doping atoms by ion inplanter [35].

3.3.1 Operation of Ion Implanter

An ion implanter consists of an ionization chamber or ion source; ion accelerator and target chamber. At the ionization chamber, the ions which are to be implanted into the target are produced; in the accelerator these ions achieve high energy due to the electrostatic acceleration; and in the target chamber the ions are implanted into the target as shown in figure 29 and figure 30. The total number of ions or atoms implanted is known as the ion dose. Ion implantation may cause either chemical or structural changes in target [17] [36].

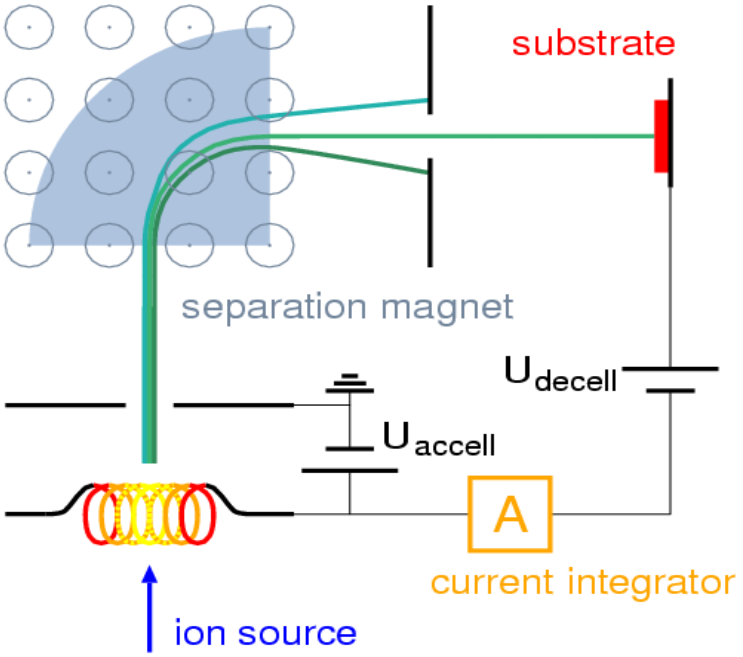

Figure 29: Basic overview of ion implanter [52-53].

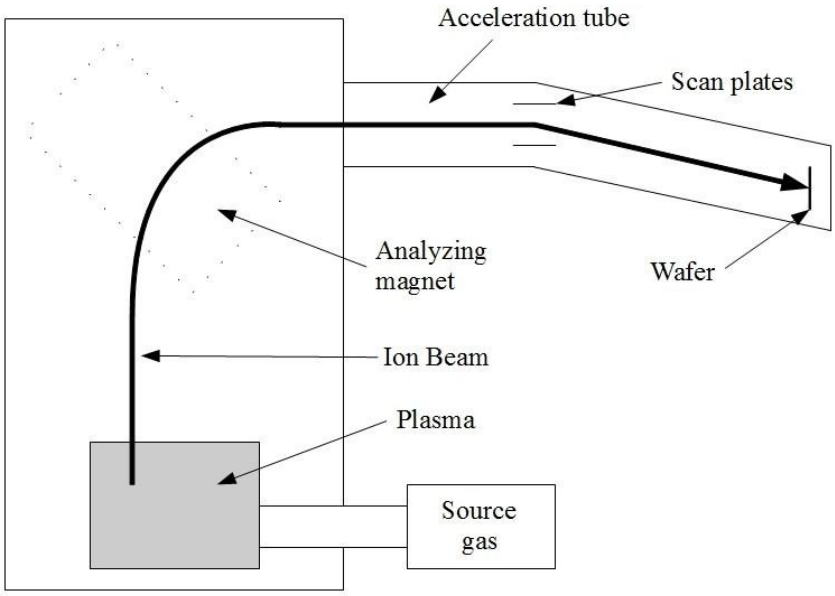

Figure 30: Detail figure of ion implanter [2]

An analyzer magnet is used to choose the correct ions from all those generated in the source chamber (Figure 30) [2]. Ion mass and charge are the selecting factors [31-33]. The ions with the required mass, charge and energy pass through the aperture. Ions with lighter mass, higher charge or less energy are bent more in the analyzer; while ions with heavier mass, lower charge or more energy are bent less and are stopped by the specific aperture in the analyzer magnet (Figure 31) [31-33].

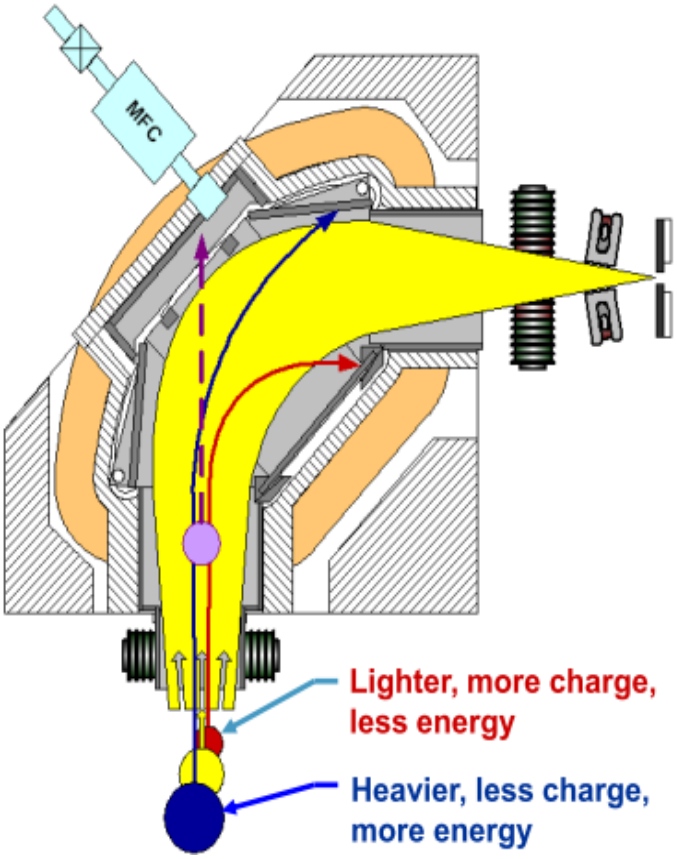

Figure 31: Desired ions with specific weight, charge and energy are passed through the aperture due to the set magnet current [31-33].

Electrostatic lenses perform the important task of spreading the ion beam uniformly over the target material surface. Finally faraday cups (or in other cases the target itself) measure the number of implanted ions [31-33].

3.3.2 Typical Implanted Doses and Implanted Energies

Typically the energy range in ion implantation is 10 to 200 KeV but 3 MeV ion implanters also can be found [11] [17] [31-33]. For higher energy the penetration depth is high. Generally four types of implanter exist: high current/ high dose, plasma doping/ultra high dose, medium current/low dose and high energy/ low dose are found (Figure 32).

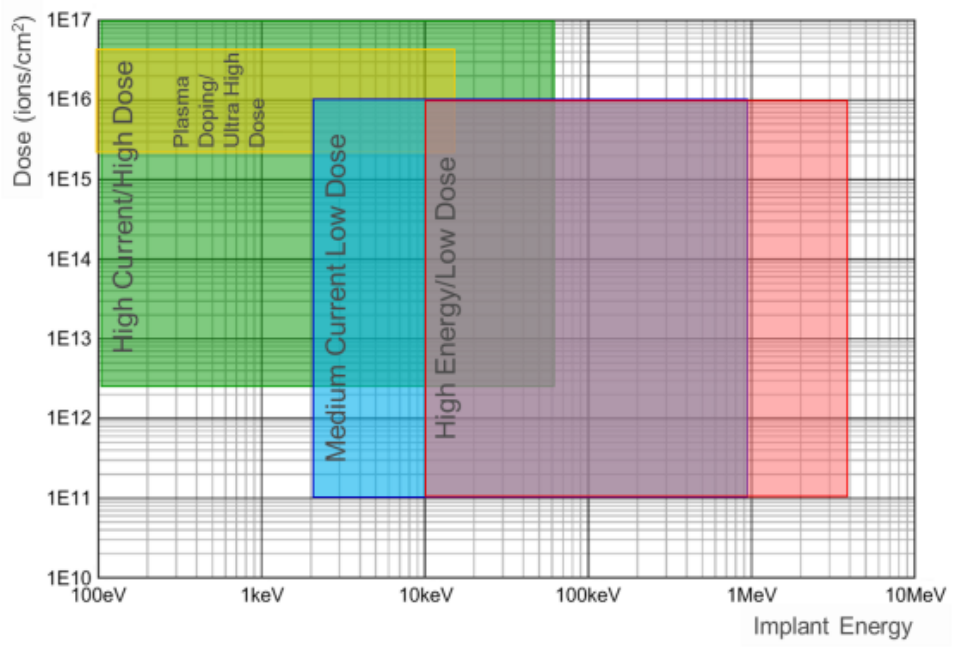

Figure 32 : Log paper diagram for the ranges of implantation doses and energies for four different implant system [31-33].

The various applications of different energies and doses in a standard silicon device build are summarized in figure 33.

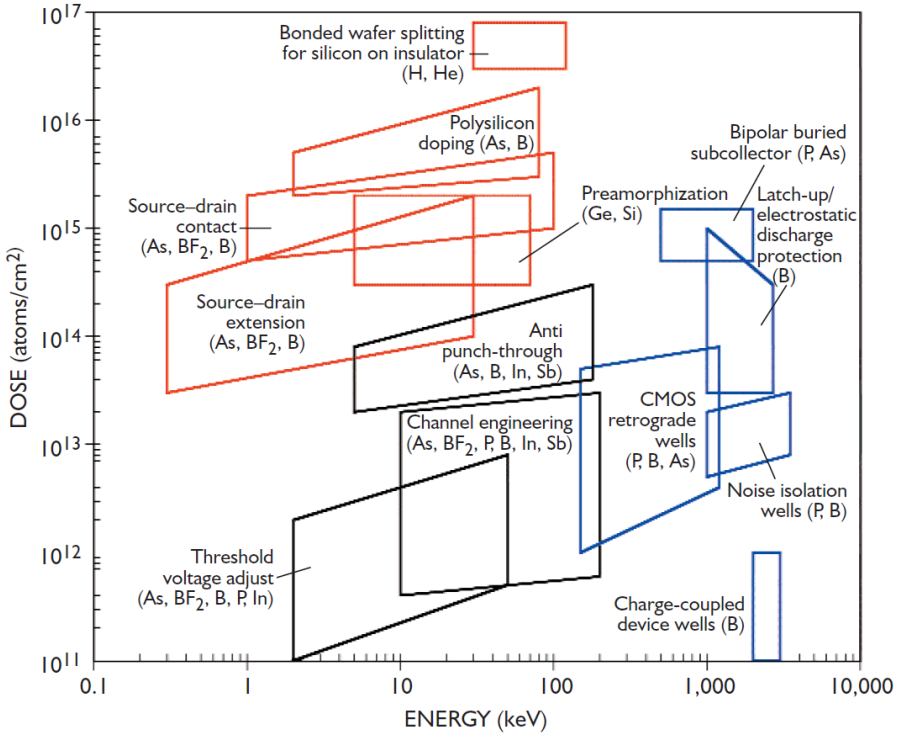

Figure 33: Implanted energy vs dose graph for ion implantation demonstrating the variety of applications in a silicon device build [35].

The high cost of ion implantation equipment is off-set by its utility in device fabrication and its excellent control of implantation dose and profile; uniformity of doping throughout the target materials; and its cleanliness (it is performed in vacuum) [37].

3.4 Rapid Thermal Annealer

After ion implantation, lots of damage is produced in the target. High temperature annealing removes most of these defects. Rapid thermal annealing (RTA) is one kind of annealing and is defined as a process where the thermal load is limited to seconds or minutes. [2] [38-41].

3.4.1 RTA Structure and Working Procedure

JetFirst 100 RTP at McMaster University was used for the annealing work. The main parts of the RTP are reflector, halogen lamps, quartz window, process chamber, wafer stand, exhaust and pyrometer as shown at figure 34 [2] [40]. For the heating purpose 12 tube-shaped halogen lamps are used. The wafer is placed to the process chamber on the wafer holder. The wafer got infrared radiation from the halogen lamps. The pyrometer is used to measure the temperature. Quartz window is used to divide the halogen lamps from the process chamber. For the lamp cooling purpose, circulating water is used [2] [40].

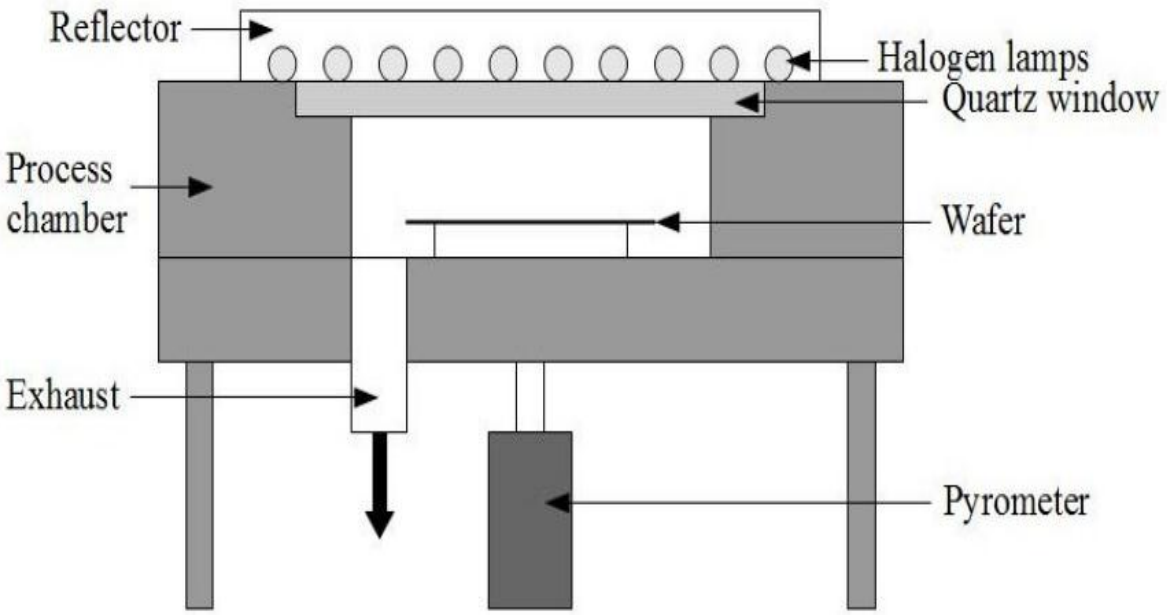

Figure 34: Basic diagram for JetFirst 100 RTP at McMaster University [2].

At the beginning of the process, the sample is placed into the process chamber. After closing the door of RTP, N_2 gas flows with a duration of several minutes at 20^o C temperature at 1000 sccm to remove the moisture and unwanted dust or impurities. Then annealing starts according to the recipe and after the end of annealing, RTA needs several minutes (4 minutes for 100 Jetfirst RTA) to cool down at room temperature. Several steady steps are used to avoid the power spikes which can damage the sample as well as the RTP sample holder. The number of steady steps depends on the target annealing temperature. One steady step is sufficient between 400^o C to 450^o C for one minute for the target annealing temperature of 700^o C, but two steady step is required for the target

annealing temperature of 1150^{o} C. Temperatures between 400^{o} C to 450^{o} C and 700^{o} C to 750^{o} C will be the best choices for one minute steady steps.

Figure 35: Rapid thermal annealing furnace at McMaster University

Figure 36: Sample chamber of the RTP of McMaster University.

A picture of the JetFirst rapid thermal furnace is shown in figure 35 and figure 36. It has also the controlling feature of temperature with thermocouple and pyrometer. This furnace is also capable of vacuum as well as atmospheric process. It is controlled by a PC and it has one purge gas line with a maximum of three process gas lines controlled with a mass flow controller (MFC). Thermal annealing as high as 1300^{o} C can be done by this furnace with the rise rate of 1^{o} C/s to 300^{o}C/s [40]. The wafer is heated via infra-red/visible radiation [2] [38]. First heating and cooling rates are correctly maintained by halogen lamps (Figure 34) which raise the temperature [38].

In a rapid thermal annealing process, several steps are defined i.e. delay step, ramp step and steady step (Figure 37). Normally every annealing recipe has two delay steps, one is at the starting point and other one is at the ending point. Throughout the first delay step the bulbs are off but the N_2 gas is flowing for the cleaning purposes. In the second delay step the gas flow helps the wafer to cool down. The duration of this step is about five to ten minutes.

Ramp steps drive the temperature up or down from a steady stage. The duration of this step depends on the temperature rise rate.

The wafer experiences a constant temperature during the steady step. This step duration is normally about one minute. A complete representation of a recipe including delay, ramp and steady steps is shown in figure 37- screen grab from the McMaster RTP.

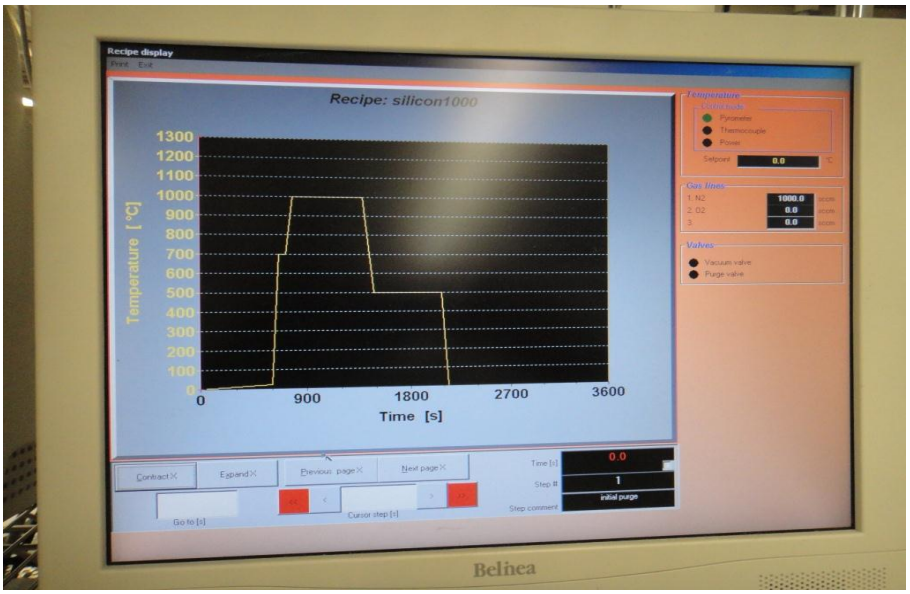

Figure 37: A complete diagram of steps during annealing.

3.5 Photoluminescence (PL) Set Up

The PL set-up is used to measure luminescence intensity from a sample when it is excited with a light source such as a laser [42-43] [50-51]. The principal of operation of the PL set-up is shown in figure 38 and figure 39.

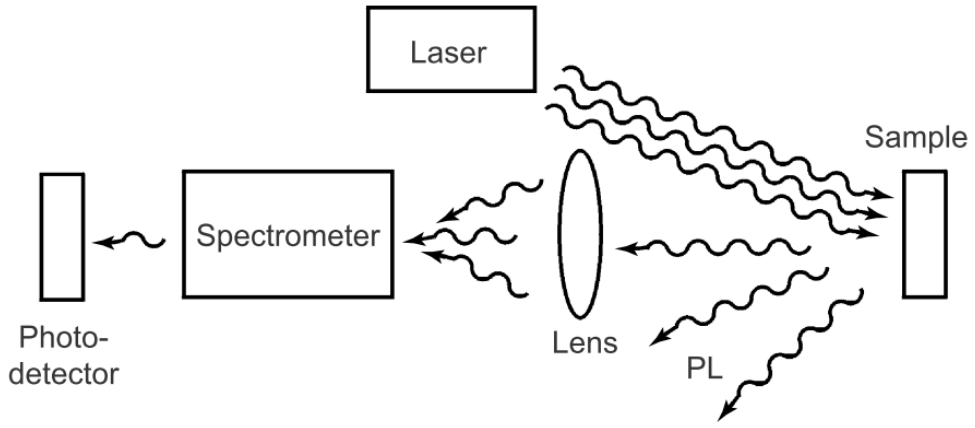

Figure 38: Basic PL set up including laser, spectrometer, lenses, sample and photo-detector [50].

When laser output hits a sample with sufficient energy, the electrical excitations are formed and subsequently relax via photon emission [42] [50-51]. Lenses are used to collect the desired output PL component coming from the sample after the laser hits it. The spectrometer distinguishes the light intensity as a function of wavelength. Then the optical system collects the photons by the photo-detector. Software is used to get the PL intensity graph.

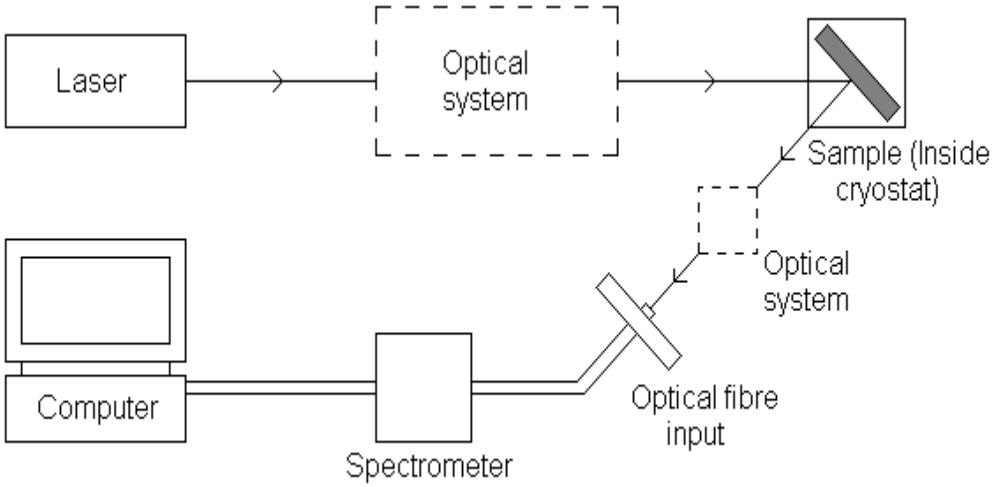

Figure 39: Schematic diagram of PL set up [51].

Spectrasuite software is used to control the PL set-up used in this research. Ocean optics USB4000 detector and yellow filter are used to detect the luminescence. The voltage applied to the laser is .62V and laser type is 405 nm 50mW solid state. The McMaster PL set up is shown at figure 40.

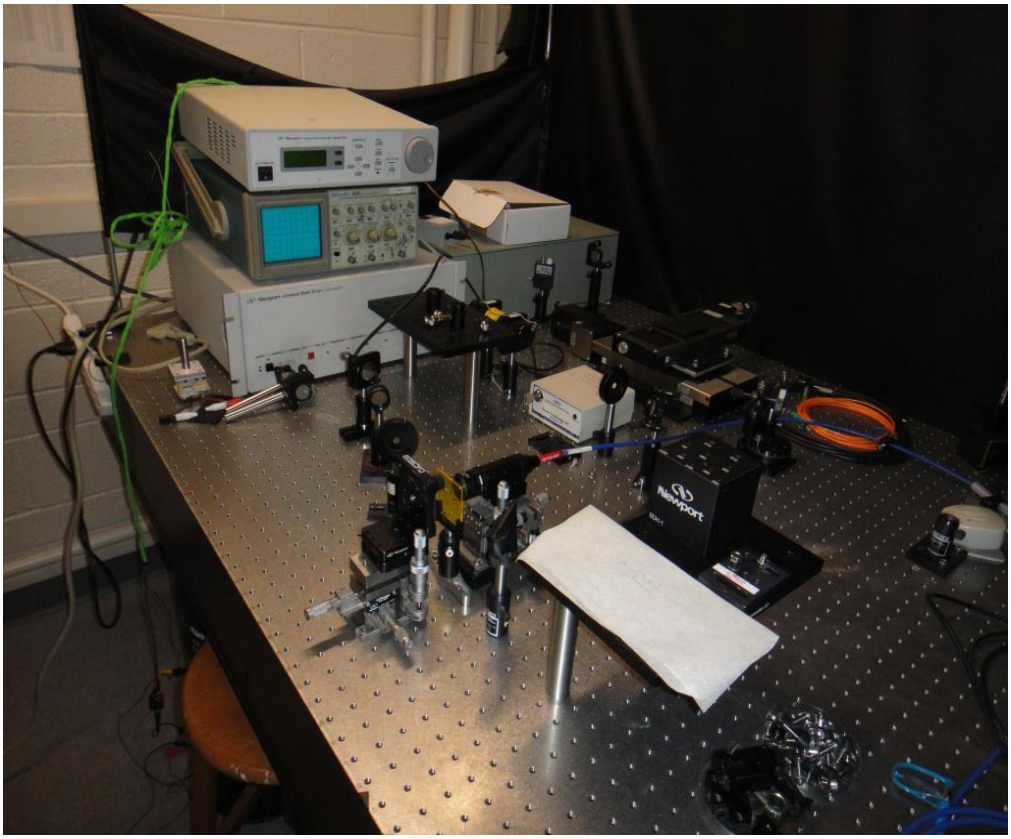

Figure 40: PL set up at McMaster University for this work.

3.6 Conclusion

The ion implanter, rapid thermal annealer and PL set up used in this research have been described. The ion implanter is used to introduce Si ions into a SiO_2 samples according to the requirement of the researcher and rapid thermal annealer removes the defect caused the ion implanter and helps to grow nanocrystals. The described PL set up measures the luminescence coming from the sample and gives the resulting PL intensity with respect to the emission wavelength.

CHAPTER FOUR: RESULTS AND DISCUSSION

4.1 Introduction

This chapter presents the core of this thesis work. All data and results are discussed along with presentation of results via tables and figures. The summary of the research work as well as the contributions to the field is presented. Two areas of study were performed during the research i.e. the effect of oxide layer thickness on the formation of nanocrystals and the effect of measurement temperature on the luminescence of samples. Figure 41 reveals the flow chart of this work.

4.2 Flow Chart

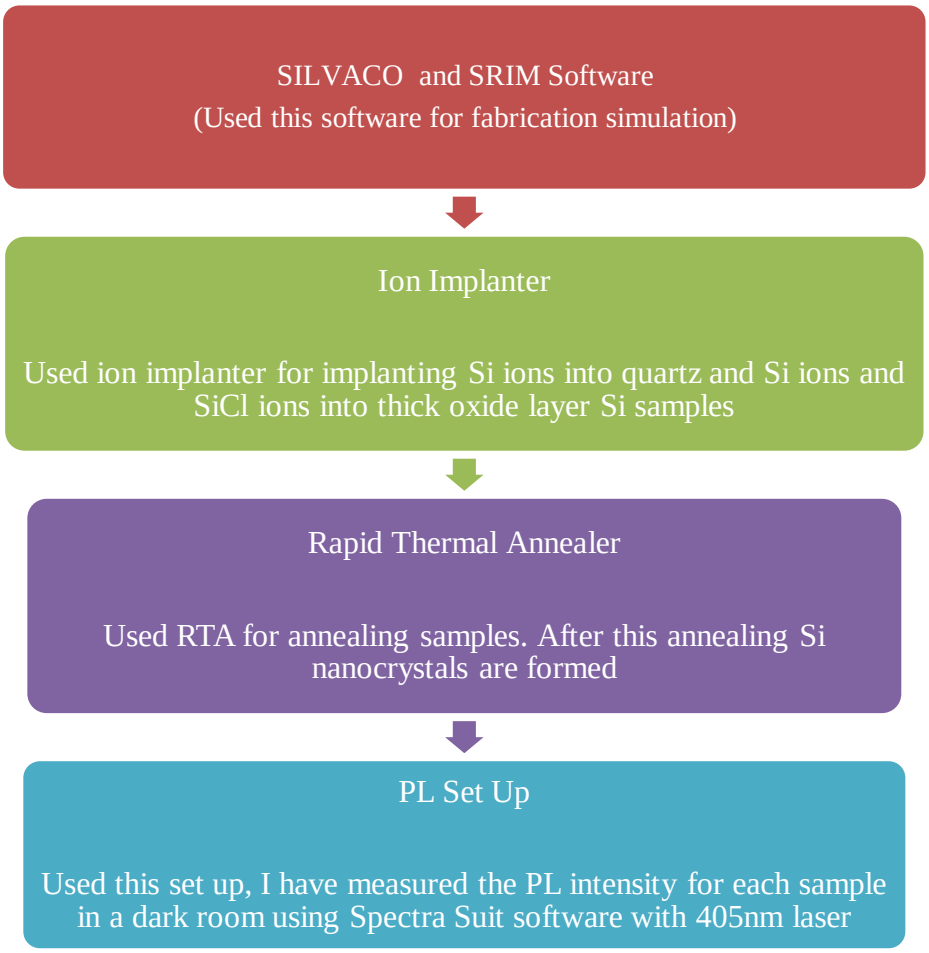

Figure 41: Flow chart of work.

4.3 Initial Fabrication of Si Nanocrystals

4.3.1 Flow of work

Several preliminary samples were prepared to investigate a potential process for nanocrystal formation. The work flow, together with specific sample description, is

described in figure 42. The 1mm quartz sample is named as sample-1, a thermal oxide layer grown on silicon describes samples-2 to 4. For sample 1, the implantation doses were 1.5×10^{16} ions_cm^{-2}, 3.0×10^{16} ions_cm^{-2}, 4.5×10^{16} ions_cm^{-2}, 6.0×10^{16} ions_cm^{-2}, or 7.5×10^{16} ions_cm^{-2} and implantation energy was same for each implantation doses which was 25 KeV. The implant ion was Si for sample 1.

The dose and implantation energy were 2.0×10^{16} ions_cm^{-2} and 23 KeV respectively for sample-2. The implant ion was SiCl for this sample.

The dose and implantation energy were 2.0×10^{16} ions_cm^{-2} and 30 KeV respectively for sample-3. The implant ion was Si for this sample.

For sample-4, those values were 3.0×10^{16} ions_cm^{-2} and 25 KeV. Implanted ion was Si for the sample.

			Anneal				Passivation				PL		
Substrate	**Doses**	**Energy**	**Temperature**	**Gas**		**Time**	**Gas**		**Temperature**	**Time**	**Intensity**	**Integration time**	**Range**
	Si+ /cm^2	**KeV**	**°C**	**Type**	**SSCM**	**mins**	**Type**	**SSCM**	**°C**	**mins**	**Counts**	**msec**	**Nm**
Sample-1 (1 mm thick quartz)	1.5 x 10^16	25	1050	N_2	1000	10	N_2H_2	1000	500	10	0	100	n/a
	3.0 x 10^16	25	1050	N_2	1000	10	N_2H_2	1000	500	10	0	100	n/a
	4.5 x 10^16	25	1050	N_2	1000	10	N_2H_2	1000	500	10	0	100	n/a
	6.0 x 10^16	25	1050	N_2	1000	10	N_2H_2	1000	500	10	0	100	n/a
	7.5 x 10^16	25	1050	N_2	1000	10	N_2H_2	1000	500	10	0	100	n/a

Table 2: Experimental data for 1 mm quartz sample (sample-1).

			Anneal				Passivation				PL		
Substrate	**Doses**	**Energy**	**Temperature**	**Gas**		**Time**	**Gas**		**Temperature**	**Time**	**Intensity**	**Integration time**	**Range**
	SiCl+ for sample-2 & Si+ for sample-3 /cm^2	**KeV**	**°C**	**Type**	**SSCM**	**mins**	**Type**	**SSCM**	**°C**	**mins**	**Counts**	**msec**	**Nm**
Sample-2	2.0 x 10^16	23	950	N_2	1000	10	N_2H_2	1000	500	10	0	100	n/a
	2.0 x 10^16	23	1000	N_2	1000	10	N_2H_2	1000	500	10	0	100	n/a
	2.0 x 10^16	23	1050	N_2	1000	10	N_2H_2	1000	500	10	0	100	n/a
	2.0 x 10^16	23	1100	N_2	1000	10	N_2H_2	1000	500	10	0	100	n/a
	2.0 x 10^16	23	1150	N_2	1000	10	N_2H_2	1000	500	10	1000	100	700-800
Sample-3	2.0 x 10^16	30	950	N_2	1000	10	N_2H_2	1000	500	10	0	100	n/a
	2.0 x 10^16	30	1000	N_2	1000	10	N_2H_2	1000	500	10	0	100	n/a
	2.0 x 10^16	30	1050	N_2	1000	10	N_2H_2	1000	500	10	0	100	n/a
	2.0 x 10^16	30	1100	N_2	1000	10	N_2H_2	1000	500	10	0	100	n/a
	2.0 x 10^16	30	1150	N_2	1000	10	N_2H_2	1000	500	10	2500	100	800-900

Table 3: Experimental data for 2.0×10^{16} ions_cm^{-2} dose samples for SiCl+ fluence with 23 KeV implantation energy (sample-2) and Si+ fluence with 30 KeV implantation energy (sample-3).

			Anneal				Passivation				PL		
Substrate	**Dose**	**Energy**	**Temperature**	**Gas**		**Time**	**Gas**		**Temperature**	**Time**	**Intensity**	**Integration time**	**Range**
	Si+ /cm^2	**KeV**	**°C**	**Type**	**SSCM**	**mins**	**Type**	**SSCM**	**°C**	**mins**	**Counts**	**Msec**	**nm**
Sample-4	3.0 x 10^16	25	950	N_2	1000	10	N_2H_2	1000	500	10	0	100	n/a
	3.0 x 10^16	25	1000	N_2	1000	10	N_2H_2	1000	500	10	0	100	n/a
	3.0 x 10^16	25	1050	N_2	1000	10	N_2H_2	1000	500	10	11000	100	660-960
	3.0 x 10^16	25	1100	N_2	1000	10	N_2H_2	1000	500	10	12000	100	650-950
	3.0 x 10^16	25	1150	N_2	1000	10	N_2H_2	1000	500	10	10000	100	650-950

Table 4: Experimental data for 3.0×10^{16}ions_cm^{-2} dose with Si+ fluence and 25 KeV implantation energy sample (sample- 4).

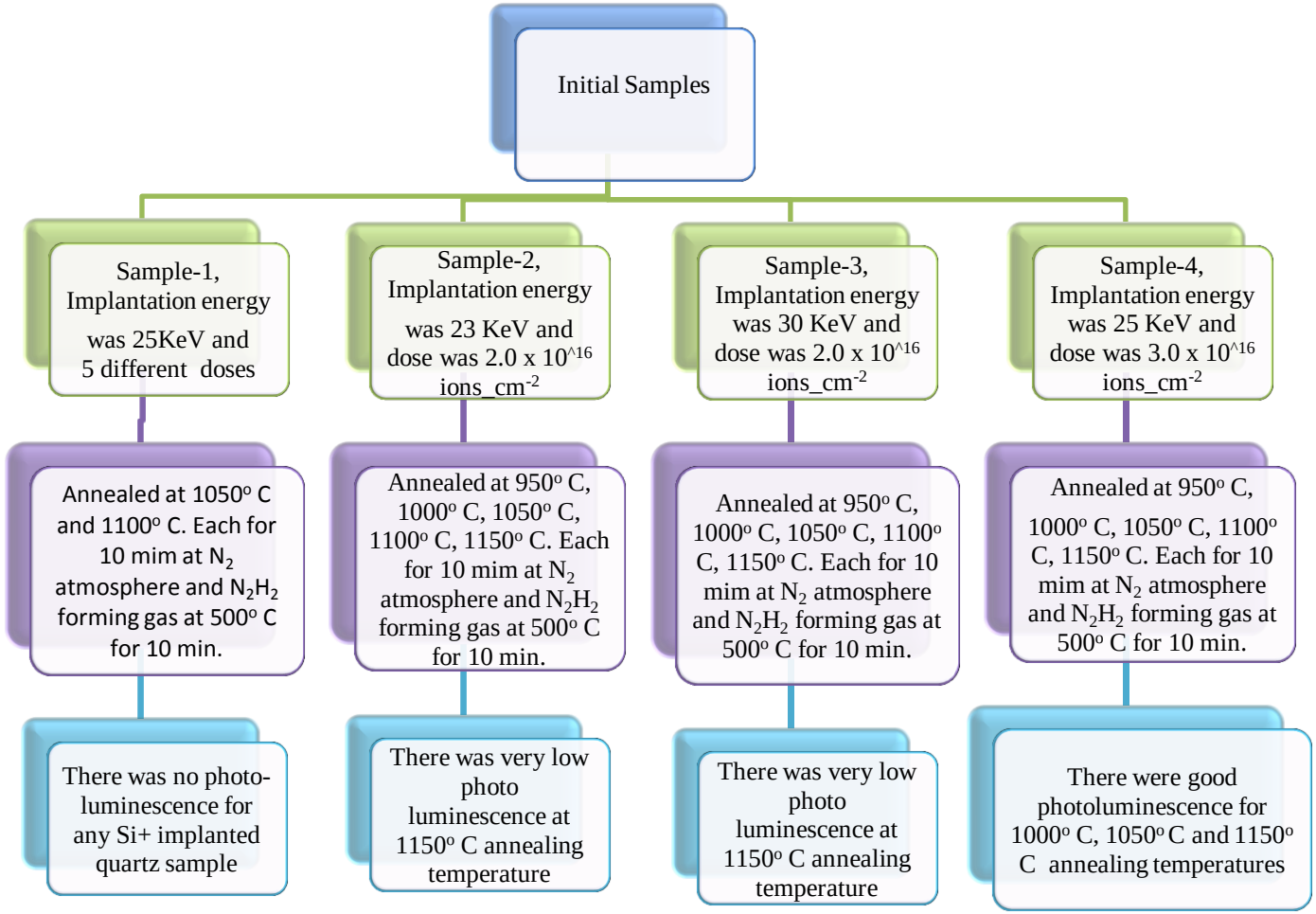

Figure 42: Flow diagram describing the preparation of initial Si-nanocrystal samples.

4.3.2 Results and Discussion

Annealing the Si^+ implanted quartz samples at 1050^o C and 1100^o C did not show any photoluminescence. This happened because no Si nanocrystal was formed according to this work. Changing implantation doses had no effect. So for quartz, no PL was found. So the high temperature rapid thermal annealing and H_2 passivation cannot make Si nanocrystals at quartz. For fabricating Si nanocrystals, SiO_2 layer on top of Si wafer is essential because only implanted Si ions within the oxide layer form nanocrystals [1] [48]. Decomposition, segregation, diffusion, nucleation, aggregation, growth and crystallization process steps have to be accomplished to fabricate nanocrystals. So according to this work it can be said that all of those steps were not performed in quartz.

For both sample-2 and sample-3, no PL was found before annealing at a temperature of 1150^o C. According to this work, before this temperature Si nanocrystals were not formed for these samples. For forming Si nanocrystals decomposition, segregation, diffusion, nucleation, aggregation, growth and crystallization process have to take place. It is known that furnace annealing at a temperature of more than 1000^o C can induce all the above steps [1]. But here no furnace annealer is used, only a rapid thermal annealer. Normally the duration of furnace annealing is about several hours but for rapid thermal annealing the duration are few minutes [1] [11] [26].

Significant photoluminescence was observed for higher annealing temperatures for the thick oxide layer on Si wafer sample implanted with a dose of 3.0×10^{16} ions_cm^{-2}

and energy of 25 KeV (Sample-4). This relatively large PL signal compared to samples 2 and 3 is likely due to the larger implantation dose. Iwayama *et al* also observed the same behavior [1]. Another observation is the PL intensity increases with the increase of annealing temperature. The Si nanocrystals start to emit relatively large amounts of light from 1050^{o} C annealing temperature for sample 4.

From the tables 2 to 4 of this chapter and the figure 9 and figure 13 of chapter 2, it is found that the relationship for rapid thermal annealing (RTA) is quite similar with furnace annealing (FA), although the temperature at which nanocrystals begin to form is different from that observed after furnace annealing [1] [11]. From the data, an interesting feature is observed. The PL intensity increases with the initial increase of annealing temperature but appears to saturate as the temperature is increased beyond 1100^{o}C (Figure 43). It is noted though that this trend is deduced from only three data points. The same results were found by Sais *et al* for three different annealing temperatures [26].

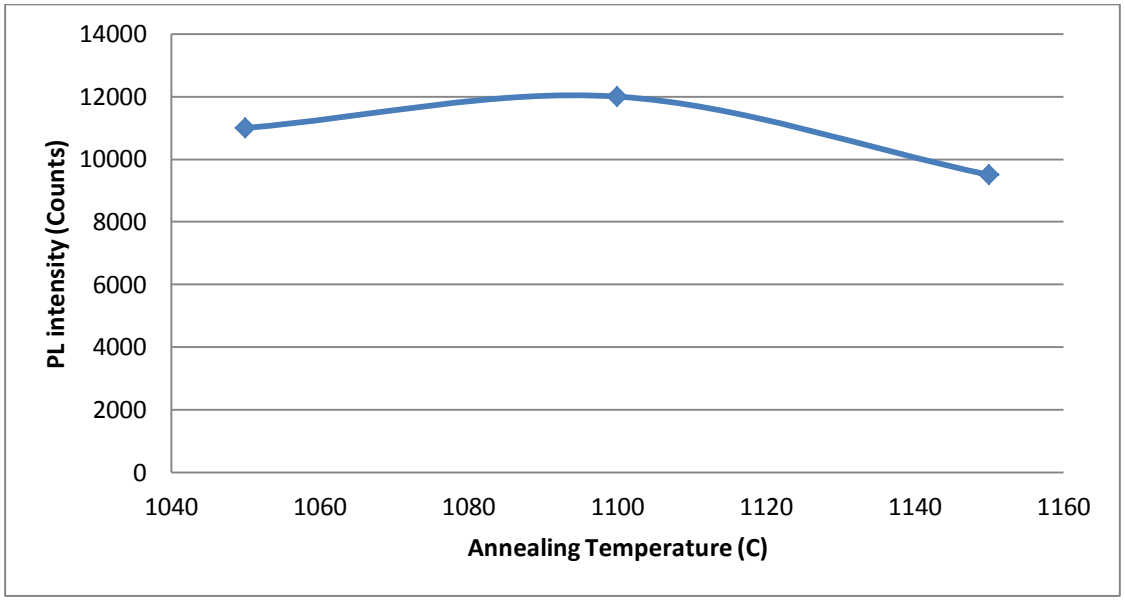

Figure 43: PL intensity as a function of higher annealing temperature for sample-4.

This trend may be explained by consideration of the nanocrystal size. With the increase of annealing temperature the diameter of Si-nanocrystals increases. The PL intensity will initially increase with the increase as more nanocrystals nucleate and begin to grow. At some point the Si-nanocrystals begin to take on bulk-like properties, either as individual nanocrystals become too large to induce quantum confinement or as two nanocrystals overlap. The PL thus begins to decrease toward that which might be expected for bulk silicon samples.

During the preliminary stage of research it was tried to make Si nanocrystals from Si^+ implanted quartz and Si^+ and $SiCl^+$ implanted thick oxide layer Si wafers followed by rapid thermal annealing (RTA). There was no emission from silicon nanocrystals in

quartz. But for the other Si^+ implanted thick oxide layers PL was observed. The PL intensity was directly related to the annealing temperature and implantation ion dose. The PL increases with the annealing temperature up to a limiting value. It is also found that the formation behavior of Si nanocrystals is similar for both furnaces annealing (FA) followed by rapid thermal annealing (RTA) and rapid thermal annealing (RTA) only [1] [11]. The Si nanocrystal formation temperature for only FA is about 1000^o C and for only RTA is about 1050^o C. But 1100^o C rapid thermal annealing gives the best result in terms of PL intensity. So this annealing temperature was used for all the subsequent samples.

4.4 Calibration of Rapid Thermal Annealer (RTA)

Rapid thermal annealing (RTA) was used for annealing the samples after the ion implantation thus removing the defects caused during ion implantation. The RTA is also used for passivation via the flow of forming gas (N_2H_2) and also for growing thermal SiO_2 layer (dry oxidation) on Si samples. At the beginning of the project, the RTA was calibrated using the Deal and Grove model for thermal oxidation. The model describes the relationship of the annealing time, annealing temperature and oxide thickness [45]. Bruce Deal and Andrew Grove formulated the model in 1965 for calculating the thickness of a thermal oxide layer [46]. It has been widely used and tested ever since. It is appropriate for oxide growth on plane substrate (one-dimensional). For this research, these limitations do not have any impact. So this model was suitable for calibrating RTA for this research work.

4.4.1 Deal Grove Model

The thermal oxidation of silicon process has three stages i.e. i) oxidizing gas comes to the outer surface of oxide, ii) diffuses through any present oxide layer to the oxide substrate interface and iii) reaction with the substrate (Figure 44) [47].

At the first stage, the flux is described by

$$F_1 = h\,(C^* - C_O) \quad \text{---------- (i)}$$

Where, h is gas-phase transport coefficient, C^* is the equilibrium concentration of the oxidants in the surrounding gas atmosphere, C_O is the concentration of oxidants at the oxide surface at any given time.

At second stage the flux is described by

$$F_2 = D\frac{\partial C}{\partial x} = D\frac{C_O - C_S}{x_o} \quad \text{---------- (ii)}$$

Where, D is the oxidant diffusivity in the oxide, C_S is the oxidant concentration at the oxide on silicon interface and x_O is the oxide thickness.

The flux of third stage is described by

$$F_3 = K_S C_S \quad \text{---------- (iii)}$$

Where, K_S is the surface constant and depends on the number of processes occurring at the oxide layer and material interface.

According to Deal and Grove $F_1 = F_2$ and $F_2 = F_3$

$$\text{So, } F_1 = F_2 = F_3 = F = {C^*}\Big/{\left(\frac{1}{k_s} + \frac{1}{h} + \frac{x_o}{D_0}\right)} \quad \text{---------- (iv)}$$

Flux of oxidant molecule is proportional with the oxide growth rate

$$F/_N = dx_0/_{dt} \text{ ---------- (v)}$$

Where, N is the per unit volume oxidant molecule number.

From equation (iv) and equation (v)

$$dx_0/_{dt} = C^*/_{(\frac{1}{k_s} + \frac{1}{h} + \frac{x_o}{D_0})} \text{ ---------- (vi)}$$

The simplified equation is

$$dx_0/_{dt} = B/_{(A + 2x_0)} \text{ ---------- (vii)}$$

Where, B= $2DC^*/_N$; A= 2d($1/_{K_S}$ + $1/_h$)

An integration of the equation (vii) is performed from t=0 to t=t

$$x_0^2 + Ax_0 = B(t + \tau) \text{ ---------- (viii)}$$

Where, $\tau = (x_i^2 + Ax_i)/_B$ and x_i is the initial oxide thickness at t=0.

After solving the equation,

$$\text{time, t} = \frac{x_o^2 - x_i^2}{B} + \frac{x_o - x_i}{B/_A} \text{ ---------- (ix)}$$

Where, B is a parabolic rate constant and B/A is a linear rate constant.

The relationship between time and oxide thickness is defined by equation (ix) (Figure 54).

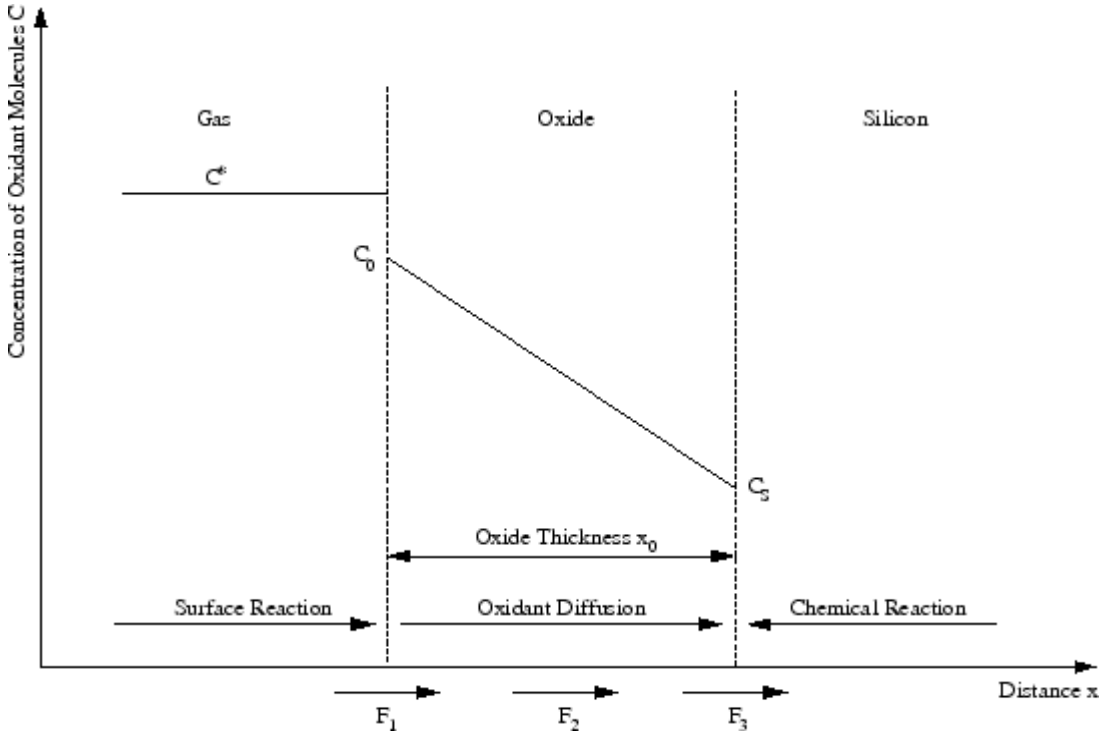

Figure 44: Oxidation process on silicon wafer [47].

From equation (viii)

$$x_o = \frac{-A+\sqrt{A^2+(B)(t+\tau)}}{2} \text{ --------- (x)}$$

Two general regimes exist for oxidation:

1) Long oxidation times when t >> τ and t >> $\frac{A^2}{4B}$; $x_{O\cong\sqrt{B.t}}$

This condition is known as parabolic condition.

2) Short oxidation times when t ≪ $\frac{A^2}{4B}$; $x_{O\cong}\frac{B}{A}$ (t+ τ)

This condition is known as linear condition.

4.4.1.1 Effect of Temperature

Deal grove parameters are described by

$B = C_1 e^{-E_1/KT}$ and $\frac{B}{A} = C_2 e^{-E_2/KT}$

Where, C_1 and C_2 are pre-exponential constants, E_1 and E_2 are activation energies (Figure 45). Significant observations are E_1, E_2 and C_1 are same for any orientation of Si, only C_2 changes with the orientation of Si and E_1 varies for dry O_2 and wet H_2O because of the diffusion coefficients of O_2 and H_2O in SiO_2 [47] [57].

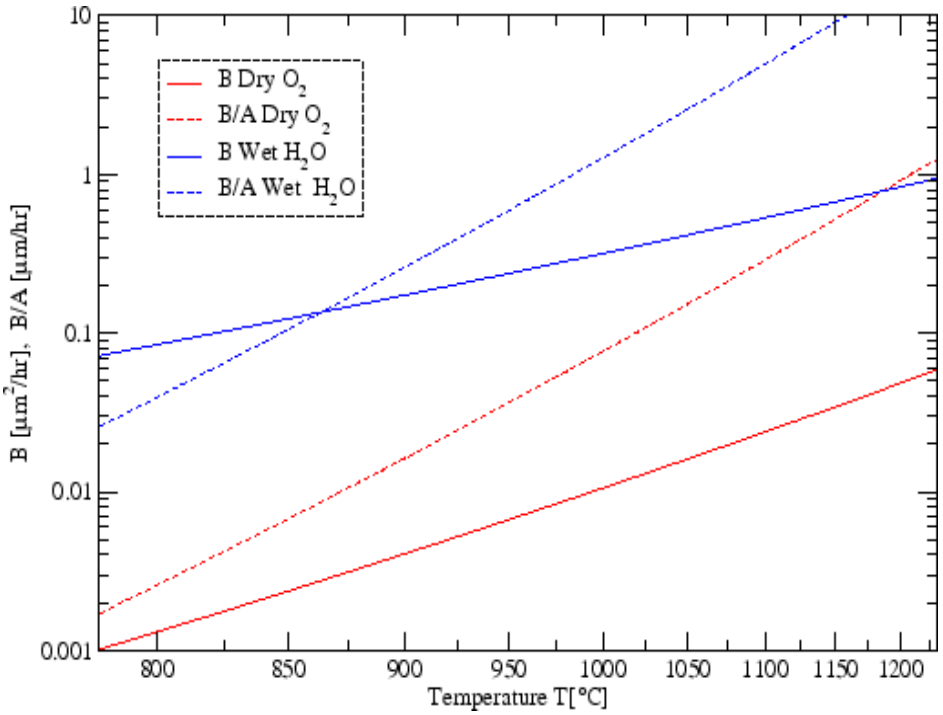

Figure 45: B and B/A versus temperature for (111) oriented silicon for wet and dry oxidation [47].

4.4.2 Procedure and Results

Thermal oxide layers were grown on silicon substrates at a variety of temperatures and then measured using an ellipsometer. The measured results were compared with results obtained from the Deal-Grove model (Table 5) [44]. The difference in measured and modeled thickness was used to deduce a calibration offset for the RTA system. The relationship between the set and actual temperatures of RTA are plotted at figure 46 and figure 47.

Set Temperature (C)	Theoretical Thickness (A)	Actual Temperature (C)	Measured Thickness (A)
830	38	910	78.49
900	71	954	131.36
950	125	997	217.66
1000	225	1036	334.05
1050	385	1092	563.12

Table 5: Set temperatures at RTA along with the actual temperatures from Deal Grove model and their corresponding oxide thickness are shown. Initial oxide thickness was 25.28 A.

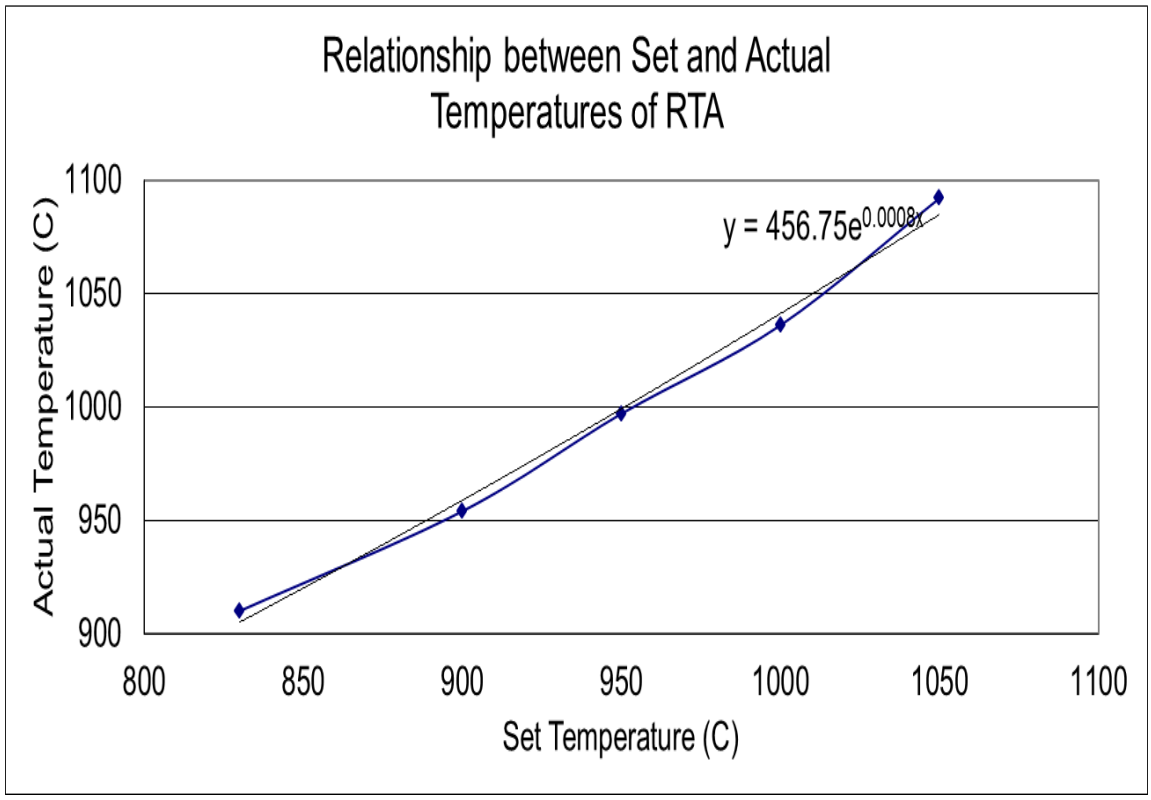

Figure 46: Set temperatures vs. Actual temperatures graph for RTA.

The theoretical thicknesses were the predicted oxide thicknesses according to Deal Grove model due to the nominal, set temperatures of the RTA. The measured thicknesses were the corresponding oxide thicknesses measured by ellipsometer. The actual temperatures were deduced from Deal Grove model from the corresponding measured thicknesses. The relationship between two set temperatures corresponding to number of data is revealed in figure 47.

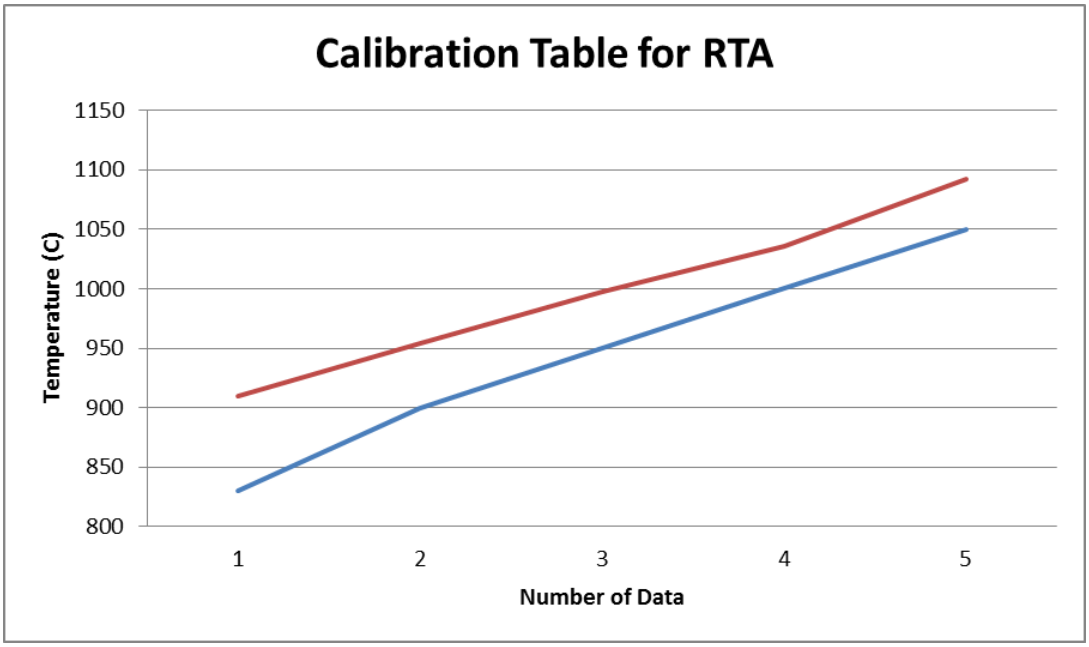

Figure 47: Number of data vs. Set temperature and Actual temperature graph for RTA. Blue line represents a line touching all set temperatures data points and red lines represents that for actual temperatures.

4.5 Calculation of Required Implantation Conditions

During the research work, 90% of implanted Si ions were aimed to be implanted in the thin films of SiO_2 with the intention for fabricating adequate number of Si nanocrystals. Only the implanted Si ions in the SiO_2 layer are going to form Si nanocrystals. The Stopping and Range of Ions in Matter (SRIM) is commonly used software to measure several properties such as stopping range of implanted ions, damages of the targets for corresponding implantation energies for specific implanted ions with various implantation angles [49]. SRIM is used to model the specific SiO_2 layer thickness for a given implantation energy which meets this criterion. The

implanted ions had a distribution profile which was similar to a Gaussian curve (Figure 48).

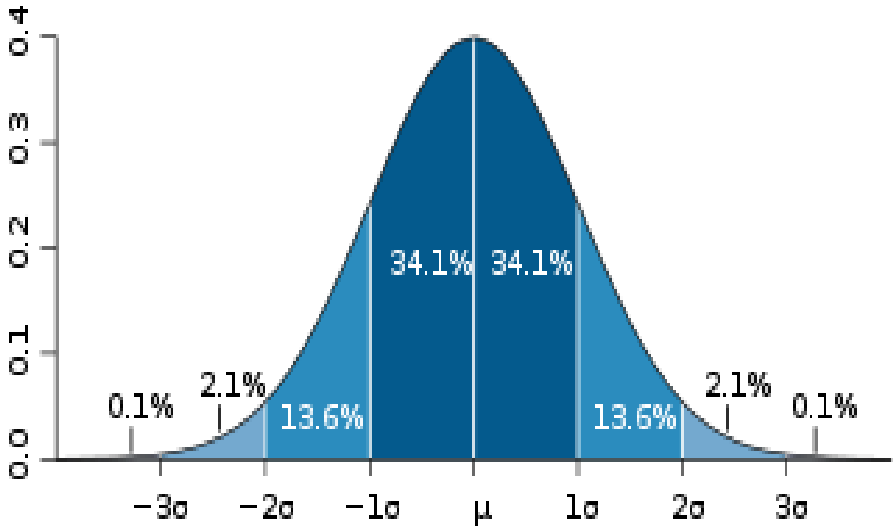

Figure 48: Gaussian Curve. The number indicates the first standard deviation (68.2% of all data), second standared daviation (95.6% of all data) and third standared daviation (99.8% of all data) from the mean value.

The SRIM simulation for implanted Si ion distribution in SiO_2 layers for implantation energies of 10 KeV, 20 KeV and 30 KeV are shown in figure 49, figure 50 and figure 51 respectively.

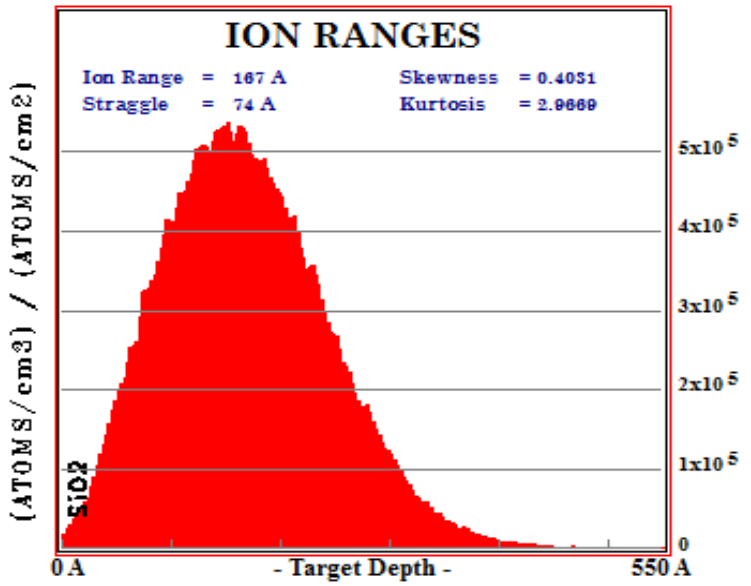

Figure 49: SRIM simulation for implanted Si ion distribution in SiO_2 layers for implantation energy of 10 KeV.

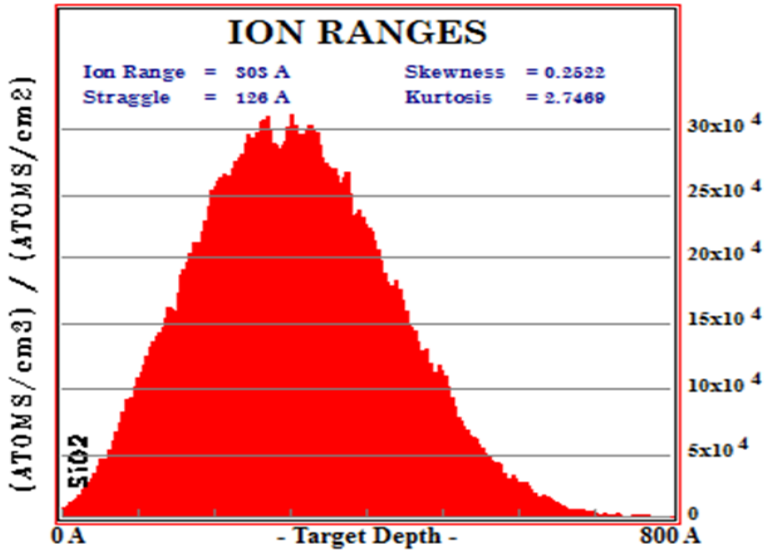

Figure 50: SRIM simulation for implanted Si ion distribution in SiO_2 layers for implantation energy of 20 KeV.

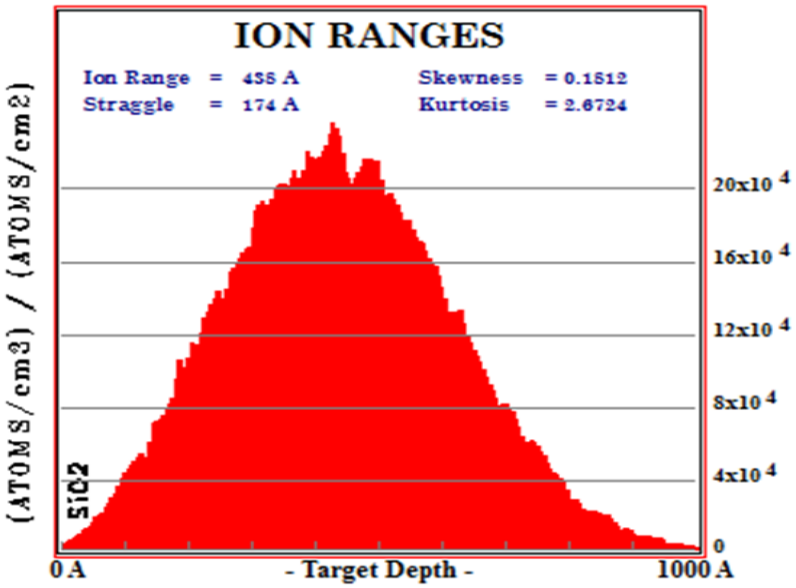

Figure 51: SRIM simulation for implanted Si ion distribution in SiO_2 layers for implantation energy of 30 KeV.

The oxide thickness values required for 90% of implanted Si within the SiO_2 layer for different implantation energies are given at table 6.

Implantation Energy (KeV)	Oxide Thickness (A)
10	290
15	385
20	520
25	610
30	720
35	800
40	890

Table 6: The oxide thickness required for 90% of the silicon ions to stop in a SiO_2 layer for 10-40 KeV implantation energies.

The samples with specific thickness were made using the RTA. All the data and results are given in table 7.

Temperature	Time (min)	Calculated Thickness (A)	SRIM O/P Thickness (A)	Measured Thickness (A)
1023	30	291	290	330
1050	30	385	385	430
1099	25	521	520	600
1108	28	611	610	624
1123	30	720	720	693
1138	30	801	800	799
1156	30	902	895	948

Table 7: Calculated (for RTA), SRIM simulated and ellipsometer measured thickness of oxide layers.

4.6 Effect of Annealing Temperatures

Three sets of samples were initially fabricated to investigate the effects of annealing temperatures on PL emission from Si-nanocrystals. The implantation energies and implantation doses were 25 KeV, 20 KeV, 10 KeV and 3.0 $\times 10^{16}$ ions_cm^{-2}, 2.3 $\times 10^{16}$ ions_cm^{-2} and 1.5 $\times 10^{16}$ ions_cm^{-2} respectively. The oxide thicknesses were 624 A, 620 A and 330 A respectively.

Enhancing the PL from Si nanocrystals is a challenging job. One approach is the increase of implantation doses i.e. implanted Si+ ions which increase the concentration of excess Si [65]. But the solution is not so simple. PL intensity is directly related with the Si nano-inclusion areal density. Nano-inclusion is inclusion at nanoscale. So the nanocrystals are one kind of nano-inclusion. But Si nano-inclusion sizes must be suitable for quantum confinement. The increase of implantation doses increases the PL intensity along with the size of Si nano-inclusions. So for high implantation doses the size of Si nano-inclusions is too high for the quantum confinement. And therefore PL intensity decreases at sufficiently higher doses [65].

The same result was found by two groups i.e. the PL intensity went through a maximum value then dropped with the increase of doses for fixed annealing temperature [59-60] [65]. The explanation was at high dose the nanocrystals as well as inclusion concentration was high. The mechanical overlapping of inclusions occur which is responsible for PL intensity decreases due to the less oscillator strength i.e. radiative transition [59].

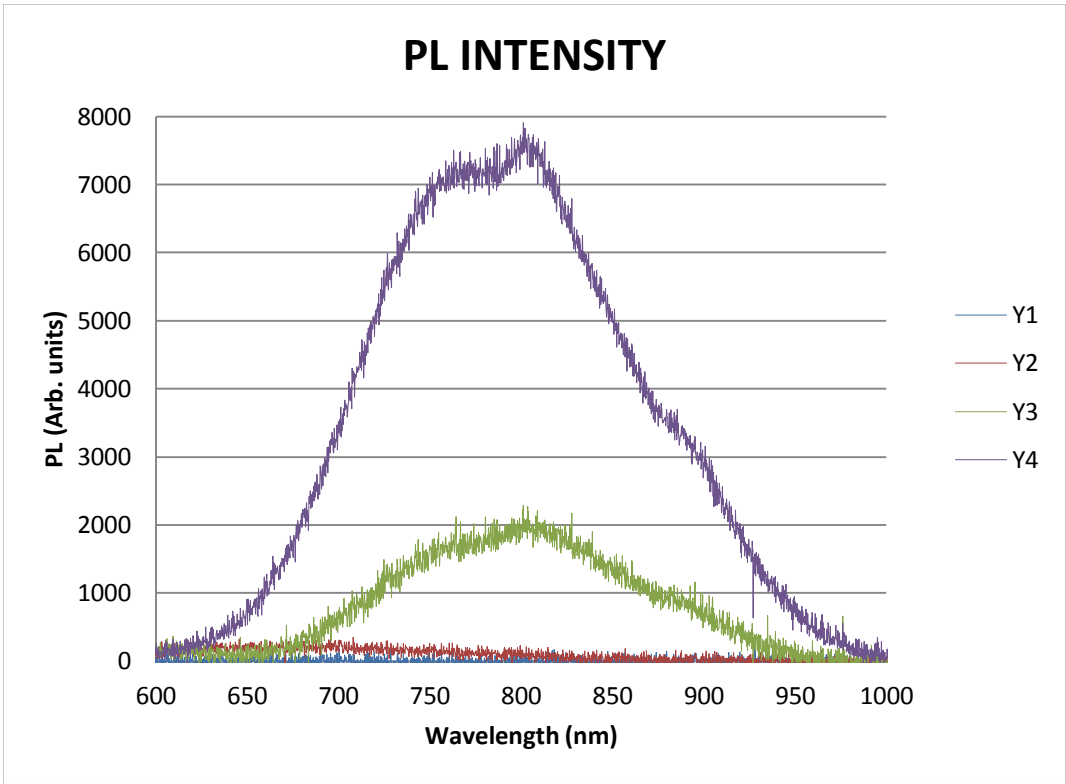

Figure 52: Wavelength vs PL intensity graph for two different annealing temperatures i.e. 1000^{o} C and 1100^{o} C for 30 minutes each case. Parameters for Y1, Y2,Y3 and Y4 are 10KeV, 1000^{o}C; 20KeV, 1000^{o}C; 10KeV, 1100^{o}C and 20KeV, 1100^{o}C respectively while the other parameters are same. For 10 KeV and 20 KeV the doses are 1.5×10^{16} ions_cm^{-2} and 2.3×10^{16} ions_cm^{-2} respectively. Integration time was 6 seconds.

The PL intensities for 20 KeV and 10 KeV samples are shown in figure 52. The PL intensities due to different annealing temperature for three different samples are shown in table 8.

Implantation Energy (KeV)	Implantation Dose (ions_cm^{-2})	Annealing Temperature (^{o}C)	Peak PL Intensities (Arb. Units)
25	3.0 x 10^16	1040	11000
25	3.0 x 10^16	1100	12000
25	3.0 x 10^16	1160	9000
20	2.3 x 10^16	1100	7800
20	2.3 x 10^16	1000	500
10	1.5 x 10^16	1100	2000
10	1.5 x 10^16	1000	300

Table 8: Annealing temperature dependence of PL peaks is shown for three sets of data.

During high annealing temperature, the diffusion of Si increases which is responsible for merging of inclusions i.e. Ostwald ripening. Ostwald ripening occurs when more than one nanocrystal or nanocrystals and inclusions come closer than two diffusion length for a fixed annealing temperature and duration. Then the size of merging Si nanocrystals radius will be more than the critical radius [59]. The amalgamation of inclusion is dominant with respect to mechanical overlapping at high annealing temperature [59] [66].

4.7 Effect of Oxide Layer Thickness

One of the main goals of this thesis work was to find out the effect of oxide thickness on Si nanocrystal formation and PL emission. Two sets of sample were used to

this end. The oxide on top of Si samples was grown to varying thicknesses. Due to the consideration that 90% of implanted Si^+ ions should be in that thickness the minimum thickness for 10 KeV and 20 KeV implantation energies were 290 A and 510 A respectively. 20 KeV and 2.3×10^{16} ions_cm^{-2} were the implantation energy and dose for one set of samples of three different oxide thickness of 600 A, 1150 A and 3400 A. For other set, the parameter were 10 KeV, 1.5×10^{16} ions_cm^{-2}, 330 A, 550 A, 1150 A and 1800 A. All samples were annealed at 1100^o C for 30 minutes and the forming gas, N_2H_2 were used at 500^o C for 10 minutes. The integration time during measuring PL was 6 seconds.

Imp E (KeV)	**Thickness (A)**	**Annealing Temp (^{o} C)**	**Measuring Temp (^{o} C)**	**PL (Arb. Unit)**
10	330	1100	20	2000
10	550	1100	20	4600
10	1150	1100	20	15000
10	1800	1100	20	11700

Table 9: PL intensities peak along with the PL ranges were shown for different oxide thicknesses. The implantation energy and doses were 10 KeV and 1.5×10^{16} ions_cm^{-2} *respectively.*

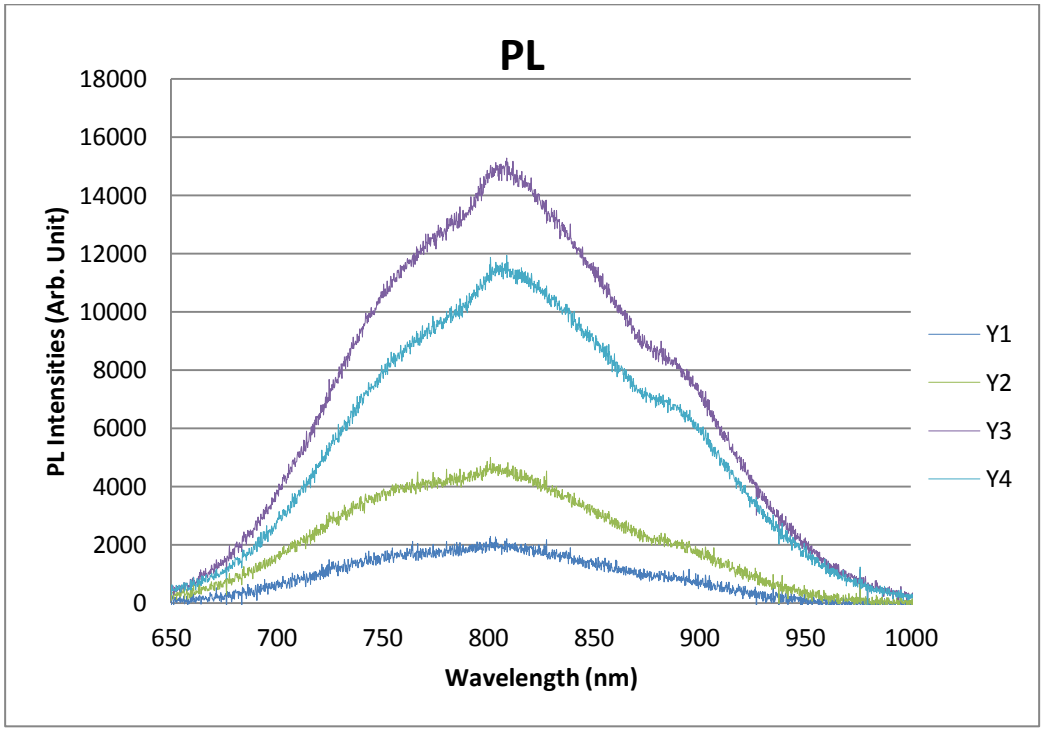

Figure 53: Wavelength vs PL intensity graph for 10 KeV implanted energy samples. Y1 indicates sample of 330A oxide layer. For Y2, Y3, and Y4, the oxide thicknes wass 550A, 1150A, and 1800A respectively. Measuring temperature was 20^{o}C.

Table 9 shows the relationship between the oxide thickness and PL intensities for 10 KeV implantation energy and 1.5×10^{16} ions_cm^{-2} dose samples. The PL intensities were 2000 Arb. unit, 15000 Arb. unit and 11700 Arb. unit at oxide thickness of 330 A, 1150 A and 1800A (Figure 53). So it was found that the PL intensity was increasing until 1150A oxide thickness and had maximum PL which was 15000 Arb. unit and after that the PL was decreasing with the increase with oxide thickness.

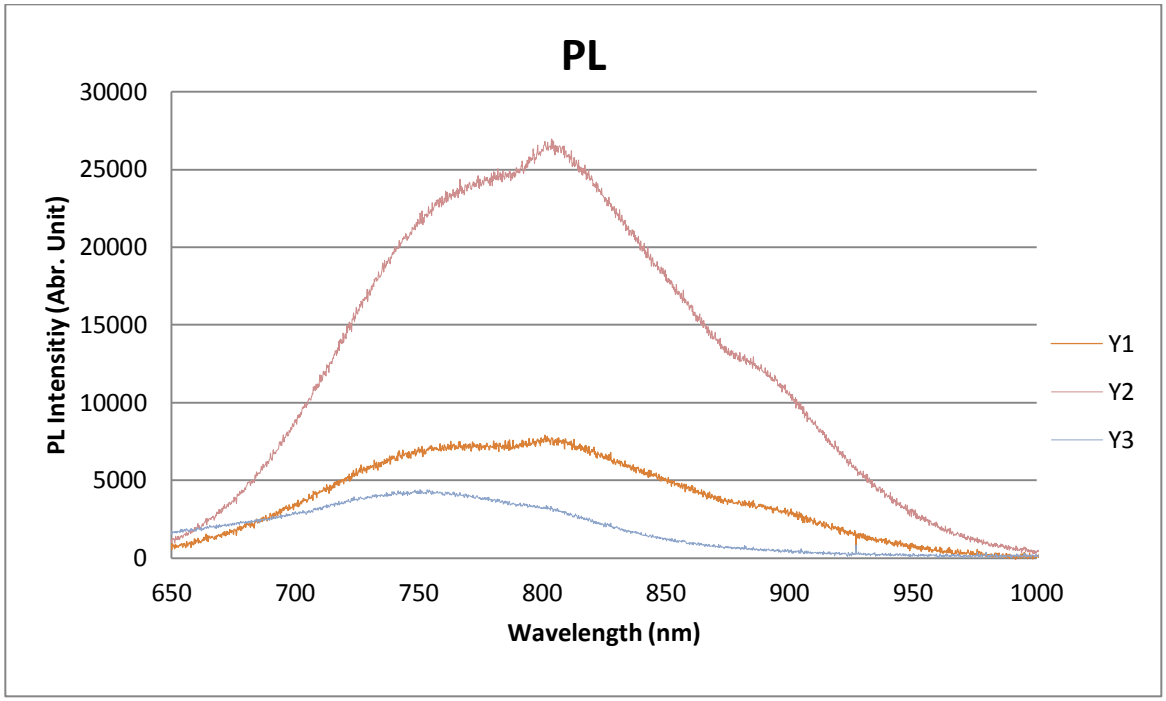

Figure 54: Wavelength vs PL intensity graph for 20 KeV implanted energy samples. Y1 indicates sample of 600A oxide layer. For Y2 and Y3, the oxide thickness was 1150A and 3400A respectively. Measuring temperature was 20^{o}C.

Imp E (KeV)	Thickness (A)	Annealing Temp (^{o} C)	Measuring Temp (^{o} C)	PL (Arb. Unit)
20	600	1100	20	7800
20	1150	1100	20	26500
20	3400	1100	20	4000

Table 10: PL intensities peak along with the PL ranges were shown for different oxide thickness. The implantation energy and doses were 20 KeV and 2.3×10^{16} ions_cm^{-2} *respectively.*

Table 10 shows the relationship between the oxide thickness and PL intensities for 20 KeV implantation energy and 2.3×10^{16} ions_cm^{-2} dose samples. The PL intensities

were 7800 Arb. unit, 26500 Arb. unit and 4000 Arb. unit at oxide thickness of 600 A, 1150 A and 3400 A (Figure 54). So it was found that the PL intensity was increasing until 1150A oxide thickness and had maximum PL which was 26500 Arb. Unit and after that the PL was decreasing with the increase with oxide thickness.

For both implantation energy 10 KeV with dose of 1.5×10^{16} ions_cm^{-2} and 20 KeV with 2.3×10^{16} ions_cm^{-2}, 1150A oxide thickness layer provides the maximum PL intensities. Optical interference is the cause for the results i.e. the effect of oxide thickness layer [74]. Optical interference is responsible for the modulation of PL spectrum [74]. Optical interference is the superposition of two or more light waves. Constructive interference, provides the maximum value and destructive interference, provides the minimum value of PL [75].

Shin *et al* studied the effect of dry oxidation thickness on porous Si [58]. The group found that the PL intensity changed with oxide thickness and it was not uniform. [58]. Barba *et. al.* group performed the study of oxide thickness on Si nanocrystals and found the same trend (increases to maximum value before starts decreasing) of results as this work [74].

4.8 Effect of Measuring Temperatures

The effect of measuring temperature (i.e. the temperature of the substrate during PL measurement as opposed to annealing temperature) is another focus of this thesis of this thesis work. Two sets of sample were used to do study on measuring temperature.

The parameters were 10 KeV, 1.5×10^{16} ions_cm^{-2}, 330 A, 550 A, 1150 A and 1800 A; 20 KeV, 2.3×10^{16} ions_cm^{-2}, 600 A and 1150 A. The annealing and forming gas flown time durations were 30 minutes at 1100^{o} C and 10 minutes at 500^{o} C respectively. Integration time during measuring PL was 6 seconds.

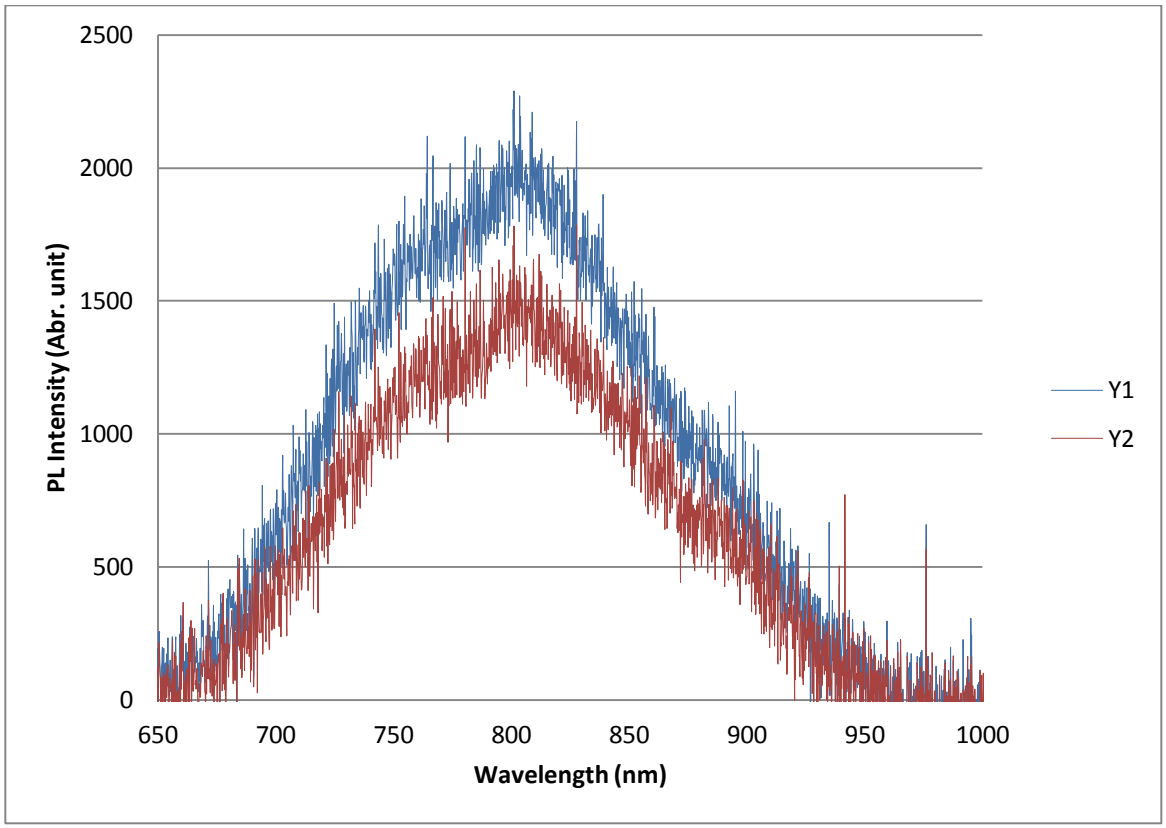

Figure 55: Wavelength vs PL intensity graph for 10 KeV implanted energy samples. Y1 and Y2 indicate samples PL intensities at measuring temperature of 20^{o} C and 60^{o} C respectively. The oxide layer of samples was 330A. Integration time during measuring PL was 6 seconds.

Imp E (KeV)	Thickness (A)	Annealing Temp (^{o} C)	Measuring Temp (^{o} C)	PL (Arb. Unit)	PL Range (nm)
10	330	1100	20	2000	650-950
10	330	1100	30	1900	650-950
10	330	1100	40	1800	650-950
10	330	1100	50	1700	650-950
10	330	1100	60	1600	650-950

Table 11: PL intensities peak along with the PL ranges were shown for different measuring temperature. The implantation energy, dose and oxide layer thickness were 10 KeV, 1.5×10^{16} ions_cm^{-2} and 330 A respectively.

The values of PL for 10 KeV implantation energy, 1.5×10^{16} ions_cm^{-2} dose and 330 A thickness samples due to different measurement temperatures are shown in table 11. The PL intensities were 2000 Arb. unit, 1800 Arb. unit and 1600 Arb. unit for the measuring temperatures of 20^o C, 40^o C and 60^o C (Figure 55).

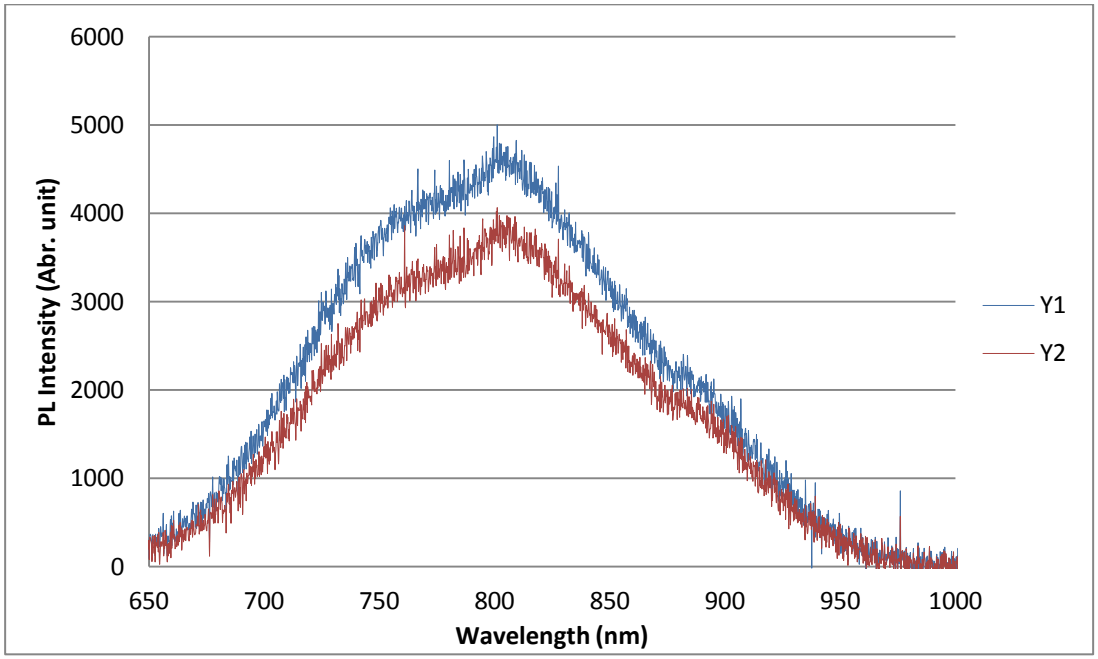

Figure 56: Wavelength vs PL intensity graph for 10 KeV implanted energy samples. Y1 and Y2 indicate samples PL intensities at measuring temperature of 20^{o} C and 60^{o} C respectively. The oxide layer of samples was 550A. Integration time during measuring PL was 6 seconds.

Imp E (KeV)	Thickness (A)	Annealing Temp (^{o} C)	Measuring Temp (^{o} C)	PL (Arb. Unit)	PL Range (nm)
10	550	1100	20	4600	650-950
10	550	1100	30	4400	650-950
10	550	1100	40	4200	650-950
10	550	1100	50	4000	650-950
10	550	1100	60	3800	650-950

Table 12: PL intensities peak along with the PL ranges were shown for different measuring temperature. The implantation energy, dose and oxide layer thickness were 10 KeV, 1.5×10^{16} ions_cm^{-2} and 550 A respectively.

The values of PL as a result of different measuring temperatures for 550 A thickness samples were revealed in table 12. The PL intensities were 4600 Arb. unit, 4200 Arb. unit and 3800 Arb. unit for the measuring temperatures of 20^{o} C, 40^{o} C and 60^{o} C (Figure 56).

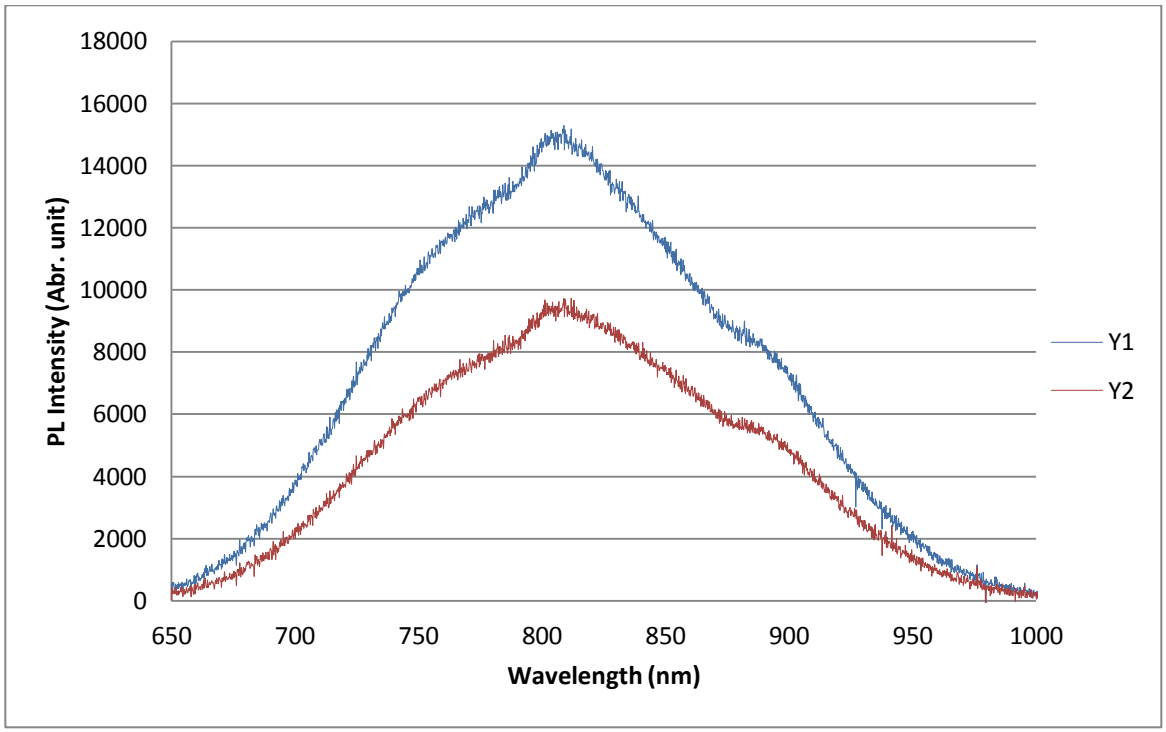

Figure 57: Wavelength vs PL intensity graph for 10 KeV implanted energy samples. Y1 and Y2 indicate samples PL intensities at measuring temperature of 20^{o} C and 60^{o} C respectively. The oxide layer of samples was 1150 A. Integration time during measuring PL was 6 seconds.

Imp E (KeV)	Thickness (A)	Annealing Temp (^{o} C)	Measuring Temp (^{o} C)	PL (Arb. Unit)	PL Range (nm)
10	1150	1100	20	15000	650-950
10	1150	1100	30	14000	650-950
10	1150	1100	40	12200	650-950
10	1150	1100	50	11500	650-950
10	1150	1100	60	9500	650-950

Table 13: PL intensities peak along with the PL ranges were shown for different measuring temperature. The implantation energy, dose and oxide layer thickness were 10 KeV, 1.5×10^{16} ions_cm^{-2} and 1150 A respectively.

The values of PL 1150 A thickness samples caused by different measurement temperatures are shown in table 13. The PL intensities were 15000 Arb. unit, 12200 Arb. unit and 9500 Arb. unit for the measuring temperature of 20^o C, 40^o C and 60^o C (Figure 57).

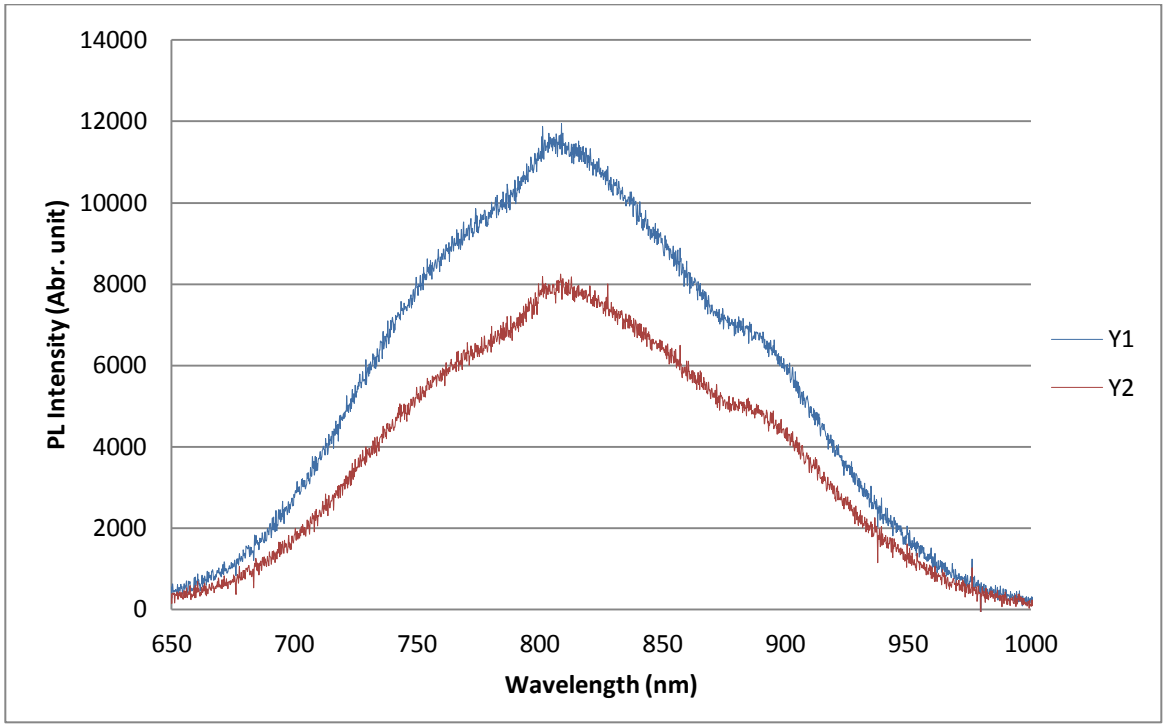

Figure 58: Wavelength vs PL intensity graph for 10 KeV implanted energy samples. Y1 and Y2 indicate samples PL intensities at measuring temperature of 20^{o} C and 60^{o} C respectively. The oxide layer of samples was 1800 A. Integration time during measuring PL was 6 seconds.

The PL caused by different measurement temperatures for 1800 A thickness samples are revealed in table 14. The PL intensities were 11700 Arb. unit, 10000 Arb. unit and 8000 Arb. unit for the measuring temperature of 20^{o} C, 40^{o} C and 60^{o} C (Figure 58).

Imp E (KeV)	Thickness (A)	Annealing Temp (^{o} C)	Measuring Temp (^{o} C)	PL (Arb. Unit)	PL Range (nm)
10	1800	1100	20	11700	650-950
10	1800	1100	30	11000	650-950
10	1800	1100	40	10000	650-950
10	1800	1100	50	8700	650-950
10	1800	1100	60	8000	650-950

Table 14: PL intensities peak along with the PL ranges were shown for different measuring temperature. The implantation energy, dose and oxide layer thickness were 10 KeV, 1.5×10^{16} ions_cm^{-2} and 1800 A respectively.

So it is found that the PL intensity for 10 KeV implanted samples is inversely proportional with measuring temperature. The PL intensities were increased with the increase of oxide thickness till 1150 A. The cause behind that was described at the effect of oxide thickness section.

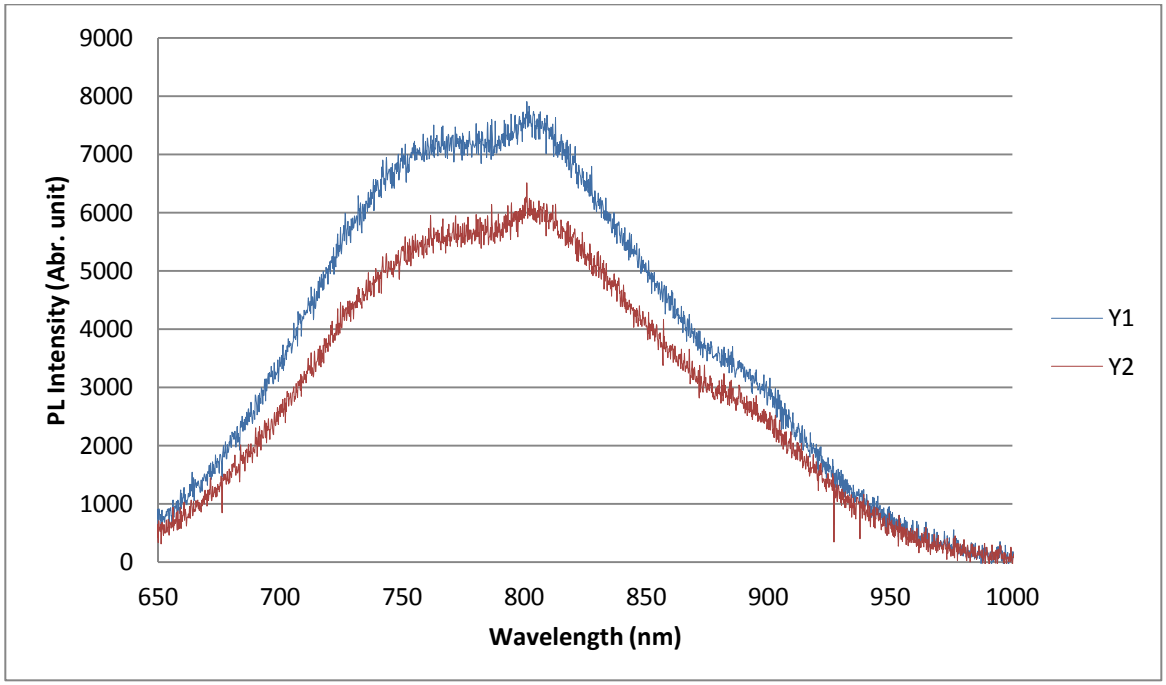

Figure 59: Wavelength vs PL intensity graph for 20 KeV implanted energy samples. Y1 and Y2 indicate samples PL intensities at measuring temperature of 20^{o} C and 60^{o} C respectively. The oxide layer of samples was 600 A. Integration time during measuring PL was 6 seconds.

Imp E (KeV)	Thickness (A)	Annealing Temp (^{o} C)	Measuring Temp (^{o} C)	PL (Arb. Unit)	PL Range (nm)
20	600	1100	20	7800	650-950
20	600	1100	30	7300	650-950
20	600	1100	40	7000	650-950
20	600	1100	50	6500	650-950
20	600	1100	60	6000	650-950

Table 15: PL intensities peak along with the PL ranges were shown for different measuring temperature. The implantation energy, dose and oxide layer thickness were 20 KeV, 2.3×10^{16} ions_cm^{-2} and 600 A respectively.

The values of PL for 20 KeV implantation energy, 2.3×10^{16} ions_cm^{-2} dose and 600 A thickness samples due to different measuring temperatures are shown at table 15. The PL intensities were 7800 Arb. unit, 7000 Arb. unit and 6000 Arb. unit for the measuring temperature of 20^{o} C, 40^{o} C and 60^{o} C (Figure 59).

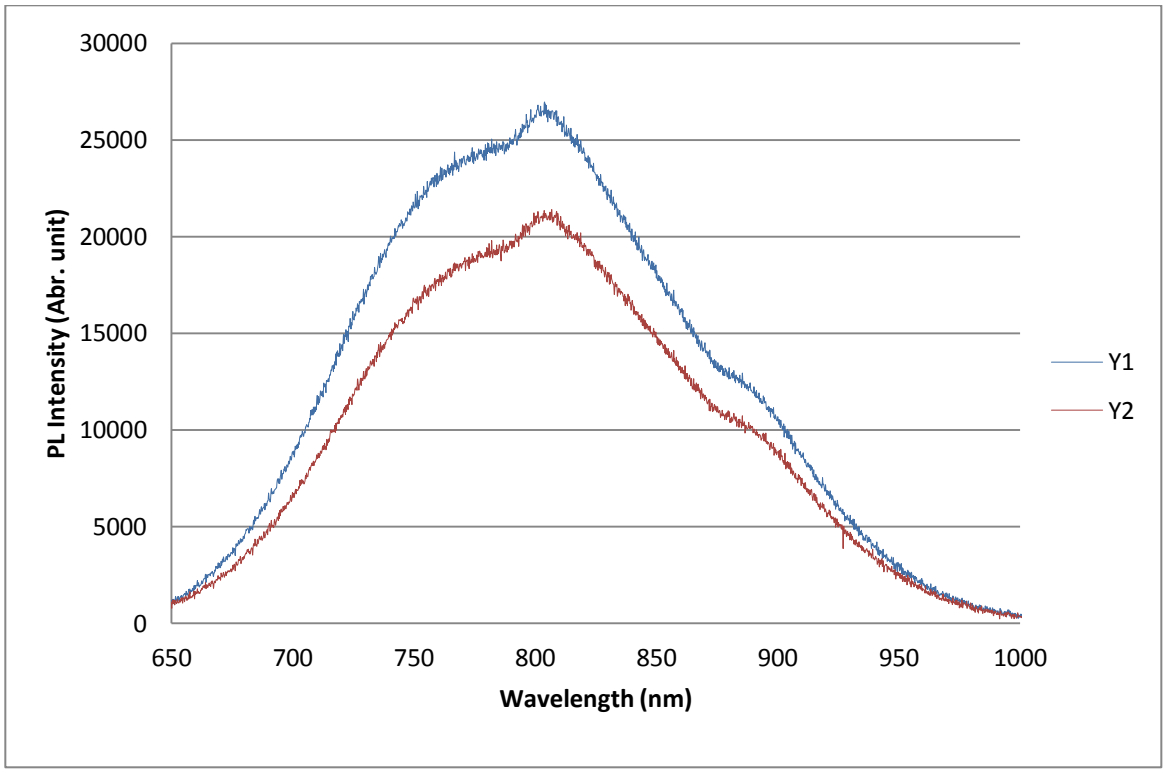

Figure 60: Wavelength vs PL intensity graph for 10 KeV implanted energy samples. Y1 and Y2 indicate samples PL intensities at measuring temperature of 20^{o} C and 60^{o} C respectively. The oxide layer of samples was 1150 A. Integration time during measuring PL was 6 seconds.

Imp E (KeV)	Thickness (A)	Annealing Temp (^{o} C)	Measuring Temp (^{o} C)	PL (Arb. Unit)	PL Range (nm)
20	1150	1100	20	26500	650-950
20	1150	1100	30	25000	650-950
20	1150	1100	40	24500	650-950
20	1150	1100	50	23000	650-950
20	1150	1100	60	21500	650-950

Table 16: PL intensities peak along with the PL ranges were shown for different measuring temperature. The implantation energy, dose and oxide layer thickness were 20 KeV, 2.3×10^{16} ions_cm^{-2} and 1150 A respectively.

The PL caused by different measuring temperatures for 1150 A thickness samples are shown in table 16. The PL intensities were 26500 Arb. unit, 24500 Arb. unit and 21500 Arb. unit for the measuring temperature of 20^o C, 40^o C and 60^o C (Figure 60).

The results of PL intensities for different measuring temperature due to 20 KeV implantation energies were same as that of 10 KeV i.e. inversely proportional. This happens due to the Auger effect. Auger effect is the recombination of inner cell hole by an electron of outer cell without any light. This electron is known as auger electron. When recombination due to auger effect increases, then recombination with light emission probability decreases [72] [73].

Huldt *et. al.* found the relationship of auger effect with the temperature is proportional to $T^{0.6}$. So the Auger effect increases with the increase of temperature [72].

Increasing temperature accelerates Auger effect and due to this behavior, PL intensities decreases. Jang *et. al.* also found the same trend of result [73].

4.9 The Effect of Types of Oxide Layer

Toward the end of the research, I decided to perform a brief investigation of the effects of the oxide type on the PL luminescence. Dry oxidation and wet oxidation are the most common methods to fabricate the oxide layer on Si wafer surface [45] [68-71]. The rate of oxidation for dry oxidation is slower than that of wet oxidation [45] [58] [68]. Linear pressure dependence oxidation rate is an important characteristic for wet oxidation whereas the dependence is sub linear for dry oxidation [62]. Wet oxidation also has the feature of insignificant early period oxidation enrichment [45] [62]. Only oxygen (O_2) is used for the dry oxidation but water i.e. H_2O is used for wet oxidation [67].

Reaction during dry oxidation,

$$Si + O_2 \rightarrow SiO_2 \text{---------- (xi)}$$

Reaction during wet oxidation,

$$Si + H_2O \rightarrow SiO_2 + 2H \text{---------- (xii)}$$

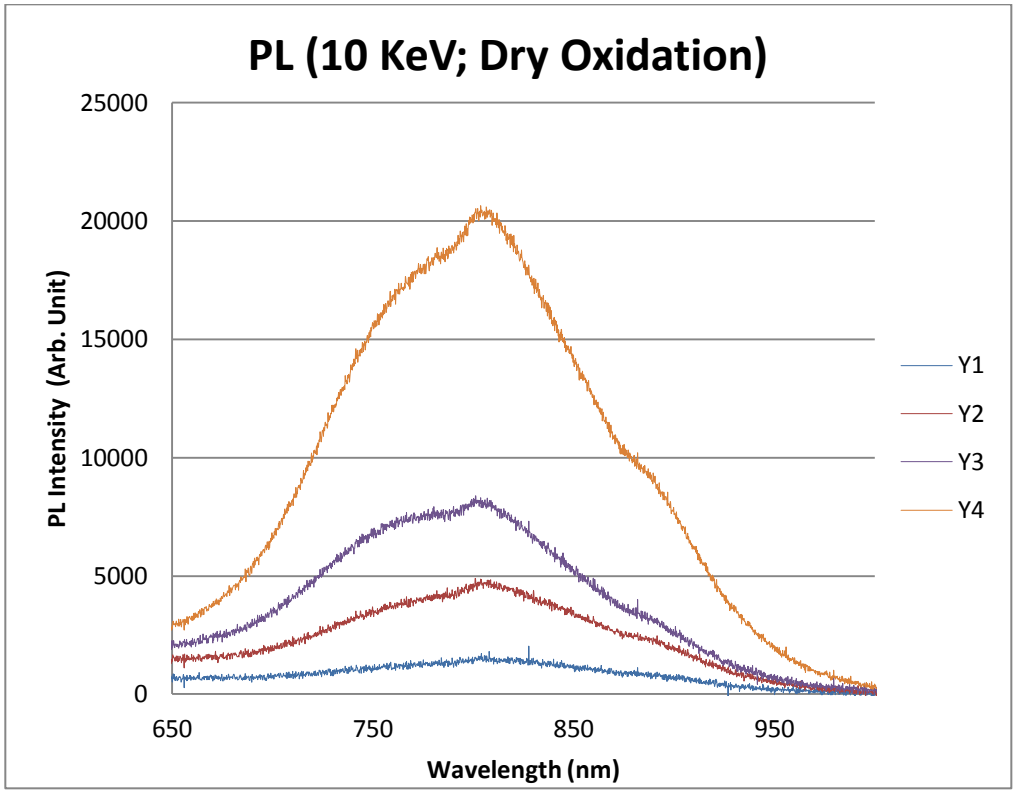

Figure 61: Wavelength vs PL intensity graph for 10KeV implantation energies dry oxidation. RTA was done at 1100^{o} C for 30 minutes. The parameters for Y1 are 400 A thick oxide layer with dry oxidation. The parameters for Y2;Y3 and Y4 are 600 A, dry oxidation; 1000 A, dry oxidation and 1300 A, dry oxidation respectively. Integration time was 6 seconds.

Oxide Thickness (A)	Peak PL Intensity (Arb. Unit)
400	2000
600	4600
1000	7800
1300	20200

Table 17: The peak PL intensities for dry oxidation samples are shown. Implantation energy and implantation dose were 10 KeV and 2 ×10 ^{16} ions_cm^{-2} respectively.

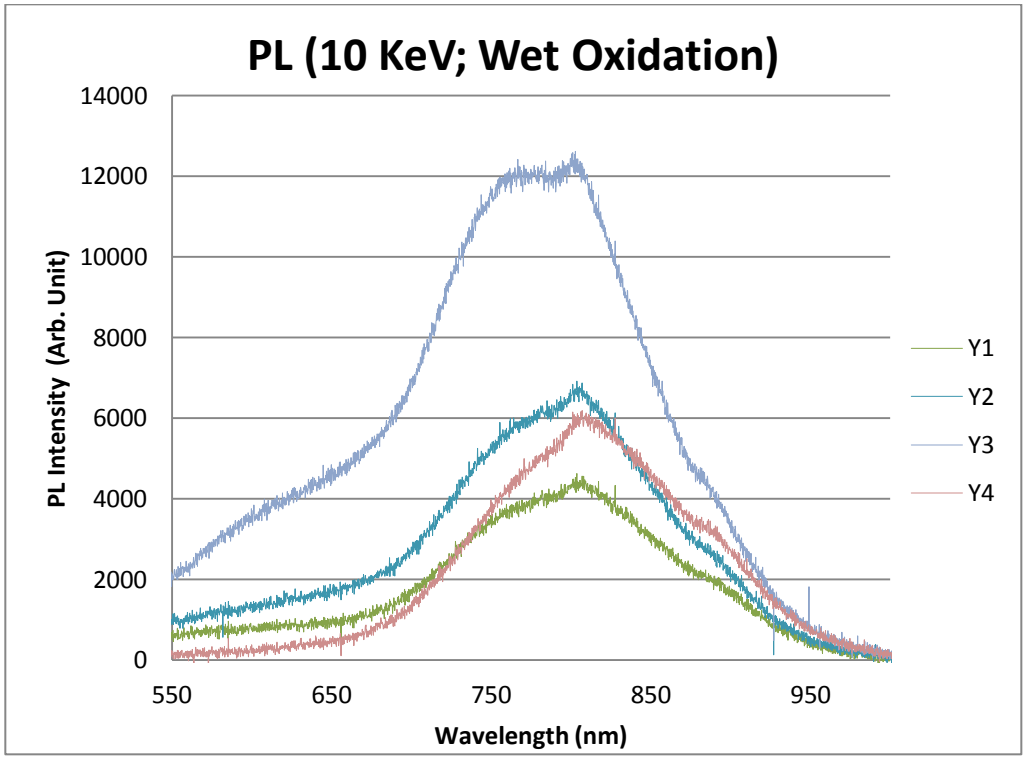

Figure 62: Wavelength vs PL intensity graph for 10KeV implantation energies for wet oxidation. RTA was done at 1100^{o} C for 30 minutes. The parameters for Y1 are 600 A thick oxide layer with wet oxidation. The parameters for Y2;Y3 and Y4 1000 A, wet oxidation; 1300A, wet oxidation and 1900 A, wet oxidation respectively. Integration time was 6 seconds.

Oxide Thickness (A)	Peak PL Intensity (Arb. Unit)
600	4200
1000	6500
1300	12200
1900	6000

Table 18: The peak PL intensities for wet oxidation samples are shown. Implantation energy and implantation dose were 10 KeV and 2 ×10 ^{16} ions_cm^{-2} respectively.

The PL intensities for dry and wet oxidation samples are plotted at figure 61 and figure 62 respectively. Both cases the implantation dose and energy were 2×10^{16} ions_cm^{-2}and 10 KeV. The PL intensities peak corresponding to oxide thickness are shown at table 17 (dry oxidation) and table 18 (wet oxidation).

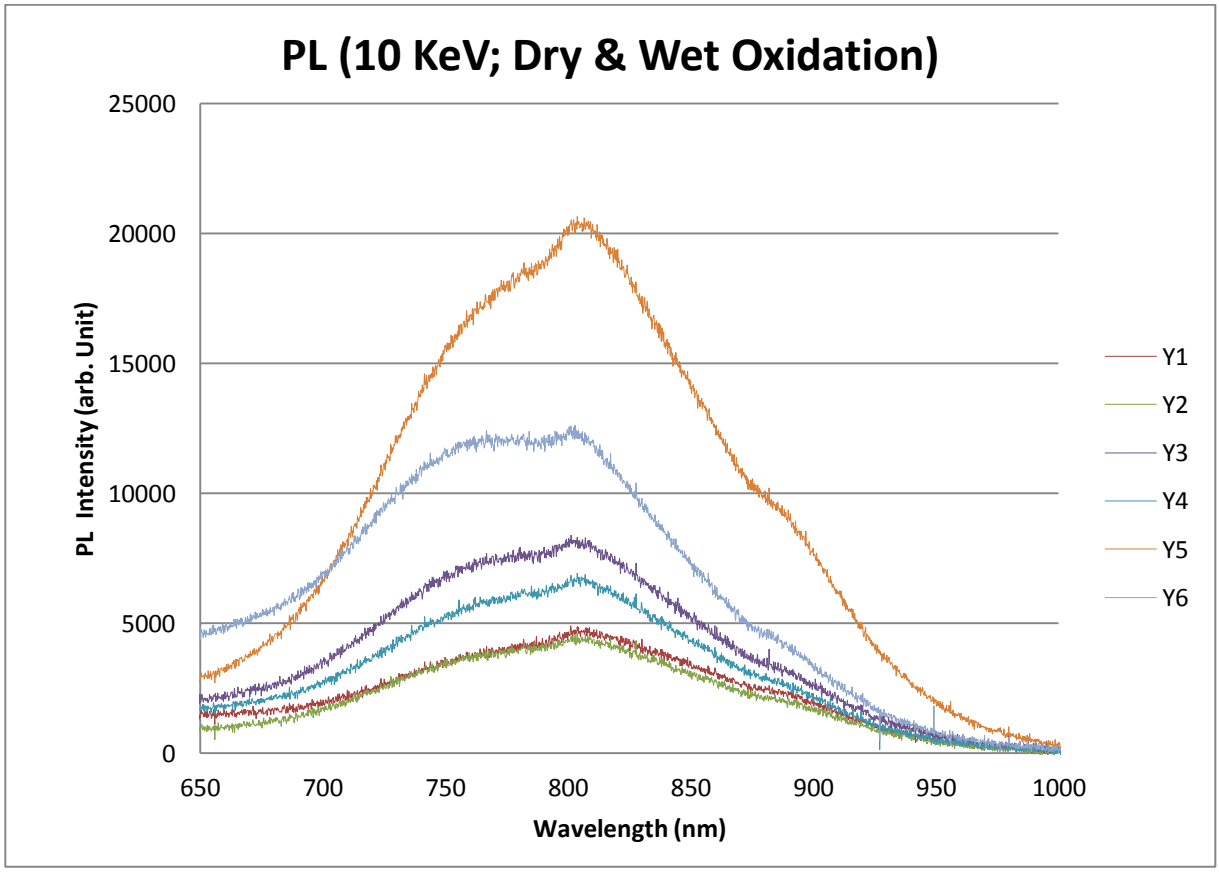

Figure 63: Wavelength vs PL intensity graph for 10KeV implantation energies for both dry oxidation and wet oxidation. RTA was done at 1100^{o} C for 30 minutes. The parameters for Y1 are 600 A thick oxide layer with dry oxidation. The parameters for Y2;Y3;Y4;Y5 and Y6 are 600 A, wet oxidation; 1000 A, dry oxidation; 1000 A, wet oxidation; 1300 A, dry oxidation and 1300A, wet oxidation respectively. Integration time was 6 seconds.

Oxide Thickness (A)	**Peak PL Intensity (Arb. Unit) Dry Oxidation**	**Peak PL Intensity (Arb. Unit) Wet Oxidation**
600	4600	4200
1000	7800	6500
1300	20200	12200

Table 19: The peak PL intensities for dry oxidation and wet oxidation samples are shown. Implantation energy and implantation dose were 10 KeV and 2×10^{16} ions_cm^{-2} respectively.

The PL intensities for three oxide thickness are plotted for both type of oxide samples at figure 63 and the corresponding results are shown at table 19. RTA was used to make the dry oxide samples. It is hard to make thicker dry oxide samples from RTA due to the high duration of process time at high temperatures. The PL intensities for 1000 A dry oxide thickness sample was about 1.2 times than that of wet oxide sample and for 1300 A the ration was about 1.7 times. So it can be said that dry oxidation samples provide more light compared with that of the wet oxidation samples.

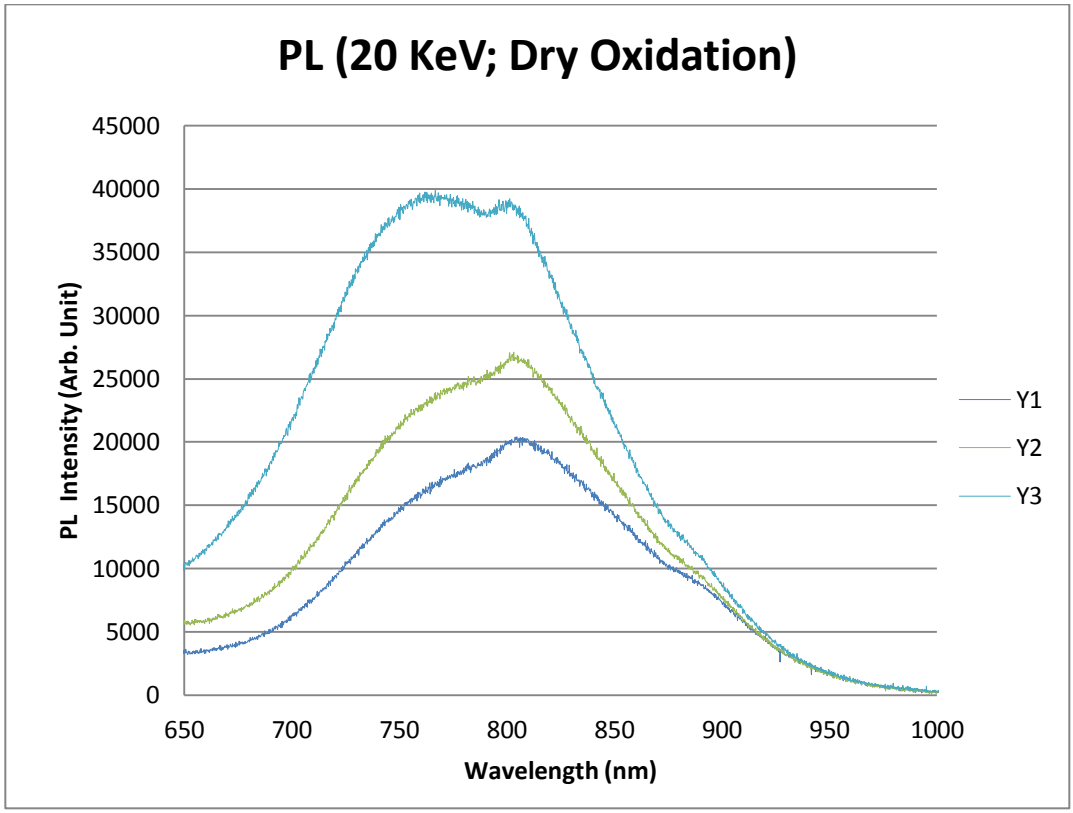

Figure 64: Wavelength vs PL intensity graph for 20KeV implantation energies for dry oxidation. RTA was done at 1100^{o} C for 30 minutes. The parameters for Y1 are 600 A thick oxide layer with dry oxidation. The parameters for Y2 and Y3 are 1000 A, dry oxidation and 1300 A, dry oxidation respectively. Integration time was 6 seconds.

Oxide Thickness (A)	Peak PL Intensity (Arb. Unit)
600	20000
1000	27000
1300	39000

Table 20: The peak PL intensities for dry oxidation samples are shown. Implantation energy and implantation dose were 20 KeV and 2 ×10 ^{16} ions_cm^{-2} respectively.

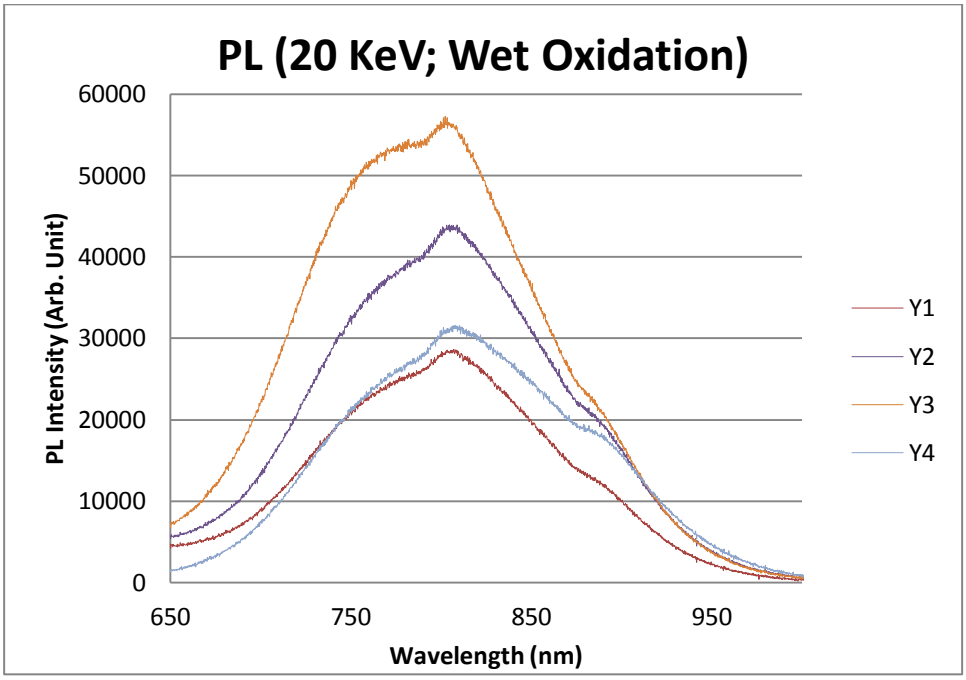

Figure 65: Wavelength vs PL intensity graph for 20KeV implantation energies for wet oxidation. RTA was done at 1100^{o} C for 30 minutes. The parameters for Y1 are 600 A thick oxide layer with wet oxidation. The parameters for Y2;Y3 and Y4 are 1000 A, wet oxidation; 1300A, wet oxidation and 1900 A, wet oxidation respectively. Integration time was 6 seconds.

Oxide Thickness (A)	Peak PL Intensity (Arb. Unit)
600	28000
1000	44000
1300	57000
1900	32000

Table 21: The peak PL intensities for wet oxidation samples are shown. Implantation energy and implantation dose were 20 KeV and 2 ×10 ^{16} ions_cm^{-2} respectively.

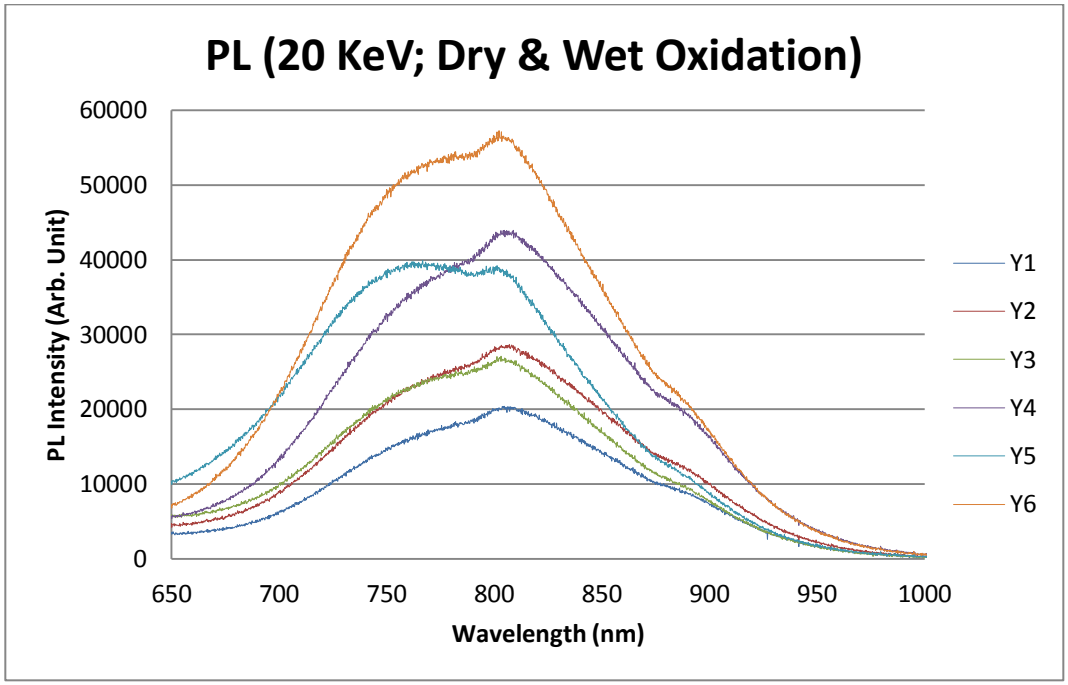

Figure 66: Wavelength vs PL intensity graph for 20KeV implantation energies for both dry oxidation and wet oxidation. RTA was done at 1100^{o} C for 30 minutes. The parameters for Y1 are 600 A thick oxide layer with dry oxidation. The parameters for Y2;Y3;Y4;Y5 and Y6 are 600 A, wet oxidation; 1000 A, dry oxidation; 1000 A, wet oxidation; 1300 A, dry oxidation and 1300A, wet oxidation respectively. Integration time was 6 seconds.

Oxide Thickness (A)	Peak PL Intensity (Arb. Unit) Dry Oxidation	Peak PL Intensity (Arb. Unit) Wet Oxidation
600	20000	28000
1000	27000	44000
1300	39000	57000

Table 22: The peak PL intensities for dry oxidation and wet oxidation samples are shown. Implantation energy and implantation dose were 20 KeV and 2×10 ^{16} ions_cm^{-2} respectively.

The PL intensities for three oxide thickness are plotted for both type of oxide samples at figure 66 and the corresponding results are shown at table 22. The PL intensities for 1000 A and 1300 A wet oxide thickness samples were about 1.5 times than that of dry oxide samples. So it can be said that wet oxidation samples provide more light compared with that of the dry oxidation samples. So it is assumed that there might be an implantation energy between 10 KeV and 20 KeV where the effect changes. Due to the limited time only two implantation energies were studied. So this is a very good option for future study. The PL intensities difference between the two types of sample is mainly due to the existence of water vapor at wet oxide samples [59]. One interesting feature was found for the wet oxidation samples i.e. there were two PL peaks; one is ~ 750 nm and other one is ~ 850 nm. Tetelbaum *et. al.* discussed the features and they found peaks at 770 nm and 880 nm. The interband recombination i.e. transition inside nanocrystal [59-61] or the recombination of excitations of nanocrystals with the border region states [59] [62-64] is responsible for PL peak at ~ 770 nm and peak at 880 nm is due to water vapour presents at interface states [59]. This group also showed a Si nanocrystals model for oxidation samples.

4.10 Conclusion

The photoluminescence from Si-nanocrystals embedded in SiO_2 is a function of numerous things. After Si ion implantation into SiO_2 high temperature annealing is performed for removing the defects and forming the nanocrystals. The first contribution

of this thesis is that1100^{o} C rapid thermal annealing is the best choice for fabricating Si nanocrystals with RTA following ion implantation. Second, the PL appears to be a function of SiO_2 thickness, an observation not previously made. Third, there is an inverse relationship between PL intensity and measuring temperature. This result provides a potential application in the area of temperature sensing. The fourth and final contribution is that types of thermal oxidation (wet or dry) have an impact on PL intensities.

CHAPTER FIVE: CONCLUSION AND SUGGESTION FOR FUTURE WORK

5.1 Conclusion

A relatively large amount of light comes from the Si nanocrystals embedded in SiO_2 matrix. A process of fabricating Si nanocrystals by ion implantation followed by only high temperature rapid thermal annealing is described. Normally a long time duration furnace annealing followed by a short time duration rapid thermal annealing is performed after ion implantation. In the current work, only RTA annealing was used. This thesis contributes knowledge on the effect of annealing temperature, measuring temperature, oxide layer thickness and grown types of oxide layer. The potential application of Si nanocrystals is a vast area which almost includes nearly all branches of electronic engineering. A literature review was done for gathering in depth knowledge about the topic.

In chapter 1, the basic principal and concepts of light emission and commonly used terms have been discussed. In chapter 2, the theoretical consideration and background literature review have been done. The light emission mechanism, the process of fabricating Si nanocrystals, effect of implantation doses as well as effect of annealing temperature and implantation temperature are discussed.

In chapter 3, the experimental set-ups and basic operating principals have been discussed. In this work an ion implanter was used in conjunction with a rapid thermal

annealer to form Si-nanocrystals. The PL set up is used to measure the light coming from the samples i.e. from Si nanocrystals.

In chapter 4, the results have been discussed. The PL intensities increase with the doses till a value after that the PL decreases due to the mechanical overlapping of Si nanocrystals. Same result was found for the high temperature annealing and Oswald ripening is the cause for the outcomes. 1100^{o} C annealing temperature provided the best PL. The oxide thickness had the similar PL effect tends as that of annealing temperature i.e. first increase to maximum value and then decreasing. Oxide layer thickness of 1150 A is found best for the samples used during the thesis work. The result was described on the basis of crystal size.

The results of the effects of measuring temperature and oxide thickness layer grown type are discussed. Very little work was done previously in this field. The PL intensities decrease with the increase of measuring temperature. An interesting result was found during the work on grown types of oxide layer i.e. dry oxidation provided more PL compared with wet oxidation for 10 KeV implantation energy whereas the results was reverse for 20 KeV implantation energy.

5.2 Future Work

Lots of scopes for future work are provided. The effect of measuring temperature is a very promising field to do further work because very few works have been done on this while it provides potential in temperature sensing. In this thesis work, implantation

energies other than 10KeV and 20KeV were not investigated, while only two implantation doses are used. Expanding the range of energies and doses will be of interest, as would be a more detailed investigation of the annealing temperatures. The most interesting results are perhaps the strong dependence of luminescence on thin film thickness and oxide type. More work is needed to fully explain why these parameters play a role in PL intensity.

REFERENCES

[1] T. S. Iwayama, T. Hama, D. E. Hole, I. W. Boyd, Science direct, vacuum 81 (2006) 179-185.

[2] Jordan Anstey, Thesis work, McMaster University

[3] B. Garrido, M. Lopez, A. Perez-Rodrıguez, C. Garcıa, P. Pellegrino, R. Ferre, J.A. Moreno, J.R. Morante, C. Bonafos, M. Carrada, A. Claverie, J. de la Torre, A. Souifi, Nuclear Instruments and Methods in Physics Research, B 216 (2004), 213–221.

[4] "Solid State Electronic Devices" by Ben G. Streetman, 4th edition, pp. 56-59.

[5] Han-Woo Choi, Hyung-Joo Woo, Joon-Kon Kim, Gi-Dong Kim, Wan Hong, and Young-Yong Ji, Bull. Korean Chem. Soc. 2004, Vol. 25, No. 4

[6] Song, H. Z., Bao, X. M., Li, N. S., Zhang, J. Y. J. Appl. Phys. 1997, 82, 4028.

[7] Brongersma, M. L.; Polman, A., Min, K. S., Boer, E.; Tambo, T. Atwater, H. A. Appl. Phys. Lett. 1998, 72, 2577.

[8] Tsutomu Shimizu-Iwayama, David E Hole‡ and Ian W Boyd, J. Phys.: Condens. Matter 11 (1999) 6595–6604, PII: S0953-8984(99)03121-5

[9] K. Koshida, Application of Si nanocrystals, Graduate School of Engineering, Tokyo Univ. Agri. & Tech., Tokyo, Japan.

[10] C. R. Mokry, P. J. Simpson and A. P. Knights, journal of applied physics (2009)105, 114301

[11] T. S. Iwayama, S. Fukaya, H. Watanable, T. Hama, D. E. Hole, Nuclear Instuements and Methods in Physics Research B 267 (2009) 1328-1331.

[12] A. Polman, "Erbium Implanted Thin Film Photonic Materials", (4 March, 1997).

[13] Robert G. Elliman, Andrew R. Wilkinson, Nathanael Smith, Marc G. Spooner, Tessica D.M. Weijers, Max J. Lederer, Barry Luther-Davies and Marek Samoc, Journal of the Korean Physical Society, Vol. 45, December 2004, pp. S656~S660

[14] E. Edelberg, S. Bergh, R. Naone, M. Hall, and E. S. Aydil, Journal of Applied Physics 81, 2410 (1997).

[15] T. S. Iwayama, T. Hama, D. E. Hole, I. W. Boyd, Science direct, Microelectronics reliability 47 (2007) 781-785

[16] T. S. Iwayama, T. Hama, D. E. Hole, I. W. Boyd, Surface & Coatings Technology 201 (2007) 8490-8494.

[17] G. H. Li, K. Ding, Y. Chen, H. X. Han and Z. P. Wang, Journal of Applied Physics, volume 88, number 3, 1 August 2000

[18] Iwayama TS, Fujita K, Nakao S, Saitoh K, Fujita T, Itoh N. Journal of Applied Physics 1994;75:7779,.

[19] Iwayama TS, Nakao S, Saitoh K., Applied Physics Lett 1994;65:1814.

[20] Min KS, Shcheglov KV, Yang CM, Atwater HA, Brongersma ML, Polman A. Appl Phys Lett 1996;69:2033.

[21] Mutti P, Ghislotti G, Bertoni S, Bonoldi L, Cerofolini GF, Meda L, et al. Applied Physics Lett 1995;66:851.

[22] Zhu JG, White CW, Budai JD, Withrow SP, Chen Y. J Appl Phys 1995;77:4386.

[23] Cheylan, S.; Elliman, R. G. Nucl. Instr. and Meth. in Phys. Res. B 2001, 175-177, 422.

[24] T. Komoda, J.P. Kelly, R.M. Gwilliam, P.L.F. Hemment, B.J. Sealy, Nucl. Instr. and Meth. B 112 (1996) 219

[25] S.P. Withrow, C.W. White, A. Meldrum, J.D. Budai, J. Appl. Phys. 86 (1999) 396

[26] U. S. Sais, E. C. Moreira, E. Ribeiro, H. Boudinov, L. Amaral, and M. Behar, J Appl. Phys., volume 95, number 9, 1 May 2004

[27] M. Y. Valakh, V. A. Yukhimchuk, V. Y. Bratus, A. A. Konchits, P. L. F. Hemment, and T. Komoda, Journal of Applied Physics. 1999, 85, 168

[28] Basic Semiconductor Physics, http://britneyspears.ac/physics/basics/basics.htm

[29] "Principal of Electronic Materials and Devices" by S O Kasap, pp.388-389.

[30] "Principal of Electronic Materials and Devices" by S O Kasap, pp. 390-391.

[31] Doering, R. and Nishi, Y, Ed., Handbook of Semiconductor Manufacturing Technology, Second Edition, CRC Press, Taylor and Francis Group LLC, Boca Raton, 2008, 1720 pp.

[32] Ziegler, J. F., Ed. Ion Implantation: Science and Technology, Ion Implant Technology Co.: Edgewater, MD, 2000, 687 pp.

[33] Ryssel, H. and Ruge, I. Ion Implantation, John Wiley and Sons: New York, 1986, 350 pp.

[34] E. Chason, S. T. Picraux, J. M. Poate, J. O. Borland, M. I. Current, T. Diaz de la Rubia, D. J. Eaglesham, O. W. Holland, M. E. Law, C. W. Magee, J. W. Mayer, J. Melngailis and A. F. Tasch , Ion beams in silicon processing and characterization, J. Appl. Phys., Vol. 81, No. 10, 15 May 1997

[35] The Industrial Physicist,

http://aip.org/tip/INPHFA/vol-9/iss-3/p12.html

[36] S. Guha, Journal of Apped. Physics ,1998, 84, 5210.

[37] Bo Cui, Microfabrication and thin film technology, ECE, University of Waterloo

[38] Dr. Alan Doolittl,Georgia Tech ECE 6450

[39] Shabbir A Bashar Ph.D. thesis "Study of Indium Tin Oxide (ITO) for Novel Optoelectronic Devices"

[40] JetFirst company website,

http:// jipelec.com/products/jetfirst/index.htm

[41] Dr. Kolin Brown, standard operating procedure: as---micro rapid thermal annealer

[42] Institute of Terahertz Science and Technology,

http://itst.ucsb.edu

[43] Horiba group,

http://horiba.com/

[44] Brigham Young University, Department of Electrical & Computer Engineering

http://cleanroom.byu.edu/OxideThickCalc.phtml

[45] B. E. Deal, A. S. Grove, Journal of Applied Physics, 1965, 36,12

[46] Deal-Grove_model,

http://en.wikipedia.org/wiki/Deal%E2%80%93Grove_model

[47] Deal-Grove_model,

http://iue.tuwien.ac.at/phd/hollauer/node16.html

[48] Lenzo Pavesi and Rasit Turran, Silicon Nanocrystals: Fundamentals, Synthesis and Application

[49] SRIM & TRIM softwares by James Ziegler

[50] Gfroerer T., In Encyclopaedia of Analytical Chemistry; Meyers, R. A., Ed., John Wiley and Sons Ltd.: Chichester,pp 9209-9231, (2000).

[51] Post graduation courses, Department of physics, University of Warwick

[52] A. J. Armini, S. N. Bunker and M. B. Spitzer, "Non-mass-analyzed Ion Implantation Equipment for high Volume Solar Cell Production," Proc. 16th IEEE Photovoltaic Specialists Conference, 27-30 Sep 1982, San Diego California, pp. 895-899.

[53] G. Landis et al., "Apparatus and Technique for Pulsed Electron Beam Annealing for Solar Cell Production," Proc. 15th IEEE Photovoltaic Specialists Conf., Orlando FL; 976-980 (1981).

[54] T. S Iwayama, M. Ohshima, I. Nilmi, S. Nakao, K. Saitoh, T. Fujita, N. Itoh, J. Phys. Cond. Mater. 5 (1993) L375

[55] G. A. Kachurin, K. S. Zhuravlev, N. A. Pazdnikov, A. F. Leie, I. E. Tyschenko, V.A. Volodin, W. Skorupa, R. A. Yankov, Nucl. Instr. And Meth. B 127 (1997) 583

[56] C. Bonafos, B. Colombeau, A. Altibelli, M. Carrada, G. Ben Assayag, B. Garrido, M. Lopez, A. Perez-Rodriguez, J. R. Morante, A. Claverie, Nucl. Instr. And Meth. B 178 (2001) 17-24

[57] J. D. Plummer, M. D. Deal, and P. B. Griffin, Silicon VLSI Technology: Fundamentals, Practice and Modeling, New Jersey: Prentice Hall, 2000.

[58] S. Shih, C. Tsai, K.H. Li, K. H. Jung, J. C. Campbell et al; Appl. Phys. Lett. 60, 633 (1992)

[59] D. I. Tetelbaum, O. N. Gorshkov, A. P. Kasatkin, A. N. Mikhaylov, A. I. Belov, D. M. Gaponova, and S. V. Morozov; Physics of the Solid State; Vol. 47, No. 1, 2005, pp. 13–17

[60] B. Garrido Fernandez, M. Lo´pez, C. Garcı´a, A. Pe´rez-Rodrı´guez, and J. R. Morante, C. Bonafos, M. Carrada, and A. Claverie; J. Appl. Phys., Vol. 91, No. 2, 15 January 2002

[61] K. S. Min, K. V. Scheglov, C. M. Yang, H. A. Atwater, M. L. Brongersma, and A. Polman, Appl. Phys. Lett. 69, 2033 (1996)

[62] L. N. Lie, R. R. Razouk, and B. E. Deal; J. Electrochem. Soc. 129, 2828 (1982)

[63] T. Shimizu-Iwayama, K. Fujita, S. Nakao, K. Saitoh, R. Fujita, and N. Itoh; J. Appl. Phys. 75, 7779 (1994)

[64] Y. Kanemitsu and S. Okamoto; Phys. Rev. B 58, 9652 (1998)

[65] D. I. Tetelbaum, O. N. Gorshkov, S. A. Trushin, D. G. Revin, D. M. Gaponova, and W. Eckstein, 8th Int. Symp. `` Nanostructures: Physics and Technology`` 2000.

[66] W. Ostwald; Z. Phys. Chem. 34, 495 (1900)

[67] J. P. Zhang, P. L. F. Hemment, S. M. Newstead, A. R. Powell, T. E. Whall and E. H. C. Parker; Thin Solid Films, 222 (1992) 141-144

[68] Masashi Uematsu, Hiroyuki Kageshima, and Kenji Shiraishi; J. Appl. Phys. 89, 1948 (2001)

[69] J. R. Ligenza; J. Phys. Chem. 65, 2011 (1961)

[70] H. C. Evitts, H. W. Cooper, and S. S. Flaschen; J. Electrochem. Soc. 111, 688 (1964)

[71] B. E. Deal; J. Electrochem. Soc. 125, 576 (1978)

[72] L. Huldt, N. G. Nilsson, and K. G. Svantesson; Appl. Phys. Lett. 35, 776 (1979)

[73] D.-J. Jang, Michael E. Flatte, C. H. Grein, J. T. Olesberg, T. C. Hasenberg, and Thomas F. Boggess; Physical Review B; Volume 58, Number 19; 15 November 1998-I

[74] D. Barba, F. Martin, C. Dahmoune, and G. G. Ross; Appl. Phys. Lett. 89, 034107 (2006)

[75] Optical Interference

http://en.wikipedia.org/wiki/Interference_(wave_propagation)